QATAR UNIVERSITY

COLLEGE OF ENGINEERING

IGNITION DELAY TIME INVESTIGATION OF GTL FUEL BLENDS

BY

ABUBAKER MOHAMMED AHMED ELBASHIR

A Dissertation Submitted to

the College of Engineering

in Partial Fulfillment of the Requirements for the Degree of

Doctorate of Philosophy in Mechanical Engineering

June 2022

© 2022 Abubaker Elbashir. All Rights Reserved.

COMMITTEE PAGE

The members of the Committee approve the Dissertation of

Abubaker Elbashir defended on 10/05/2022.

Dr. Samer F. Ahmed

Thesis/Dissertation Supervisor

Dr. Saud Abdel Ghani

Committee Member

Dr. Fadwa Eljack

Committee Member

Dr. Mostafa H. ElSharqawy

Committee Member

Approved:

Khalid Kamal Naji, Dean, College of Engineering

ABSTRACT

ELBASIR, ABUBAKER MOHAMMED., Doctorate : June : [2022], Doctorate of Philosophy in Mechanical Engineering

Title: IGNITION DELAY TIME INVESTIGATION OF GTL FUEL BLENDS

Supervisor of Dissertation: Samer Fikri Ahmed.

Ignition delay is a vital combustion characteristic of any fuel that directly affects the development of internal combustion engines (ICEs) and exhaust emissions, especially in diesel engines. Considering the global interest in alternative fuels, GTL (Gas to Liquid) can be considered one of the promising new alternative fuels, especially for compression Ignition engines (CIE). In this dissertation, an investigation of this property experimentally for different types of heavy hydrocarbon fuels such as diesel, GTL, GTL/diesel blends, and GTL/biodiesel blends under a wide range of operation conditions like initial pressure, initial temperature and equivalence ratio; starting from a deep survey of the previous studies. The shock tube facility is used to investigate the fuel's combustion delay above. The works initially characterized the shock tube at Qatar University experimentally and numerically by determining the best location for the diaphragm (three different diaphragm positions (1m, 2m, and 3m)) alongside pressure ratio across the diaphragm (five pressure ratios (6-10)) since those parameters affect the tube performance and then the measurement of the ignition delay. The parametric study results showed that at high-pressure ratios, diaphragm positions 1 and 3 could generate a 7.4% rise in the Mach number of the incident shock wave compared to the diaphragm position-2 model.

Moreover, the diaphragm position-3 model tends to have a 2% increase in the temperature behind the reflected shock wave compared to the other two positions.

The ignition delay results are presented for three types of fuel: Diesel, GTL, and 50-50 Diesel-GTL blend for a variety range of pressure (6, 10, 14, and 20 bar), temperature (980 to 1120 K), and equivalence ratios (0.5, 0.7, 1.0, and 1.3). The ignition delay time measurements confirm a previous study by Joshua et al. that GTL has the shorter ignition delay period for all conditions. The Diesel-GTL blends data vary in different temperatures; however, it was noted between Diesel and GTL.

DEDICATION

This dissertation is dedicated to the soul of my mother, my father, brothers, sisters, friends, colleagues, teachers, Professors, and the rest of my family and relatives

Special dedications to my beloved small family, particularly my wife, for her continuous support and endless patience

ACKNOWLEDGMENTS

I would like to express my most profound appreciation to my supervisor Dr Samer F. Ahmed, who made this work possible and generously provided knowledge expertise and guaranteed the research finance. I could not have undertaken this journey without his guidance and advice carried me through all the stages of performing experiments, numerical analysis and guidance in writing this dissertation. I would also like to thank my committee members for letting my defense be an enjoyable moment and for their valuable comments and suggestions. Especially Dr Saud Ghani for the valuable advices while performing this study.

My acknowledgement extends to all my professors, TAs, Technicians, and colleagues in Mechanical Engineering Department at Qatar University for their cooperation and support.

Special thanks were sent to my colleagues, A. Saqr, Hamza Kamal, Yousif Badri, Ahmad Abdalla, Mohammed Bassiony, and exceedingly Eng. Yahya Elsaeed and Eng. Mohammed Ayad for their valuable technical advice.

"I would like to acknowledge the support of Qatar University for providing all the needs to achieve the requirements of this study."

TABLE OF CONTENTS

LIST OF TABLES

LIST OF FIGURES

Nomenclature

ST	Shock Tube
ICE	Internal Combustion Engine
ID	Ignition Delay
RCM	Rapid Compression Machine
CVB	Constant Volume Bomb
CFD	Computational Fluid Dynamics
2D	Two Dimensions
MFC	mass flow controllers
u	velocity in x_direction per unit mass
v	velocity in y_direction per unit mass
P	pressure
T	temperature
ρ	density
M	Mach number
Φ	Equivalence ratio
τ	Time
γ	Specific heat ratio
x	Argon volumetric ratio in Helium
Att	Attenuation rate of the incident shock wave
A/F	Air to fuel ratio
L	Driven section length

Subscripts

i	Incident shock wave
r	Reflected shock wave
1	Initial condition in the driven section before rapture
2	Incident Shock Wave condition at the driven section
3	The region behind expansion fan wave
4	Initial condition in the driver section before rapture
5	Reflected shock wave condition
S	Stoichiometric air-fuel mixture
a	Actual air-fuel mixture

CHAPTER 1: INTRODUCTION

This thesis chapter begins by providing context and rationale for the proposed thesis subject. Then, the present trends and necessity for this study are discussed, emphasizing Qatar's involvement in the GTL sector and research and the relevance of assessing the ignition delay attribute of a fuel. Finally, dissertation goals and objectives were established based on the provided reason.

1.1 Background

Parallel to boosting renewable energy sources such as wind and solar, the worldwide issue of developing clean, sustainable alternatives to fossil fuels or additives is urgent, given that combustion is of critical importance now, as it has been in the past and will be in the foreseeable future, and is globally the dominant means of energy release. While a drop-in replacement to conventional fuels is unlikely in the foreseeable future, complementary renewable alternatives are emerging, with biofuels gradually becoming an integral part of the energy mix. Although the pandemic of COVID19 influences in March & April 2020, petroleum consumption takes back the lead in the first half of the year 2021 out of all other fuel sources [1] According to Energy Information Agency (EIA), despite the boom in the use of alternative fuels and increasing electrification recently, for the primary energy consumption 2020 in the U.S., there is still a vast difference between petroleum and the natural gas consumptions and the other mentioned fuel sources as per figure (1). Based on the U.S Department of Energy reports, the petroleum and natural gas contribution in the U.S has reached 69% of the total energy consumption in 2020 which was 92.92 quadrillion Btu [2]. Petroleum consumption indicates that fossil fuels are still dominating the energy sector. However, high-

energy-density energy carriers such as liquid fuels are preferable in maritime transportation, long-distance trucking, and aircraft. The data in figure (1) show that the energy transition process is essential to investigate since it is directly reflected in the economy and environment. Thus, scientists' intention is still to find the proper methods of energy conversion, which imply an effective combustion process with less amount undesirable emitted gases. To do this, we must first get a fundamental understanding of the combustion reaction. Fluid flow and heat transfer are critical components in engine combustion modelling. However, because the combustion is eventually governed by chemistry, a chemical process must be good for a modelling or Simulation package to succeed. In other words, a chemical mechanism is like a path model that describes how to fuel, and oxidants are converted into final products by using specific chemical reactions. The breakdown of fuel molecules is the first step in these processes. For example, gasoline, Jet-A fuel, diesel fuel, and bio-diesel all have average carbon counts over 7; as a result, large hydrocarbon molecules account for a significant amount of the energy used (per molecule).

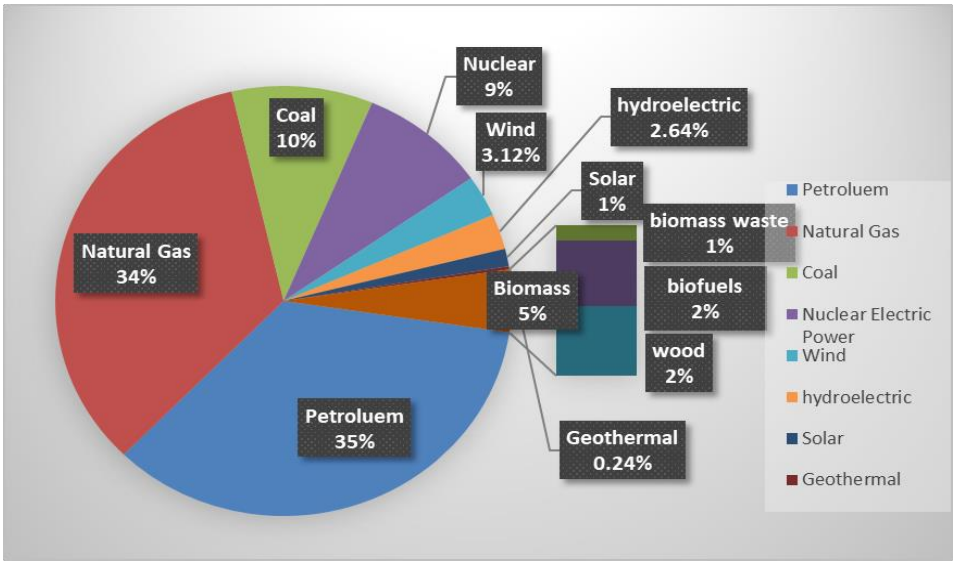

Figure 1. U.S. Government Total Energy Consumption by Source (Trillion Btu) [2]

1.2 Low Vapor Fuels

In current civilization, low-vapor-pressure fuels have been and continue to be extensively utilized. These fuels are appealing because of their low volatility under atmospheric conditions, which reduces the chance of unintentional explosion, making them challenging to deal with practically. Diesel fuel, which has low volatility (it has low volatility in standard atmospheric conditions than other hydrocarbon fuels such as gasoline, making it more stable regarding safety storage), is one of the most effective forms of low-vapor-pressure fuels. The widespread use of diesel fuel in different applications (trucks, trains, generators, boats, farms, and construction equipment).

1.3 Gap and Significance of the Research

According to the U.S Energy Information Administration (EIA) [[3]], the ever-increasing fuel prices due to the 37% growth in global energy consumption over the last 20 years, in addition to currently legislated reductions of specific exhaust gas emissions, have forced the engine manufactures to look for alternative fuels for ICEs. For example, the European Union ordered in 2005 that around 2 % of conventional fossil fuels be replaced with biofuels, a percentage increased to 5.75 % in 2010. [[4]] GTL fuels (approximately 70% super pure diesel fuel, naphtha around 25%, and some percentage consisting of LPG and others) have received increasing attention to be excellent alternative fuels for combustion engines. As the leading producer of GTL fuels, Qatar is interested in using these alternative fuels, especially diesel engines. Moreover, Qatar is currently moving to use GTL diesel fuel and its standard blends with regular diesel in all public transportations. The GTL diesel fuel production scale may not be enough to completely replace conventional diesel fuel. Therefore, blends of this fuel are essential to be

extensively studied in terms of their combustion characteristics before using these blends on a wide scale in diesel engines. From the previous studies, the auto-ignition characteristics of the GTL and its blends have not been investigated yet; however, only the GTL influence on the engine performance and emissions for an engine fueled by GTL diesel has been investigated in the literature [[5]–[12]]. Therefore, deep research needs to be done to fully evaluate and assess the ignition delay of the GTL fuel.

When it comes to the effective operation of a diesel engine, the ignition and burning of the fuel utilized are crucial factors. One of the most critical things that affect these processes is the ignition time it takes for the combustion to start up. The duration of this period can affect power output, combustion efficiency (and hence fuel efficiency and exhaust emissions), and engine maintenance. Furthermore, the ignition delay is influenced primarily by the fuel and engine design and operation characteristics. As a result, this parameter must be thoroughly investigated for new alternative blended fuels to improve engine design and operation and reduce emissions.

To date, researchers on GTL have mainly focused on engine experiments rather than fundamental studies. As we have seen above, engine studies, while extremely useful, involve too many variables and processes that render generalization difficult. There is a pressing need, therefore, for fundamental studies that enable the development of predictive tools to account for the complexities of the fuel as well as the multitude of processes that take place in spray combustion from primary atomization, to coalescence and dispersion, to evaporation, mixing and the formation of pollutants. Of course, it is impossible to complete such a massive endeavour without a thorough understanding of fuels' fundamental physical and

chemical characteristics. Chemical kinetic mechanisms and basic properties such as ignition delay times have already been generated for diesel and some alternative fuels. However, for GTL, there is still no sufficient complete understanding of it. Few kinds of research have been conducted to characterize such phenomena. The current research aims to fill this gap and enhance the current understanding of one of the fundamental properties of GTL and its blends with diesel, ignition delay time. In addition to that, the produced capacity of the GTL would not be sufficient to meet the fuel market demand, so a study of blending the Diesel with GTL could be a solution of having the merits of both fuels; thus, it is necessary to investigate the blend behaviour under the fuel test requirements.

1.4 Objectives and Organization of This Thesis

The study's objective was to initiate a feasible technique for testing heavy hydrocarbon fuels in a shock-tube facility. Under average temperature and pressure, these fuels are in the liquid phase focusing on the following points:

1. To design, build and characterize a shock-tube test rig that can be a method to study the autoignition of all fuel types.
2. Measuring the ignition delay time as a function of several variables such as initial pressure, initial temperature and equivalence ratio.
3. Measuring the ignition delay time of fuels: (a) pure diesel fuel (b) pure GTL fuel (c) blends of diesel/GTL

These fuels' ignition delay durations were measured under actual engine circumstances. The new data can be utilized to validate mixture fuel kinetics processes. Chapter 2 generally discussed the combustion characteristics of the heavy hydrocarbon fuels focusing on Diesel and GTL since they were the main aim of this study. Furthermore, reviews the property that needs to be investigated

(ignition delay time) and sees the various methods for measurements. Chapter 3 presents an overview of the facility, covering a shock tube theory as a tool for ignition delay time measurement and a shock tube survey. Chapter 4, the primary components, DAQ, devices needed to conduct experiments. Diagnostics setup, Ignition delay time measurement methodology, mixture preparation procedure, and the parametric study for the shock tube in Qatar University. Chapter 5 shows the study results starting with validation and comparison of the test facility results with the published studies in the literature.

Chapter 6 summarizes the thesis and includes recommendations for further research. The raw data samples for all delay period time tests undertaken in this work are included in the appendix sections, and calibration data are provided.

CHAPTER 2: FISCHER-TROPSCH DIESEL FUEL REVIEW

2.1 Introduction

Biodiesels are a renewable biofuel that shares many characteristics with fossil-based diesel, such as high cetane values. They can be used as pure, blended, or even directly in engines. Biodiesels are fatty acid esters generated from non-edible plants, food waste, animal fats, or algae. Their fatty acid chain length spans from C8 to around C22, from fully saturated to unsaturated, and their composition is dependent on the feedstock. Many countries have previously embraced different biodiesel production technologies as a long-term strategy for maximizing resource usage by turning waste into energy. Gas-to-liquid conversion produces synthetic crude, which may be processed and separated into a range of helpful hydrocarbon fractions by chemically converting natural gas, including liquid transportation fuels, into several usable hydrocarbon fractions (GTL). It is also possible to use this technology to turn coal and biomass, both abundant globally, into fuels and chemicals with additional value. It is possible that, this alternative would be advantageous for Qatar in conjunction with the country's large expenditures in GTL production from natural gas using Fischer-Tropsch processes [13].

Fischer-Tropsch synthesis (FTS) has piqued scientists' interest in recent decades since it is considered that producing liquid hydrocarbons using this promising clean technology might be a viable alternative option for addressing the lack of liquid transport fuels [14]–[16].

Hydrocarbons may be extracted from synthesis gas (C.O. and H2) using the Fisher-Tropsch technique. The Fisher-Tropsch method is used to make diesel fuels. Making diesel fuels using the Fisher-T process can be broken down into three stages:

Creating syngas, catalyzing Fisher-Tropsch reactions, and completing the product [Fischer–Tropsch reactions and the environment] are all steps in the manufacturing process. Syngas may be produced from any carbonaceous resource, such as natural gas, coal, or biomass, and is used to power vehicles. The production of synthetic gas is a capital-intensive process. Syngas production accounts for 70% of overall costs, according to estimates. The F-T product may be transformed into diesel of high grade during post-processing. Hydrocracking and hydrotreatment of Fischer-Tropsch fuels result in long-chain hydrocarbons, which enhance the cold flow qualities of the fuel. [17]. Post-processing removes any oxygenates that may have formed throughout this F-T conversion. This chapter generally discussed the combustion characteristics of heavy hydrocarbon fuels focusing on Diesel and GTL since they were the main aim. Furthermore, reviews the property that needs to be investigated (ignition delay time) and sees the various methods for measurements.

2.2 Fuel Properties

Sulfur content in Fischer-Tropsch diesel fuels is shallow. As a result, catalysts utilized in synthesis compounds are poisoned by sulfur compounds, essentially removed during syngas production. An example of a property is a Lubrication is provided by aromatic hydrocarbon chemicals found in diesel fuels. Low aromatic concentration and exceedingly low sulfur level in F-T diesel fuel result in poor lubrication features of a fuel. To increase the lubricity of diesel fuels, commercial additives may be used. Manufacturers and batches might have different fuel characteristics. Specific synthesis factors, including temperatures, catalyst type, and syngas generation technique, may be used to adjust properties. Because of their higher n-paraffin concentration, F-T diesel fuels may have poor cold flow qualities. Post-processing of the gasoline allows manufacturers to modify its cold flow

qualities. Hydro-isomerization is one method that has been utilized to induce splitting [18]. An abridged list of fuel properties is presented in table (2.1) due to the enormous number of fuels discovered in the literature and in that table. In addition, the table shows the average qualities of conventional diesel fuel worldwide and the variety of additional Fisher-Tropsch diesel fuel specifications listed in Appendix table (A).

Table 1. Fuel characteristics of some Fisher-Tropsch and standard diesel fuel. [13]

Fuel	Density [kg/m3] @ 15°C	Viscosity [cst] @40°C	Flash Point °C	Cetane Number	Sulfur [ppm]	Pour Point °C	HHV [MJ/kg]
PetroSA (Feedstock: Natural Gas)	0.8042	2.98	97	48.9	<5%	<-60	46.69
Shell F-T (Feedstock: Natural Gas)	0.7845	3.57	109	>74 (above measurement capacity	Below the measurement capacity	0	47.11
Typical No.2 (Diesel)	0.8705	3.199	82	45.5	300	-8.1	45.6

2.2.1 Diesel Fuel

There is a paucity of high-quality, precise chemical kinetics data for heavy hydrocarbon ignition, which are crucial for the combustion modelling of compression ignition engines. Furthermore, with the widespread use of diesel fuel in different applications (trucks, trains, generators, boats, farms, and construction equipment) [1], a complete survey for each study that dealt with diesel's combustion characteristics since a lack of deep investigation must be considered along with the

fact that diesel consumption still represents. Diesel fuel is considered one of the low-pressure fuels. Therefore, it has low volatility in standard atmospheric conditions than other hydrocarbon fuels such as gasoline, making it more stable regarding safety storage. Today, diesel fuel is among the most commonly utilized crude oil fuels. Diesel fuel is often used in massive, high-output engines. Heavy-duty diesel engines power everything from commercial vehicles and SUVs to heavy equipment, front-end tractors and bulldozers, vessels of all sizes, and other industrial machinery [19]. However, some may claim that the environmental impact of diesel engines outweighs their fuel-efficiency advantages.

Diesel is distilled and produced during the crude oil refining process. Crude oil refers to any combustible liquid containing many hydrocarbon molecules, which is what crude oil is. The crude oil is heated to a higher temperature than usual to begin refining and cracking. Phase changes are seen in specific components when the temperature increases. The chemical composition of the liquid varies over time due to the varying responses of the various components to the temperature rise. Condensed gas-phase molecules are collected in a separate container. Crude oil may be divided into various "cuts" and put to various uses depending on the temperatures used to begin and conclude this process. A set of rules may define a distillate, yet each batch is unique. Figure (2) shows several distillation curves for standard fuels. At a certain temperature, the condenser recovers a specific volume of liquid. Fuels, including gasoline, jet fuel, and diesel, are all cut at temperatures between 50 to 350 °C, although kerosene and liquified petroleum gas are lower temperature cuts. Distilled from oil products, these are the most common forms of fuel [20].

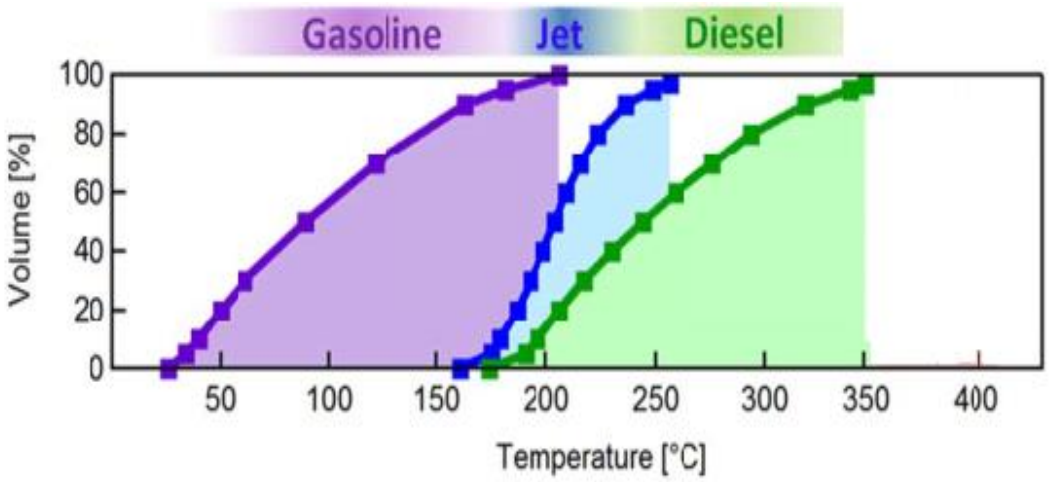

Figure 2. Typical crude oil inventories distillation curves [21]

As a result of its evaporation window's high temperature, the diesel cycle is difficult to understand. Diesel fuel burns at temperatures ranging from 700 K to 2500 K, at which point all of the fuel's constituents are in a state of equilibrium in the gas phase. The fuel must go through a phase transition before a combustion chemistry experiment can be carried out in the gas phase. The fuel must be heated to at least 400 degrees Celsius to ensure that it is entirely in the gaseous phase. Slow breakdown and pyrolysis are possible at these temperatures, even though oxidation is impossible (and probably does occur in the distillation process). The evaporation effect makes evaluating most peer-reviewed research on fossil fuel combustion difficult. Some experts believe that preheating the fuel may be an effective way to avoid this issue. [22]

As a consequence of overheating the fuel, the fuel will begin to disintegrate prematurely, while failing to raise the temperature to a sufficiently high level leads to fractional distillation. This may be true when doing experiments to determine ignition delay time, which is the time needed for the fuel to attain autoignition at a

given pressure and temperature [23], [24]. Few studies have been done on low-pressure fuels, which could be a valuable resource for validating Arrhenius models (illustrates how temperature affects the pace of physical and chemical reactions [25]). The information that does exist is dispersed. In figure (2), representative data is depicted.

2.2.2 Fuel from F-T or Gas to Liquid

The conversion during the chemical process, or what has called (GTL), is the inspiration for this clean alternative fuel. When a carbon-rich feedstock is transformed into a wide variety of synthetic fuels, the process is known as GTL. Natural gas, coal, or biomass can all be used as the raw resources for the final product. Gas-to-liquid production is on the rise, particularly in regions where natural gas is abundant. However, its sources are difficult to access or where excess gas is burned off into the atmosphere. Oil-producing countries have heavily regulated flaring and natural gas venting, so they are looking into developing cleaner GTL fuels. In order to alleviate fuel shortages and provide cleaner fuels and less pollution to the environment, many companies, including Shell, Sasol, and Chevron, are pursuing GTL production technologies.

German scientists Franz Fischer and Hans Tropsch invented the Fischer Tropsch (F.T.) process in 1923, which allowed natural gas to be transformed into a hydrocarbon mixture that could then be refined into oil products. Liquid petroleum products may be manufactured from natural gas, most notably diesel fuel, using the F.T. technology to replace traditional crude oil refining. GTL manufactures its products using the three-step production chain process: Syngas formation, Catalytic synthesis of syngas, and Cracking as a method of product creation [26]. Figure (3)

depicts a high-level view of the GTL formation process [27].

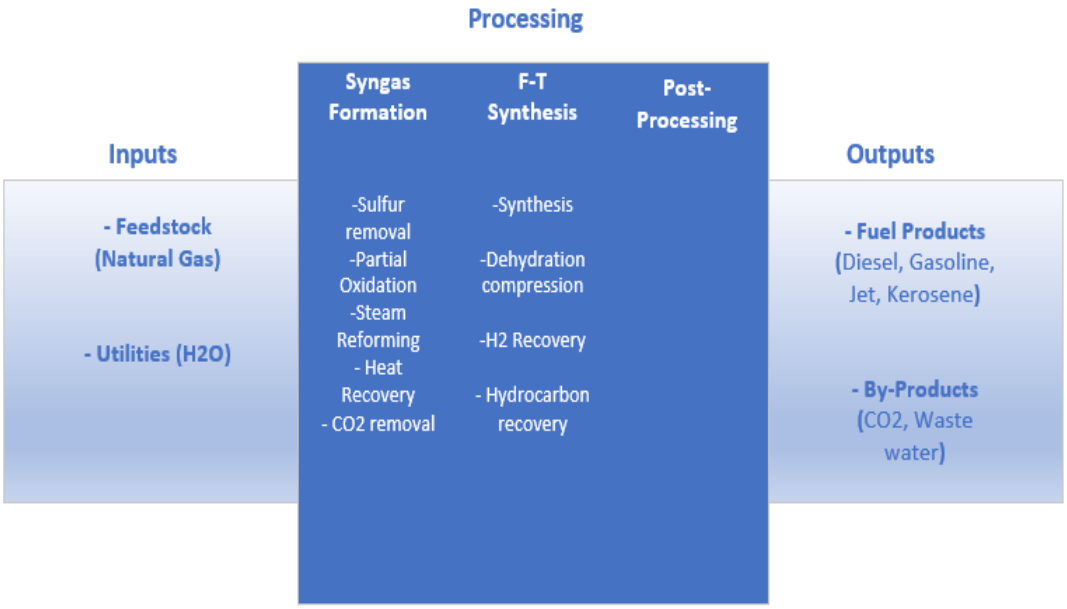

Figure 3. GTL fuels production process through Fisher-Tropsch technology [28]

In the first phase of the F-T GTL process, natural gas is converted to H_2, CO_2, and CO., primarily methane. Syngas is the name given to this mixture. Because of the risk of contaminating the catalyst with sulfur, water and CO_2, the syngas is cleaned prior to use. Carbon monoxide and hydrogen combine in the F-T reaction to produce various liquid hydrocarbons. After that, various refining techniques are used to turn these liquids into liquid fuels. Iron catalyzes the F-T reaction, which typically occurs at high pressures of 40 atm and temperatures of 500º-840ºF. An expensive reaction vessel must be built to handle these temperatures and pressures and produce the required volume of fuel or product. Different reactor designs (called "micro-channel reactors") and proprietary catalysts are being investigated by several companies as an alternative method for producing GTL at much smaller scales.

Table 2. Properties of different petroleum fuel products, including the GTL diesel (F-T diesel) [29]

Fuel	Chemical Formula	Net calorific value, MJ/L	Octane number	Cetane number
Oil Petrol	C_4-C_{12}	31.2-32.2	90-95	-
Oil Diesel	C_{15}-C_{20}	35.3-36.0	-	45-53
Oil naphtha	C_5-C_9	31.5	50	-
FT naphtha	C_5-C_9	31.5	40	-
FT Diesel	C_{12}-C_{20}	33.1-34.3	-	70-80
BioDiesel	C_{12}-C_{22}	32.8	-	51-58
Methanol	CH_3OH	15.4-15.6	110-112	5
DME	CH_3OCH_3	18.2-19.3	-	55-60
Hydrogen	H_2	8.9	106	-

The above table shows the main properties of GTL processing that may provide F.T. naphtha, F.T. diesel, methanol, dimethyl ether (DME), and H_2, all of which are appropriate for use in road transportation. The present research's primary objective is to examine and concentrate on GTL-diesel, a fuel that is intended to be used instead of conventional diesel fuel. Since both fuels have different combustion characteristics, it is necessary to compare their attitude, particularly the ignition delay time and see whether GTL may be used as an alternate fuel.

2.3 Performance parameters and Emission of F-T Diesel Fuels

Historically, there was much attention on the emissions data and the usage of GTL in engines as a primary fuel in previous reviews and studies. CI engines fuelled by conventional diesel, GTL, and GTL combined with conventional diesel were compared in performance data and exhaust pollutants. The performance and emissions of engines may be compared by blending biodiesel and alcohols with

GTL. An investigation of combustion characteristics has been conducted on a single-cylinder direct-injection diesel engine coupled with an electric dynamometer in the Heat Engine lab at Qatar University. The specifications of the used engine, fuel details, and a complete description of the testbed can be found in the publications [12], [30], [31]. The following sub-titles are the combustion characteristics, parameters of engine performance, and emission measurements discussed in the below sections. The study involved three alternative fuels to observe the effect of changing the fuel type on the combustion characteristics and emissions of the engine compared with those of conventional diesel that were tested in the previous study [32]. These fuels are; Gas-to-Liquid (GTL) fuel, waste cooking oil biodiesel and corn oil biodiesel. The GTL fuel was supplied by a local oil company (Qatar SHELL), while the waste cooking oil was obtained from the local market. For the corn oil, the corn seeds were dried in an oven at around 50 °C for 24 h. Once dried, the seeds were mechanically crushed, and oil was extracted. According to the ASTM standards, all the fuels and fuel blends were characterized in the Chemical Engineering Department lab at Qatar University. Pure fuels' main physical and chemical properties are listed in Table 2.3. It can be observed that GTL fuel has a lower density and viscosity and higher cetane number (C.N.) than diesel fuel.

On the other hand, corn oil has a higher density and viscosity and lower C.N. than diesel fuel. Finally, the waste cooking oil has comparable properties, in general, with those of diesel fuel, except that it has the lowest C.N. among all the tested fuels. This can be related to the fact that waste cooking oil is usually a blend of many vegetable oils. The waste cooking oil of the current study has been obtained from what is available in the local market. Therefore, its properties are related to the blend ratio of each component of this oil. Similar observations have been reported in previous

investigations working with waste cooking oils [33]–[36].

Table 3. Main properties of the pure fuel used. [37]

Properties	Diesel	GTL	Corn oil	Waste cooking oil
H/C Ratio	2.125	2.1–2.15	1.9–2.0	1.82
Approx. Formula	$C_{16}H_{34}$	$C_{16}H_{34}$	$C_{16}H_{34}O_2$	$C_{17}H_{31}O_2$
Density at 15 °C (kg/m^3)	866	760	915	863
Flash Point (°C)	55	77	270	160
Cetane No.	55	70	37.6	32.5
Calorific Value (MJ/kg)	44.3	47.3	36.3	42.7
Viscosity at 40 °C (mm^2/s)	5.2	2	45	4.9
Distillation Temperature (°C)	190–200	190	160	316

2.3.1 The maximum pressure rise rate (dP/dθ)

Figure (4) compares the selected fuels for dP/dθ. It can be noted that dP/dθ was found to be the lowest with GTL fuel, and the highest dP/dθ was obtained with the DGCW fuel blend. The dP/dθ of other fuels (Diesel, DG, D.W. and DGW) are close. The main properties that affect the physical ignition delay of any fuel are its viscosity, density and distillation temperature. However, for the chemical ignition delay, the C.N. is the responsible fuel property. Therefore, since GTL fuel has the highest C.N. and the lowest viscosity among all the selected fuels, as shown in Table 2.3, it is expected that dP/dθ of this fuel is the lowest due to the short ignition delay. It should be mentioned that the reduction in dP/dθ of the GTL fuel compared with that of the diesel fuel is about 18%. As the C.N. of the fuel decreases and the viscosity increases, dP/dθ increases due to the longer ignition delay. This can be observed in Fig. 4. Diesel, DG, D.W., and DGW fuels have nearly similar viscosity, density and C.N. Therefore, their dP/dθ are close. However, for the high viscosity fuel blend (DGCW), dP/dθ is the highest even though its C.N. is comparable to that

of the other fuels. The high viscosity of the fuel results in poor fuel atomization and big droplet size, which reduces the fuel-air mixing quality. This indicates that the effect of the physical ignition delay on the total ignition delay period is higher than that of the chemical ignition delay.

2.3.2 Peak pressure

The variations of the peak pressure for all the optimized manifold designs concerning the fuel type are shown in Figure (5). Theoretically, the in-cylinder pressure reaches higher levels as the engine load rises. The increase of load means more fuel injected, which leads to high pressures and temperatures inside the cylinder. Therefore, the trend in Figure (5) is the same as expected from the theoretical point of view. As the peak pressure increases, the I.D. decreases due to the improvement of air-fuel mixing. Good air-fuel mixing inside the engine reduces emissions [38]. The reduction of the peak pressure of diesel is about 7% on average lower than that of GTL. Therefore, the peak pressure values at high engine loads for diesel, GTL, and GTL blends are almost the same. The high C.N. of GTL is responsible for reducing ignition delay time, which leads to lower $dP/d\theta$.

In contrast, the high viscosity of diesel fuel controls the ignition delay by the injection of large droplets, which results in no well homogeneous air-fuel mixing and atomization. Poor atomization leads to incomplete combustion, which lowers the peak pressure inside the cylinder. It could be observed that, for most engine loads, the diesel–GTL blend has almost the same peak pressures as GTL fuel.

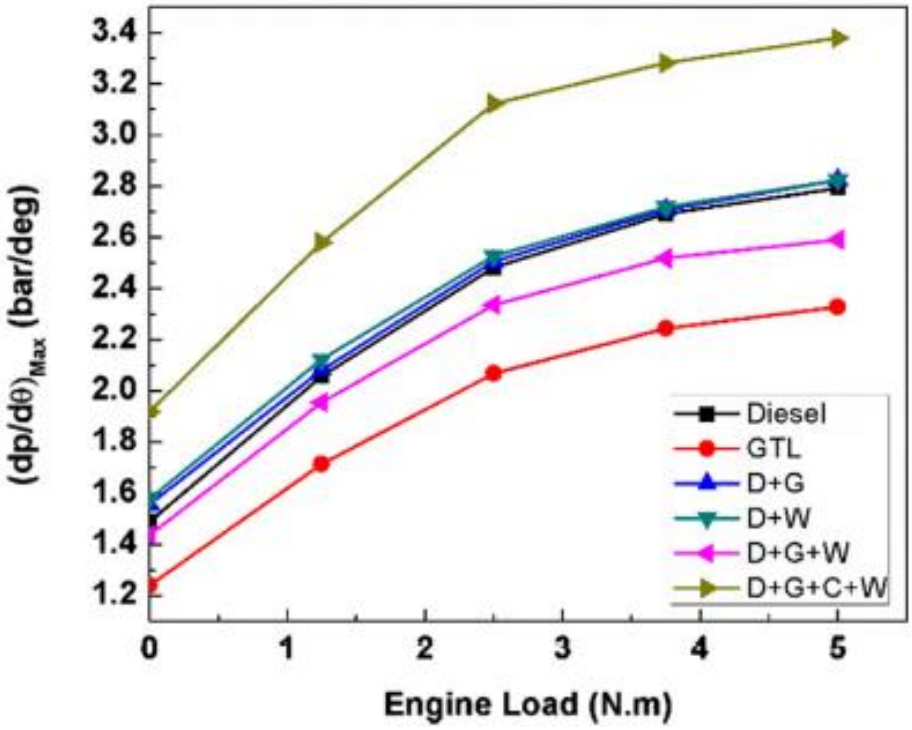

Figure 4. A comparison between the tested fuels using the 1D manifold for dP/dθ as a function of engine load. [37]

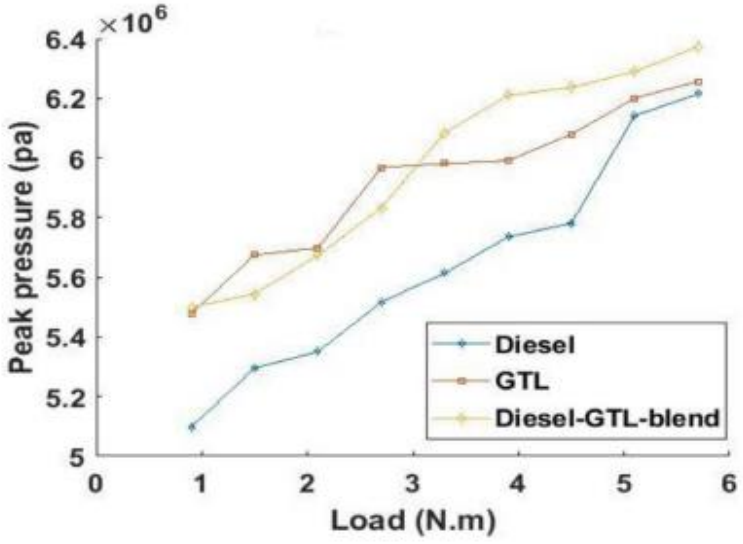

Figure 5. A comparison between the tested fuels for peak pressure as a function of engine load [39]

2.3.3 BSFC of the engine

Figure (6) shows the Brake Specific Fuel Consumption (BSFC) for diesel, GTL, and diesel–GTL blend as a function of engine load. For this manifold, the lowest BSFC was achieved by the diesel–GTL blend. The BSFC is inversely related to the calorific fuel value. However, it is hard to observe this relation, as the calorific values for the three fuels used are almost the same [43,44,46]. However, at high loads, the BSFC of diesel–GTL blend is about 30% lower than diesel fuel, which shows superior complete combustion over diesel fuel. This is also evident from the highest peak pressure generated from this fuel compared to diesel fuel, as shown in Figure (5). This is due to the fuel's reduced viscosity and increased C.N. content, compared with diesel fuel, which helps achieve a high degree of complete combustion and burns less fuel to get a certain amount of energy release [39]

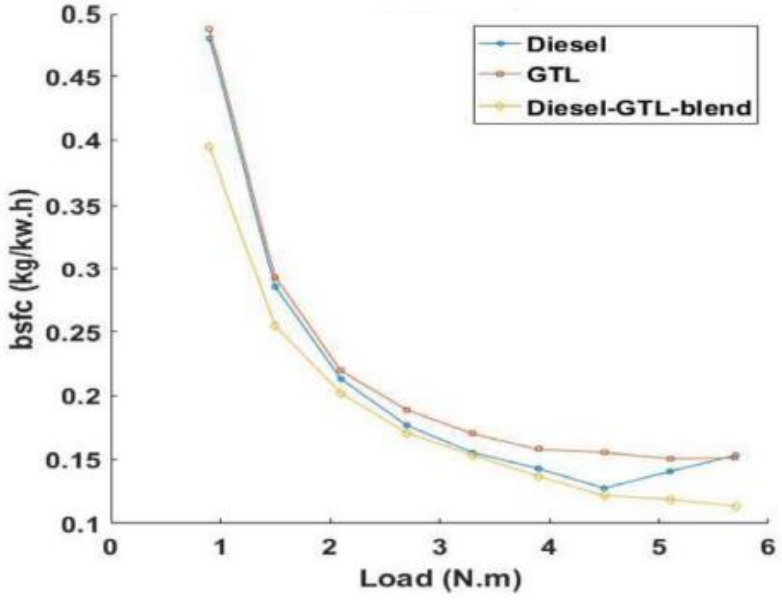

Figure 6. A comparison between the tested fuels for the brake-specific fuel consumption as a function of engine load. [39]

2.3.4 CO emission

As shown in Figure (7), it could be observed that the highest CO emissions were recorded when using diesel fuel compared to GTL and blended fuels. The high CO emissions for diesel fuel could be related to the high viscosity. The lower the viscosity, the more efficient is the fuel atomization, which leads to good air-fuel mixing and complete combustion. This is the case with GTL fuel compared with diesel fuel. The blended fuel had almost the same level of C.O. as GTL or slightly higher. This could be related to the viscosity and C.N. of the blended fuel, which are average between diesel and GTL. Moreover, these results demonstrate the significant advantages of blending diesel with GTL fuels. A high reduction of CO emissions was achieved by blending only 50% of GTL with diesel.

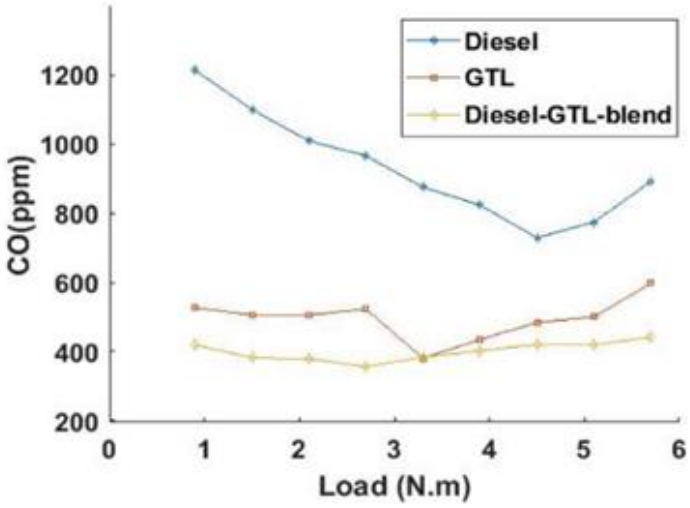

Figure 7. A comparison between the tested fuels for C.O. emissions as a function of engine load. [39]

2.3.5 Unburned Hydrocarbons emission

Hydrocarbon emission behaviours for all tested fuels are shown in Figure (8). It could be observed that the lowest H.C. emission was obtained with GTL and blended fuels. The H.C. emissions, in the case of diesel fuel, are about 70%

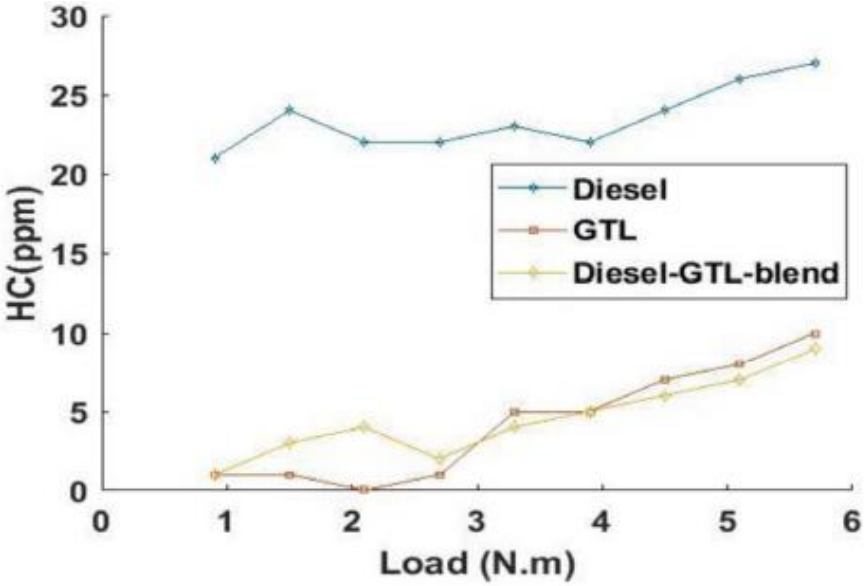

Figure 8. A comparison between the tested fuels for H.C. emissions as a function of engine load [39]

2.3.6 NO emission

Figure (9) shows the trends of NO emissions for all the tested fuels. The lowest NO emissions were achieved when using GTL and blended fuels. On the other hand, the highest reading was recorded for diesel fuel. GTL fuel has a high C.N., higher than 70, as shown in Table 2.3. A higher C.N. value results in a shorter I.D. and a lower peak pressure. The low peak pressure inside the cylinder leads to a low temperature, which contributes to forming NO. As the temperature inside the engine gets lower, the NO emission will be below. There was a reduction in NO emissions using GTL by about 50% rather than diesel fuel. However, in the case of diesel fuel, the growth in NO emissions signified the complete combustion process, which resulted in high peak pressures and higher temperatures inside the cylinder.

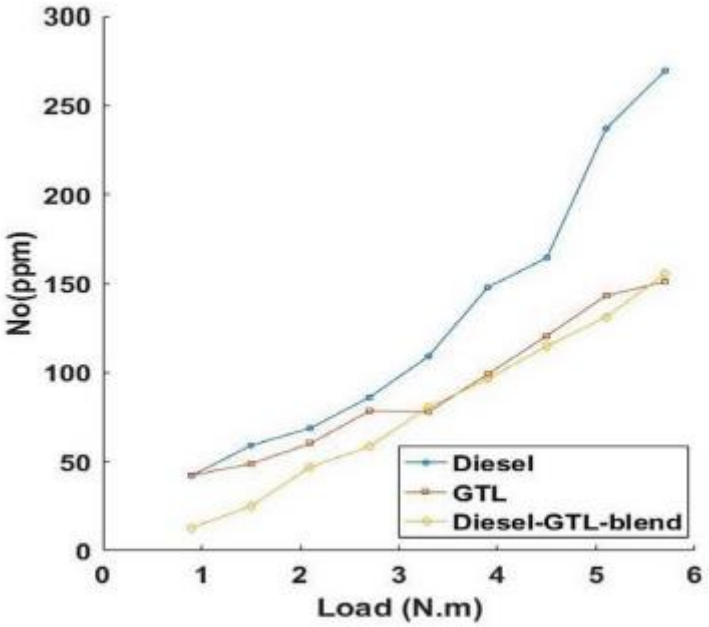

Figure 9. A comparison between the tested fuels for H.C. emissions as a function of engine load [39]

2.3.7 Smoke Emissions and Particulate Size Distributions emission

Of all emissions produced from a diesel engine, particulate matter (PM) is perhaps the most problematic. The conventional diesel combustion mechanism results in a relationship between soot and smoke opacity, which is affected by the absorption of elemental carbon [40][41]. Figure (10) compares smoke emissions between diesel and GTL fuels. GTL fuel reduced the smoke emissions considerably for constant speed and constant load operations. Figure (10-a) shows that using GTL fuel has managed to reduce the smoke opacity by about 60% at low loads and about 10% at high loads. With the increase in engine speed, Figure (10-b), considerable reductions with about 60–70% were obtained with GTLfuel.

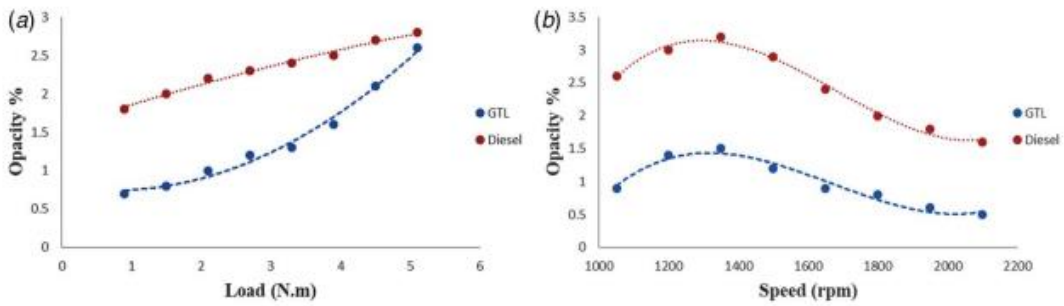

Figure 10. Smoke emissions for diesel and GTL at (a) a constant speed of 1800 rpm and (b) a constant load of 1.5 N.m [41]

Figure (10) shows comparisons between the two fuels for different PM sizes. It is evident from Figure (11) that the total numbers of PM had been reduced significantly for fins sizes with GTL fuel as a function of engine load; about 80% reduction for 0.3 μm (Figure (10-a)), 85% for 0.5 μm (Figure (10-b)), and 85% for 1.0 μm (Figure (10-c)) comparing with those with diesel fuel. However, for the coarse PM size, 5.0 μm, the total number of particles is comparable (Figure (10-d)).

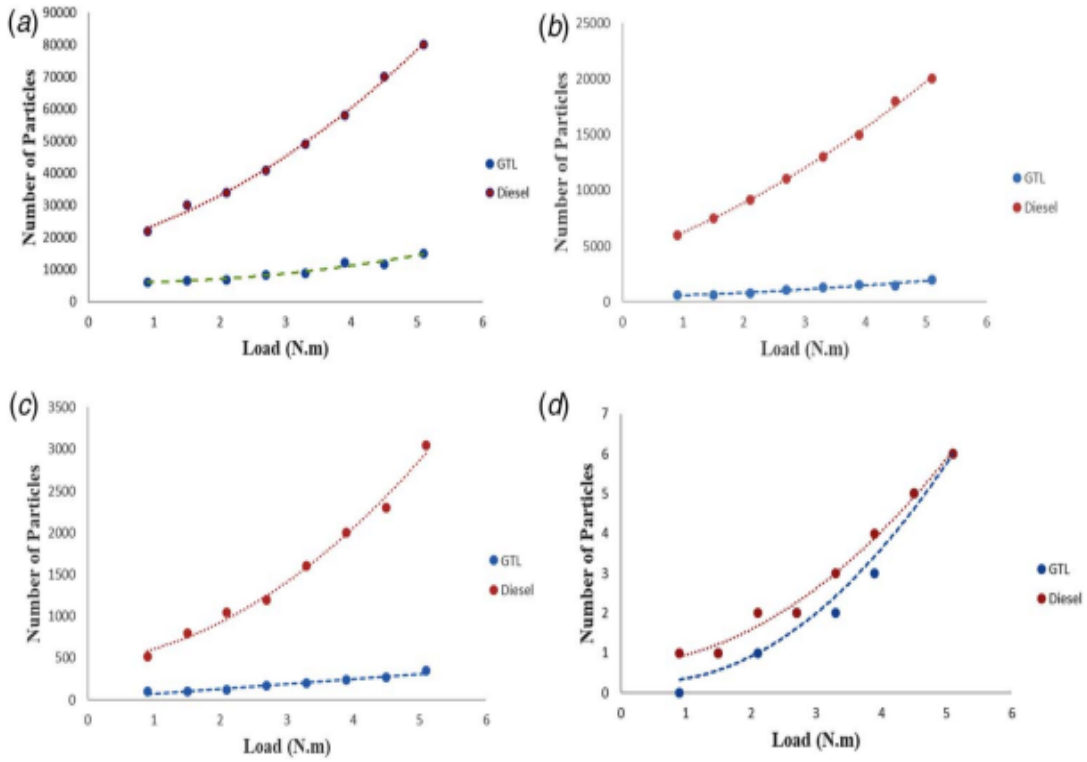

Figure 11. PM distributions at a constant speed of 1800 rpm for diesel and GTL fuels. Total number of PM that its diameter equal or less than: (a) 0.3 μm, (b) 0.5 μm, (c) 1.0 μm, and (d) 5.0 μm. [41]

2.4 Ignition Delay Time

The ignition delay (I.D.) measurement in Internal Combustion Engines (ICEs) is essential as this characteristic directly affects the engine's output power, emissions, and noise. For compression ignition (CI) engines, this phenomenon has received much attention whereby the combustion process is based on the non-premixed condition hence separate feeding of fuel and oxidizer. However, for Spark Ignition (S.I.) engines, the uncontrollable manner of some charge ignition that leads to the knocking phenomenon is problematic. The ignition delay time, which indicates the self-ignition occurrence for different fuels, is essential. The definition of I.D. time is

the time needed for the air-fuel mixture to reach the self-ignition (auto ignition) conditions or to detect the time interval between the start of ignition (a moment in which the injector needle is raised) and the beginning of combustion [42]. Ignition delay periods are a good measure of combustion reactors' overall conduct and are commonly utilized for precise chemical mechanisms as performance standards. However, the process of combustion initiation is challenging to be determined precisely; thus, the in-depth investigation of I.D. time is eventually one of the crucial aspects of scientists' efforts to study combustion kinetics for different fuels and various measuring techniques. The total ignition delay time depends on several factors involved in two phases: physical and chemical delay. The fuel first decomposes into tiny atoms and then evaporates and combines with air. As a result, fuel mist, air pressure, temperature, and speed affect the ignition delay. Therefore, the previous parameters should be considered when handling the fuel injection system design, combustion chamber design, and engine operating conditions). Simultaneously, the chemical delay wherein the influence of pre-combustion reactions is the main reason. Therefore, it is necessary to handle ignition delay by preparing the fuel before injecting it into diesel spray engines' combustion chamber and considering the optimum injection timing. The ID property can be defined as the time required to detect heat release once the air-fuel mixture reaches the self-ignition (autoignition) temperature and pressure or the time interval between the start of ignition (a moment) injector needle is raised up) and the start of combustion. Producing a flash of fire is very difficult to be detected precisely. However, scientists agreed that the best method for determining it is from the heat release slope, as per the figure (12) profile. It shows the diesel engine's heat release rate as a function of crank angle. There are three distinct phases of combustion, according to Heywood

(1988). The cylinder pressure rises fast for a few crank angles, and the combustion duration is brief. The first stage is known as the premixed phase. This is the primary heat release phase, which lasts around 30 C.A. degrees and is characterized by a progressive decrease in HRR. A minor but distinct HRR can be seen throughout the expansion stroke in this third stage of combustion, which corresponds to the tail of the heat release diagram.

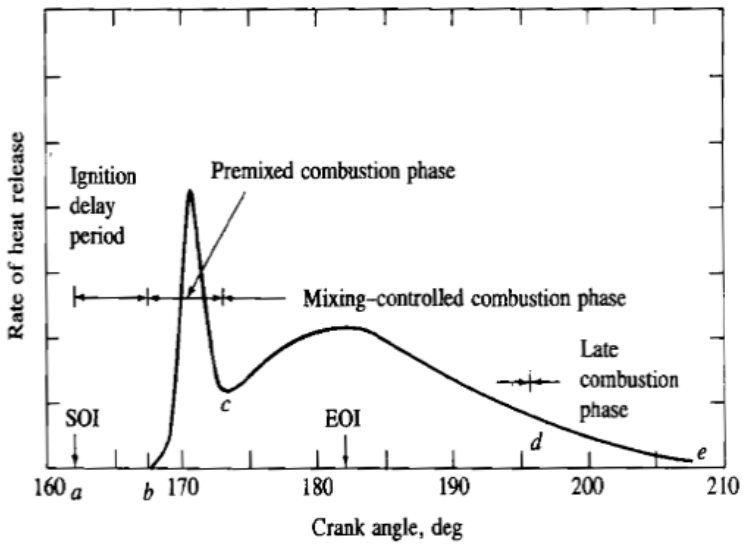

Figure 12. heat release profiles for IDI diesel engine [42]

For a historical demonstration of studying the ignition delay, several types of research have been carried out using different techniques such as constant volume bombs (CVB), Rapid Compression Machines (RCM) and Shock Tubes (S.T.). Shock tubes are used to measure I.D. in this dissertation, and more specifics will be provided in the following chapters. The RCM may also be used to investigate the chemical kinetics of fuels and, as a result, determine the ignition delay time. It may be used in low-to-medium-temperature auto-ignition circumstances. When it comes to light hydrocarbon fuels, the shock tube method cannot detect a duration of fewer

than 10 milliseconds, making this methodology ideal [43]. The RCM, on the other hand, may be programmed to restart an experiment (a repetitive process) more quickly than the shock tube approach. Compression strokes in internal combustion engines, in which an oxidizer-fuel combination is quickly compressed in an adiabatic compression chamber utilizing two pistons, are similar to this process. In this way, the properties of a reactive mixture, such as ignition delay, pressure tracing, and heat release, may be determined. A heated RCM was utilized to conduct an experimental examination of gas-phase autoignition of commercial diesel fuel, as described in various recent published publications [44]–[61]. The autoignition of commercial diesel has been demonstrated using the solid and dashed traced pressure curve, which led to the value of total and first phase ignition delay time directly from this representative pressure traced curve for conditions of stoichiometric diesel/air mixture and compressed pressure and temperature of 15 bar and 701 0K, respectively, as shown in figure (13) [62].

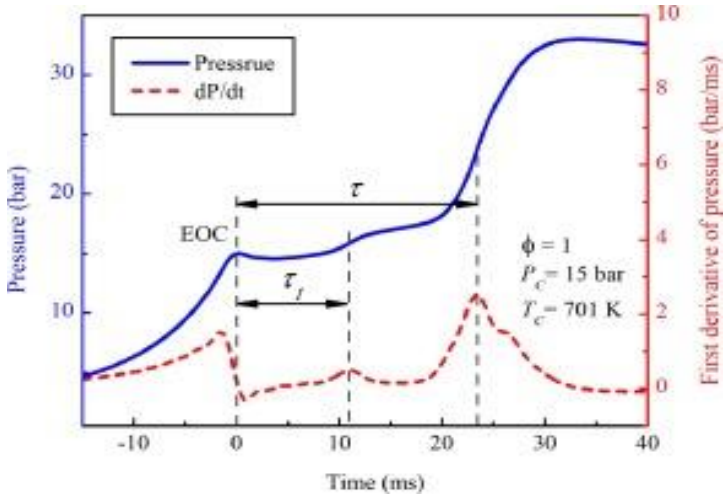

Figure 13. Ignition delay time for RCM [61]

2.4.1 ID Time of Diesel Fuel

The diesel ignition fuel has been studied extensively throughout the last century.

In 1938, Wolfer became the first to measure the diesel fuel I.D. time [63]. Numerous experiments employing constant volume combustion facilities [64]–[66], rapid compression machines (RCMs) [67], [68], flow reactors, and shock tubes [20], [69]–[71] have been carried out nowadays, yielding a variety of results on I.D. time. The absence of data on clean diesel fuel makes it difficult to compare ignition delay times for various kinds of diesel fuel over time and a shortage of data on pure diesel itself, given that most of past experimental attention has been on diesel surrogates. Kei et al. [67] used the rapid compression machine to study the behaviour of diesel ignition and applied the hot motor technique to detect the onset of the ignition. They observed that the dependency of the I.D. on higher temperature was low, and that was attributed mainly to the vaporization effect. A strong relation between their I.D. results in a fuel-air mixing rate for a temperature range below 750 ºK. Later in 1991, the spray injection method to investigate the I.D. time focused on the influence of Kown et al.'s residual gas fraction and composition or constant volume combustion bomb[64]. They figured out that It was discovered that repeated fuel injection had caused an increase in the bomb's residual gas percentage, and when the ambient mixture included less than 4% residual, the I.D. time was the shortest. Haylett et al. [70] investigated the ignition kinetics of diesel fuel (DF-2) in 21 per cent Oxygen gas diluted in Argon using an aerosol shock tube in 2009. These studies were carried out at pressures ranging from 2 to 8 atm, an equivalency ratio of 0.3 to 1.35, and temperatures ranging from 900 to 1300 K. Their heavy work on this study explain how to accelerate the evaporation of diesel which improved the homogenously of the diesel air mixture and then the diffusion process. After that, the same author [20] did second research in which several different diesel fuels were included. A variety of fuels were tested, including US DF-2, European DF-2, Low aromatic DF2, and

high aromatic DF2, to see which ones ignited best. Smaller derived cetane numbers (DCNs) have shorter ignition delay durations than more significant derived cetane numbers (DCNs). Before 2004, most of the published research had used either aerosol technique in shock tubes, rapid compression machines (RCMs), or direst engines, although other experiments have used flow tube reactors. Diesel surrogate sprays (P=41-118 atm, Φ=1) were examined by Kobori et al. [68] in an RCM. Clothier et al. [66] investigated diesel ignition delay durations in a single-cylinder gasoline engine converted to diesel operation (P=16 atm, Φ =1). Boiko and colleagues used shock waves (P=23 atm, Φ =1) to study the ignition of droplets (usually 2mm in diameter) behind them. A spray of light fuel oil (P=10 atm, Φ =1) sprayed into a shock tube was explored by Tsuboi and Kurihara [72]. In addition to the Hurn and Hughes [73] work on fuel-spray shock tubes for partly refined diesel fuels, Mellor et al. [74] mention further early work (P=35 atm, Φ =1). In a flow reactor, Tachina [75] researched the ignition of diesel fuel. Tevelde [76] and Spadaccini [77] employed a customized flow reactor with entirely evaporated flows to evaluate the ignition durations of diesel at increased pressures [76]. As shown in Figure 1.2, there is a wide variety of these pieces. Based on the correlation of Spadaccini and Tevelde [77], the data have been scaled by Haylett et al. [70] to 6 atm, and the equivalency ratio Φ =0.5 has been calculated for these experiments, which are plotted in Figure (14) below:

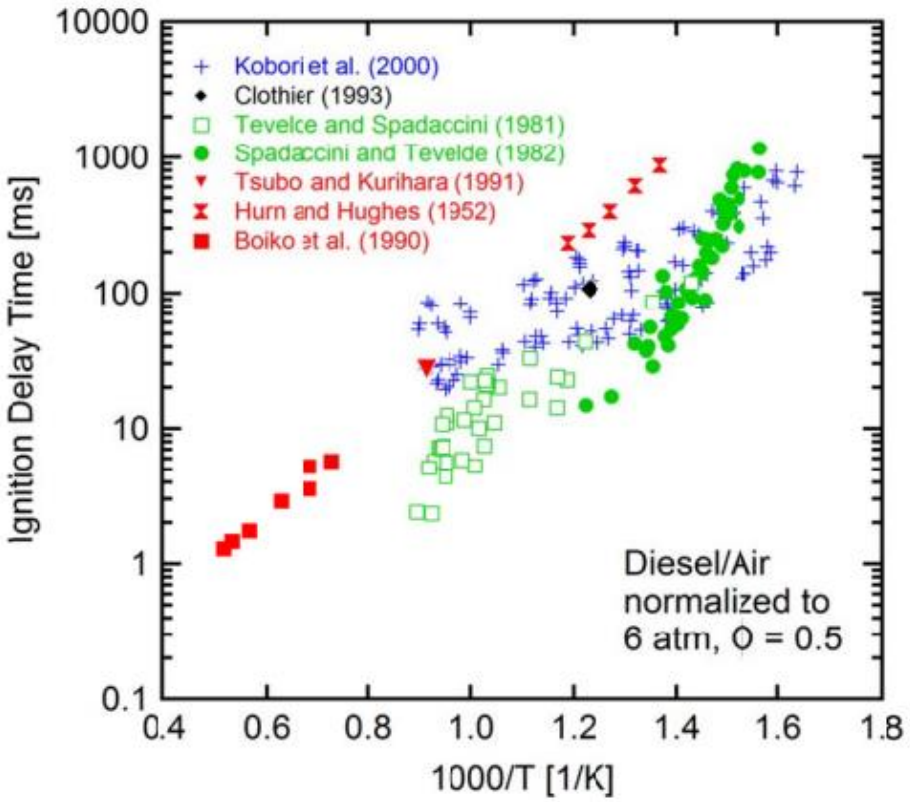

Figure 14. previous I.D. time measurements standardized to 6 atm and Φ= 0.5 [70]

It takes longer for the spray injectors in shock tubes and the RCM to create I.D. times than for the flow reactor data to evaporate and mix/diffuse the fuel/air combination. Table 4 outlines a few recent diesel fuel ignition investigations that have been conducted recently.

Table 4. Recent Diesel Fuel ID Studies

Ref	**Author**	**Fuel**	**Techniqu**	**Pressure [atm]**	**Temp [ºK]**	**Φ**
[78]	AGMB et al	St. diesel	Engine	1.2 int	300 int	N/A
[79]	Assad et al	St. diesel	reactor	4.7 – 10.4	1065 - 1838	0.5~2
[80]	Abdullah	Diesel+BioD	RCM	1100 inj	950-750	N/A
[69]	Davidson	DF-2	ST	6-60	1000-1400	0.85-1.15
[81]	Kukkadapu	FD9A	RCM	10-20	678-938	0.5-1.02
[71]	Gowdagiri	F-76	ST	10, 20	671-1266	0.5, 1.0
[79]	Penyazkov	DF-2	ST	4.7-10.4	1065-1838	0.5-2.0
[82]	Haylett	DF-2	ST	1.7-8.6	838-1381	0.1-2.0
[70]	Haylett	DF-2	ST	2.3-8.0	900-1300	0.3-1.35

2.4.2 ID Time of GTL Fuel

It is critical for the combustion community to study the start of auto-ignition in GTL fuel for gas turbine and internal combustion engines in the transportation sector. Autoignition begins when a set of thermodynamic circumstances is reached in which all of the combustible mixtures spontaneously and instantaneously ignite [83]–[86]. As far as auto-ignition goes, temperature and pressure are the most important factors to keep in mind for any given combination of fuel, oxygen, and diluent. A pressure transducer may detect pressure waves generated by the unburned gas when auto-ignition requirements are met. Auto-ignition happens when the unburned gas's circumstances, which cause the pressure waves, are similar to those found in a combustion system, such as those seen in internal combustion engines.

Kumar and Sung [82] studied the autoignition properties of GTL and conventional fuel/air mixes. They noticed a two-stage ignition delay response. They found that S-8 GTL creates a more robust flame than Jet-A in a laminar burning test [87]. Wang and Oehlschlaeger [84] tested numerous conventional and GTL fuels for igniting behaviour with a heated shock tube. At temperatures greater than 1000 K, the ignition delay times measured by GTL and JetA were almost identical.

On the other hand, lower temperatures revealed considerable variations between GTL and Jet-A fuels. Many organizations have attempted to establish a surrogate mixture for GTL fuels to imitate the combustion behaviour of GTL fuels. Huber et al. [85] generated GTL fuel surrogates based on the thermophysical characteristics and volatility data. Naik and coworkers [88] used the findings of Ji and coworkers [89] to forecast the GTL fuel's chemical kinetics model and compared it to the experimental data. The model adequately predicted GTL fuel laminar burning rates;

however, ignition delay time calculations were limited to very high temperatures due to a lack of data. Chemical kinetic models based on iso-octane/n-dodecane mixtures were developed by Dooley and colleagues [90] to simulate the burning of GTL fuels. Reports of the experimental data confirming the predictions of extinction limits and species concentrations were relatively accurate. Various experimental designs have been used to test the ignition behaviour, including counterflow burners, fast compression machines, and shock tubes [91]. Compared to traditional jet fuels, GTL fuel has far greater resilience to flame stretch effects and more robust combustion behaviour. The shorter ignition delay of GTL fuel compared to its conventional equivalents was the most striking aspect of its combustion behaviour. Atmospheric pressure or discrete intermediate pressures have been used in all investigations above; therefore, it is vital to highlight them. It has not been thoroughly tested under the same settings as internal combustion engines for GTL fuel's auto-ignition commencement. Table 5 outlines a few recent GTL fuel ignition investigations that have been investigated recently.

Table 5. Recent GTL Fuel ID Studies

Ref	**Author**	**Fuel**	**Techniqu**	**Pressure [atm]**	**Temp [ºK]**	**Φ**
[84]	Yu G et al	GTL surrogate	model	1.0 -10	885-1500	0.5,1.0, 2.0
[92]	Kitano et al	GTL JsNs	Engine	20 inj	N/A	N/A
[93]	Askari et al	GTL surrogate	CVCB	8-12	450 int	0.8-1.2
[94]	Choi et al	GTL+ BioDiesel	Engine	1600 inj	N/A	N/A
[95]	Joshua et al	GTL, DF2, Jet-A	ST	5-10	950-1250	0.5, 1.0

2.4.3 Fuel Ignition Quality

The principal reference fuel (PRF) for diesel is a blend of cetane and iso-cetane, a standard specification for a fuel's cetane number. The ID time of fuel is tested through an engine in a Cooperative Fuel Research (CFR) to determine its cetane number. Afterwards, the ignition delay period is set following a certain cetane and iso-cetane combination. Compared to cetane, iso-cetane has a longer ignition delay. Some 15 (the lower limit for cetane number is derived from alpha-methyl naphthalene (CN=0), which is the lowest constraint for cetane number). The cetane number of a mixture is calculated as the weighted average of the cetane numbers of its constituents. Based on Heywood [42], cetane number (C.N.) is given by:

$$CN = percent\, n-cetane + 0.15 \times percent\, HMN \quad (1)$$

Where HMN is the ratio of isocetane heptamethylnonane which has a very low ignition quality. High cetane numbers are a characteristic of F-T diesel fuels, with a high n-paraffin concentration. Compared to other F-T diesel fuels, PetroSA's fuel has a lower cetane number because it contains less paraffin. Although the cetane scale extends up to 100, several of the cetane figures in Table A in the appendixes are recorded as >74. This is because it is the top limit of ASTM D613 requirements for working standards [18]. The ID is highly affected by the C.N. Combustion processes may spread across a larger area if the delay period is less than long. As a result, diesel knock may be prevented, and emissions can be reduced due to a better-regulated heat release rate and pressure increase. Fuels with a high cetane number have a short ignition delay. Measuring the fuel ignition delay time is possible by precisely a CVCA (Constant Volume Combustion Apparatus) [66]. As seen in Figure 15, the ignition delay vs cetane number is shown. The ignition delay is

inversely proportional to the cetane rating [96].

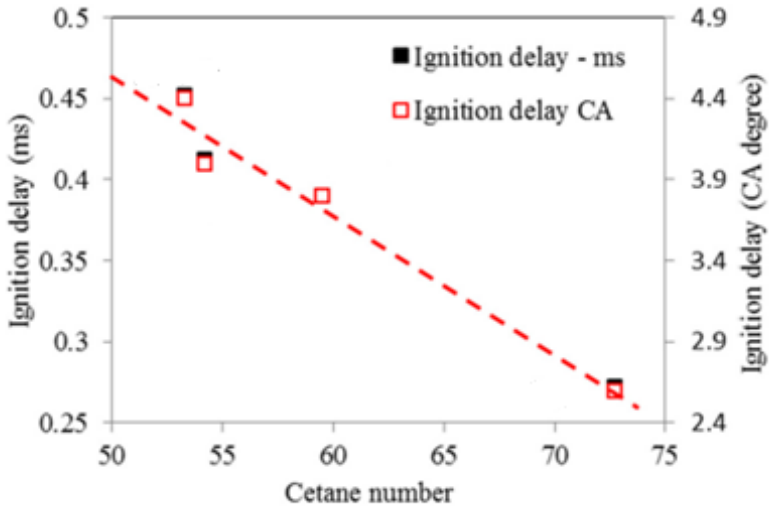

Figure 15. The fuel cetane number affects ignition delay time.[96]

Finally, to conclude this chapter, the only investigation of GTL diesel fuel that has been conducted is the study conducted by Joshua et al. [93]. Because using a shock tube, the authors were able to evaluate the ignition delay time across a wide temperature range. In contrast, they performed their studies for the lean combination (=0.5). However, they did not investigate the mixture's stoichiometric or rich conditions due to the challenges of attaining test durations longer than a few milliseconds and the non-idealities associated with the testing facilities. In the present study, the three conditions of the air-fuel combination are covered for a range of intermediate temperatures between (980 and 1120 K) and the same range of pressure up to 20 bar. The temperatures and pressures studied are 980 to 1120 K and (6, 10, 14, 20) bar, respectively. In addition, a combination of diesel and GTL is being examined to see whether there are any dire impacts, so it would be recommended that it be utilized and have the advantages of both diesel and GTL.

CHAPTER 3: SHOCK TUBE FACILITY FOR IGNITION DELAY MEASUREMENT

3.1 Introduction

The shock tube has gained widespread acceptance as an experimental instrument for studying reactive gas mixtures' chemical kinetic behavioral patterns in a confined space. It has been used in several research papers since its development in the early 1950s. With the availability of shock tubes, special reaction rates, ignition delay times, and other combustion characteristics have been completed to investigate several fuels. It comprises two sections, the high-pressure driver and the low-pressure driven section, divided initially by a diaphragm. Then, the driver portion is pressured to a level of a pressure value sufficient to produce the diaphragm to rupture, resulting in the generation of a shock wave that moves throughout the driven section.

3.2 Fundamentals of Shock Tubes

Shock tubes are constructed of a rigid tube with a diaphragm at the beginning, which divides the driver gas from the test gas or driven gas in the shock tube's first section. Other names for high and low-pressure spaces include compression chambers and expansion chambers, which are two different types of chambers [97]. When the diaphragm abruptly bursts, an incident shock wave is generated and propagates through the test gas, elevating the temperature and pressure of the gas in question. As the shock wave travels through the test gas, a rarefaction wave is created, which travels back into the high-pressure gas at the speed of sound and reflects off the driver endwall when it reaches the driver endwall. The "contact surface," which travels down the tube behind the shock front, is where the test gas

and the driving gas touch. Shock waves strike the end wall and reflect into the test zone, boosting the temperature and pressure of the shocked gas in the test region.

Consequently, the energy release and chemical reaction begin, culminating in the occurrence of an ignition. The experiment comes close when the expanding fan reaches the driven tube endwall or when the reflected shock interacts with the contact surface, whichever comes first, and the experiment is over. Testing periods in the shock-tube trials are often just a few milliseconds, which is typical. Usually, the diaphragm is assumed to rapture at t = 0, and before the rapture, only two regions exist, 4 and 1, which indicates the high and low-pressure regions, respectively. After the rapture, a compression wave is developed in the driven section (low pressure), generating region (2) behind it. In addition to the compression wave, an expansion wave is formed at the driver section lowering its high-pressure value and forming a new region (State 3). Next, the compression wave is reflected from the high temperature and pressure of the driver end-wall, creating a region (5). Finally, the expansion wave is also reflected when it reaches the driver's left end and significantly increases pressure and temperature. The region behind the reflected expansion wave is illustrated as Stage 6 in Figure (16). The flow pressure of the shock tube, alongside its temperature changes, is shown in Figure (17) using a schematic approach. Eventually, all the regions will reach a steady-state condition with constant pressure and temperature throughout the inner volume of the S.T.

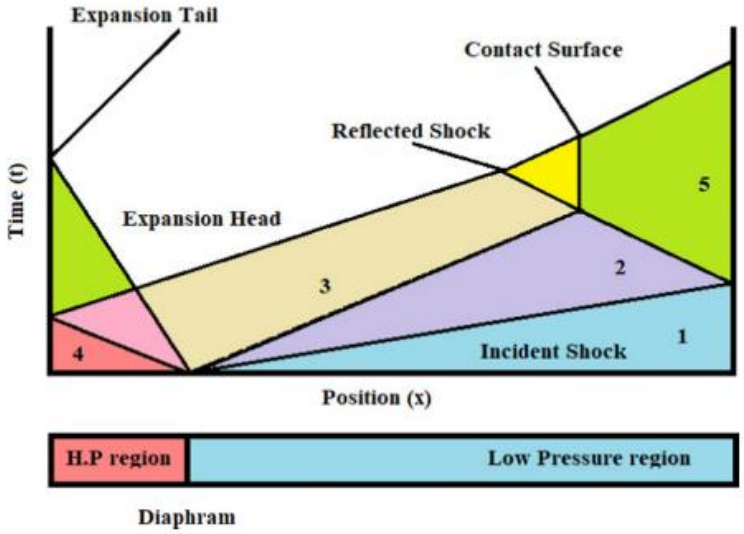

Figure 16. Shock tube ideal flow (reproduced from Ananthu and Asok Kuma [79])

Discussion of shock tube theory has been restricted to shock tubes with circular cross-sections propelled by compressed gas. The Rankine–Hugoniot relations describe the thermodynamic parameters on both sides of the shock front (also known as the jump conditions). By assuming inviscid flow and compliance with an ideal gas equation with constant specific heat. Equations below are the governing equations for the conservation of mass, momentum, and energy:

$$\rho_2 u_2 = \rho_1 u_1 \tag{2}$$

$$P_2 + \rho_2 u_2^2 = P_1 + \rho_1 u_1^2 \tag{3}$$

$$\frac{P_2}{\rho_2} + e_2 + \frac{1}{2}u_2^2 = \frac{P_1}{\rho_1} + e_1 + \frac{1}{2}u_1^2 \tag{4}$$

There are four variables in these equations: P (pressure), u (velocity), ρ (density), and e (internal energy). It is possible to rearrange a gas equation for the conservation equation (Pv=RT).

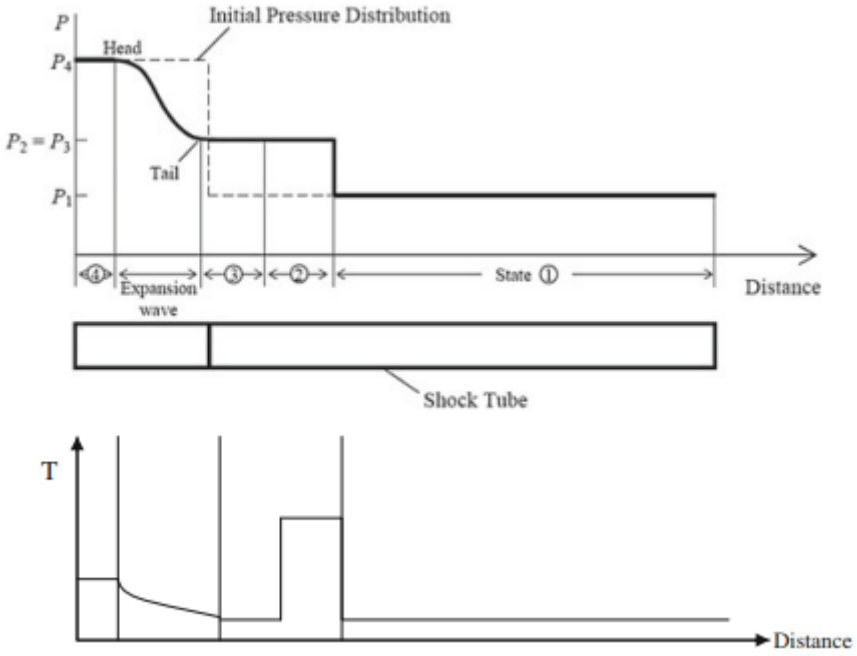

Figure 17. instantaneous pressure alongside temperature transients within a shock tube is shown schematically. [99]

3.3 Shock Front Flow Relationships

The 1D conservation equations for mass, momentum, and energy for an ideal gas, which is a logical hypothesis for several gaseous with modest pressure and temperature fluctuations along with the head of the shock, may be used to derive these correlations [100]

$$\frac{P_2}{P_1} = \frac{\frac{\gamma+1}{\gamma-1}\frac{\rho_2}{\rho_1} - 1}{\frac{\gamma+1}{\gamma-1} - \frac{\rho_2}{\rho_1}} \quad \textbf{(5)}$$

where M_S indicates the shock wave incident Mach number, u and ρ symbolize gas velocity and density, index 1 represents pre-shock circumstances, and index 2 implies post-shock conditions. is the ratio of a gas's specific heat capacity. The

following two equations show the pressure and temperature fluctuations along with the head of the shock:

$$\frac{P_2}{P_1} = 1 + \frac{2\gamma}{(\gamma+1)}\left(M_s^2 - 1\right) \qquad \textbf{(6)}$$

$$\frac{T_2}{T_1} = 1 + \frac{2(\gamma-1)}{(\gamma+1)^2}\frac{\gamma M_s^2 + 1}{M_s^2}\left(M_s^2 - 1\right) \qquad \textbf{(7)}$$

The initial pressure ratio P4/P1 and the subsequent incident shock Mach number, Ms, may be calculated using the formulae mentioned thus far. It's as follows:

$$P_{41} = \left[1 + \frac{2\gamma}{\gamma+1}\left(M_s^2 - 1\right)\right]\left[1 - \frac{\gamma-1}{\gamma+1}\frac{a_1}{a_4}\left(M_s - \frac{1}{M_s}\right)\right]^{-\frac{2\gamma}{\gamma-1}}. \qquad \textbf{(8)}$$

P5/Pl and T5/T1 may be expressed as a function of Ms1. The following formulae are established by combining the previous two equations (P2/P1) and (T2/T1).

$$\frac{p_5}{p_1} = \left[\frac{2\gamma_1 M_{s1}^2 - (\gamma_1 - 1)}{\gamma_1 + 1}\right]\left[\frac{-2(\gamma_1 - 1) + M_{s1}^2(3\gamma_1 - 1)}{2 + M_{s1}^2(\gamma_1 - 1)}\right] \qquad \textbf{(9)}$$

$$\frac{T_5}{T_1} = \frac{[2(\gamma_1 - 1)M_{s1}^2 + 3 - \gamma_1][(3\gamma_1 - 1)M_{s1}^2 - 2(\gamma_1 - 1)]}{(\gamma_1 + 1)^2 M_{s1}^2} \qquad \textbf{(10)}$$

The above set of equations represents how to find the conditions through all phases of the transient flow of the shock wave.

3.4 Literature Review of Various Shock Tubes

Various shock tubes have been and are still being utilized across the globe during the last century; Chapter one of [101] provides a historical overview of investigations on shock and blast wave phenomena. As early as 1899, a French scientist named Paul Vieille conducted the first shock-tube studies, which focused

on varying diaphragm materials and driving gases. However, it was not until 1946 that Payman and Shepherd published their first important paper on the shock tube [102] There are many uses for the contemporary shock tube discussed in this paper. They also discovered that the diaphragm thickness, the length of the driver and driven tubes, and the molecular weight of the driving gas are all essential factors in shock tube experiments. Refer to Gaydon and Hurle's well-known book on shock tubes for further information on the history of shock-tube development. (1963). Figure (18) shows a schematic of historical works for S.T.s until the 20th century.

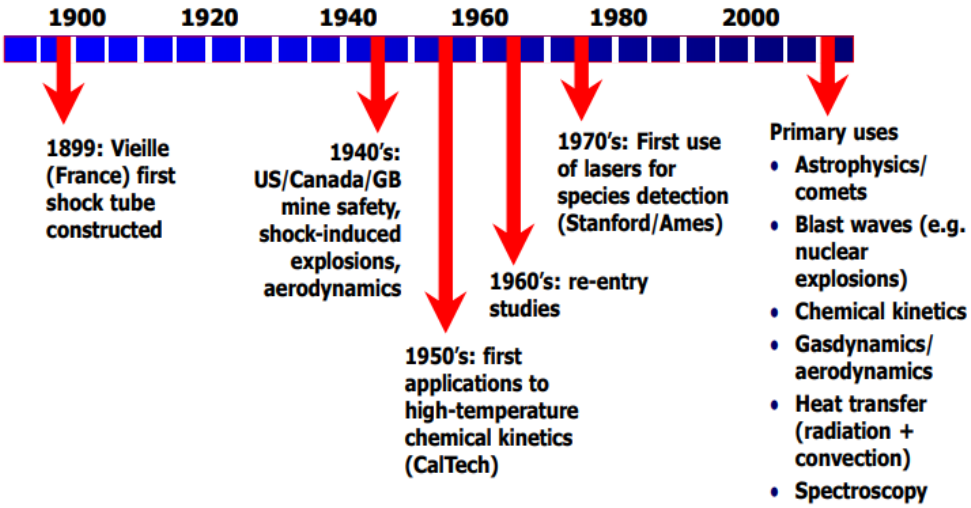

Figure 18. historical progress of S.T.s usage. [102]

A shock tube is the most practical and safe means to create regulated shock/blast waves in labs. The flow is to be identified and created within the heated tube (test section), determines the shape and size (geometry parameters) and the range of beginning conditions to be employed (P and T). Following is a short overview of a few standard shock tube designs and a summary of investigations completed in these shock tubes. The authors chose the mentioned tubes based on their knowledge at the time.

3.4.1 Shock Tube [UTIAS], Canada

University of Toronto Institute for Aerospace Studies (UTIAS) built the UTIAS combustion-powered hypersonic shock tube to mimic the high enthalpy, actual gas flow characteristic in hypersonic flight. Combustion drivers can deliver shocks at velocities up to 7 Km/s. The Institute for Aerospace Studies at the University of Toronto, Canada, constructed it in 1964. A quick explanation of this tube follows; a more in-depth description may be found in Boyer's article [103]. Even though it was designed to generate high-velocity flows, it may be used to analyze shock waves with Mach numbers as low as one and as high as roughly 20. There is no requirement for a flammable gas combination while investigating flows formed behind weak/moderate impact shock waves with Mach numbers less than 5, and conventional high-pressure gases emitted from compressed gas containers are employed instead. BenDor used a wide range of starting conditions in his experiments, which you can see in Table (6) below:

Table 6. Initial conditions of UTIAS [102]

Driven section gas (N_2)			**Driven section gas (Ar)**		
Incident Mach	**P4/P1**	**Driver gas**	**Incident Mach**	**P4/P1**	**Driver gas**
2.0	110	CO_2	2.0	60	CO_2
3.7	220	He	3.0	70	He
4.8	690	He	4.4	350	He
6.2	800	He	5.2	800	He
7.0	1550	H_2	6.1	520	He
7.8	3320	H_2	6.9	1000	H_2
			7.9	1900	H_2

3.4.2 Shock Tube [Prefectural University], Japan

The drag coefficient of a tangible item in a gaseous medium must be known to

evaluate its mobility. Shock tubes have been used in experiments to estimate the drag coefficient of a solid sphere travelling through a fluid, among other ways. Shock waves were used in these investigations, and the movement of the spheres was tracked. We determined the appropriate drag coefficient by looking at the recorded sphere trajectories. Technical difficulties emerge while doing shock tube studies, such as protecting the object of study from contacting the tube walls. The following explains Suzuki et al. [104] proposed solution. Experiments were performed in a horizontal shock tube shown schematically in Figure (19) to determine the sphere's drag coefficient in a nonstationary movement. 75 cm long and 11 cm inside diameter with a cross-section area of 7.5 cm^2 for the test section; the driver part had the same length.

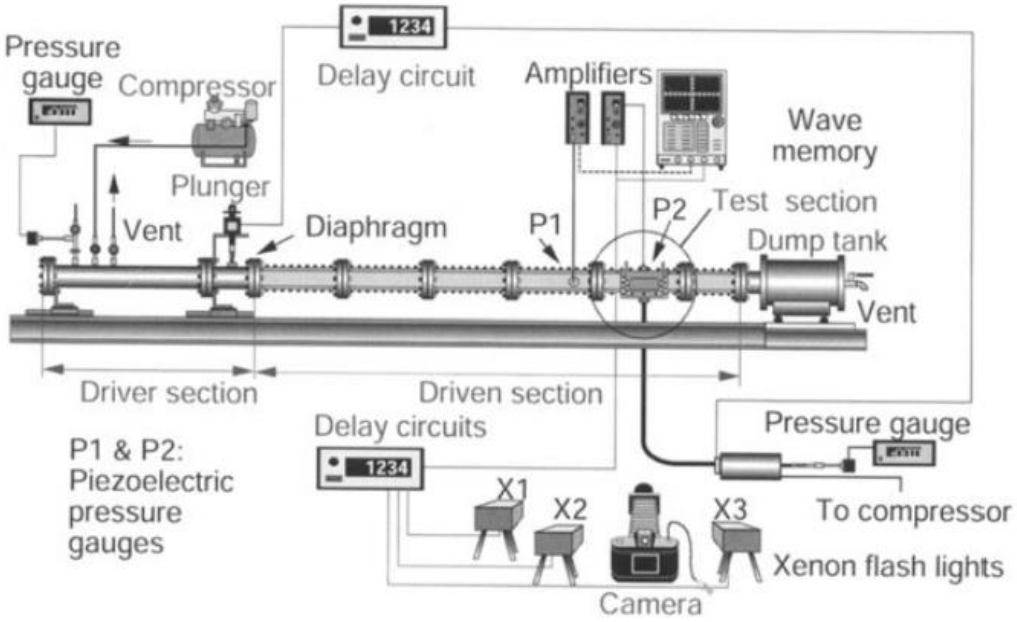

Figure 19. schematic of the described shock tube in section 3.4.2 [103]

3.4.3 Ben Gurion University Shock Tube, Israel

There are seven different shock tube systems at Ben Gurion University's Shock Tube Laboratory for performing various studies. Each apparatus has its specifications of orientation, cross-section geometry and section lengths. Starting with mitigation of shock wave experiments, passing through testing of shock reflection phenomenon and finally structure study of the blast waves. Table (7) summarizes the tube specifications. For example, Figure (20) shows the vertical, 4.5-meter long shock tube that was updated and completely automated using a quick opening valve between the driven and driver tubes.

Table 7. Characteristics of Ben Gurion University Shock Tube [105]

Experiment	**Maximum Mach**	**Orientation**	**Cross-Sestion dimension [cm^2]**	**Driver length (m)**	**Driven Length (m)**
ST-01sh	1.7	Horizontal	8×8	2.0	3.5
ST-02sv	5.0	Vertical	8×8	2.0	4.5
ST-03ch	2.0	Horizontal	Dia=20 cm	2.0	8.0
ST-04sv	1.8	Vertical	3.2×3.2	1.0	1.5
ST-05sv	2.0	Vertical	3.6×3.6	1.5	3.5
ST-06sv	2.5	Vertical	5.6×5.6	1.5	3.0
ST-07sv	2.0	Vertical	25×12.5	2.0	6.0

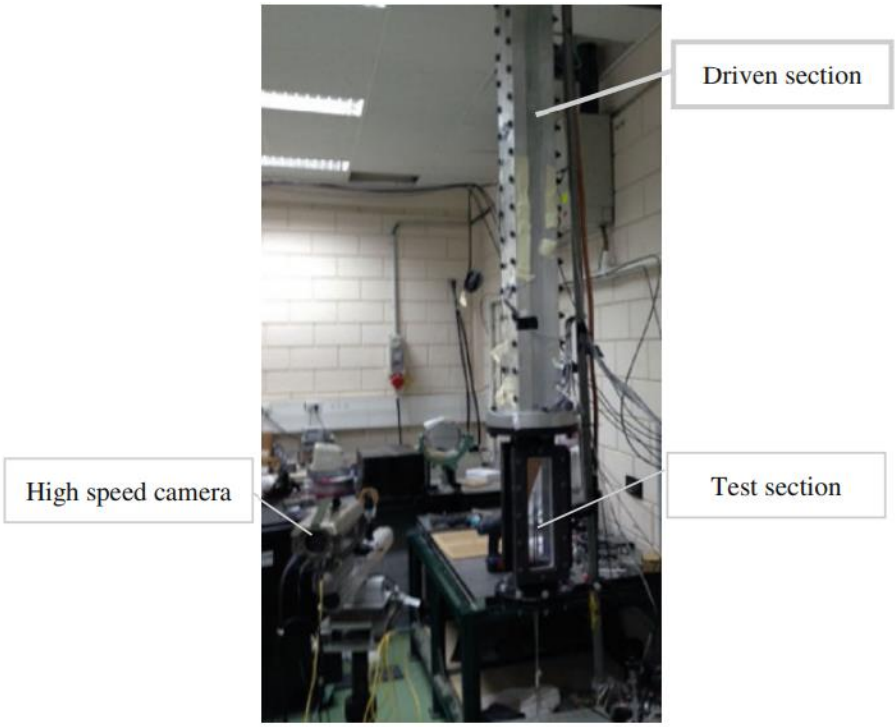

Figure 20. schematic of the described shock tube (ST-02sv) in section3.4.3 [104]

The following table (8) summarizes various shock tubes around the world and shows the main features of geometry and shock conditions

Table 8. Review of Shock Tubes

Ref	Affiliation	Driver length	Driven length	Main Features
[106], [107]	Ernst Mach Institute	150 cm	380 cm	An experimental was employed shock tube that produced shock waves in 1 to 5 Mach to explore various shock wave patterns.
[108]	Aix-Marseille University	1.5m	5.04m	Allows for the study of flows without the influence of wall boundary layers.

[100]	Russian Academy of Sciences	3m	13m	employing hydrogen as the driving gas at temperatures up to 750 K and pressures up to 500 atm
[109]	Texas A&M University	2.24m	4.72	High-Pressure Shock Tube with different diaphragm material usage and having long test times for the runs up to 50-atm
[110]	Texas A&M University/Qatar	6.6m	5.2m	Aerosol Shock Tube, Using an external holding tank, a set amount of aerosol was injected into the driving part of the shock tube.
[111]	Stanford University	7various lengths	7various lengths	The new aerosol loading scheme uses two large S.T. gate valves, a mixing plenum and dump tank, and plug flow loading. Laser diagnostics (U.V. to MIR) provide fuel loading, uniformity measure, and species concentration time-histories
[112]	KAUST	3-9m	9m	Two types of S.T.s low-pressure S.T., are designed to reach reflected shock pressures of 1 - 20 bar and temperatures of 500 – 4000 K, and high-pressure S.T.

3.5 Improvements in S.T.s design

3.5.1 Diaphragm

A shock wave is generated when the diaphragm separating the driver and driven

portions ruptures. The diaphragm is punctured with a needle, or a differential in pressure may be created. In order to simulate spontaneous rupturing of an aluminium or iron metal diaphragm, it is advised that the diaphragm be scraped across. In 1962 [95], Bradley suggested using the cross-scratched layer design to avoid the reproduction of spontaneous rupturing in the case of the flat layer. Figure (19) illustrates the layer rupture shapes for the cross-scratched diaphragm.

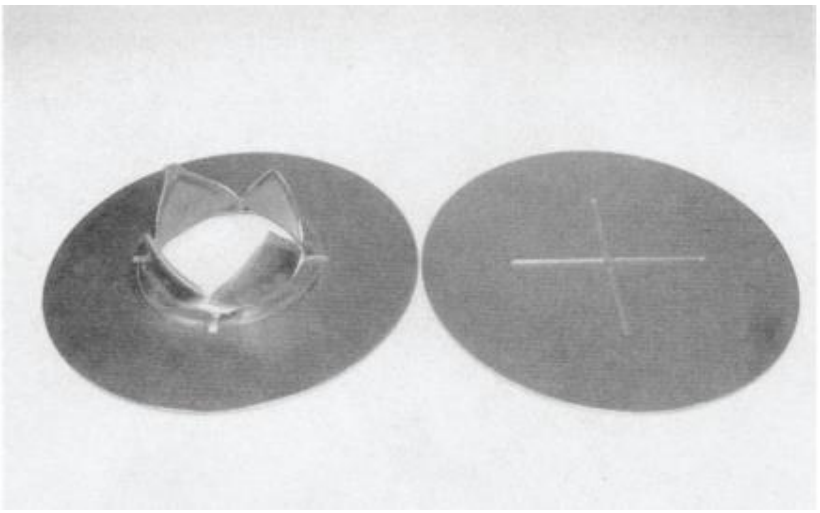

Figure 21. Diaphragm before and after rupture of cross-scratched layer [95]

Diaphragm-less shock tubes with fast action valves have been recommended because of their outstanding repeatability and quick turn-around time for experiments [113]–[116]For example, in the shock Mach number range of 1.1 to 2.5, Kim (1995) [117] reports shot-to-shot repeatability in shock speed of better than 0.2 % scatter utilizing air as both the driver and driven gas.

3.5.2 Variable Cross-Section STs

With a powerful shock wave projected, a driver portion bigger than a driven part was contemplated [118]–[122]. Alper and White (1958) [123] calculated the Mach number of shock waves produced in the driven portion for varyindriver/driven gases

configurations. Their findings are shown for four alternative cross-sections of the driver and driven cross-section. The authors found that the Mach number of a shock wave may be raised by up to 1.1 times if the cross-sections of the driver and driven portions are equal.

3.5.3 Aerosol S.T.

The Aerosol shock tube as in figure (22) is designed to meet the challenge of having the test conditions when examining the liquid fuels. However, maintaining a regionally uniform dispersion of the aerosol test composition is the fundamental problem when researching aerosols in shock tubes. A non-uniform aerosol concentration may degrade shock tube results, as was the case in previous research [70], [124]–[126]. Remember that the heated S.T. method would include heating the shock tube and mixing assembly to allow for a more significant fuel vapour pressure in the system. When the fuel temperature is too high for an extended period in the shock tube or mixing tank, the issue with this approach manifests itself prior to the shock start. Preparation for the combustion experiment, including mixing and filling the shock tube, will cause the fuel to disintegrate prior to the start of the experiment.

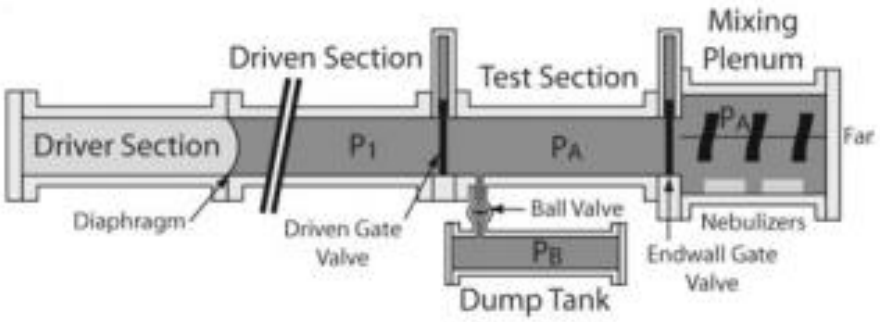

Figure 22. illustration of the aerosol S.T. [69]

The following is the technique for filling the shock tube, To begin, a combination of

oxidizer and diluent is used to establish the gas pressures in all volumes (with all valves closed). The pressure in the mixing plenum and the shock tube test section is adjusted to $P_{.A.}$. The dump tank's $P_{.B.}$ pressure is lower than $P_{.A.}$'s. When the dump tank ball valve is opened, and the pressures in the other streams equalize, the pressure in the whole of the driven section is adjusted to the specified target pressure P1. Then comes the aerosol concoction. A fan within the aerosol mixing tank mixes the whole volume. The fan has six blades evenly distributed along the axis of rotation and spins at about 100 rpm. Then an ultrasonic nebulizer array creates liquid droplets that rapidly catch up in the mixed flow. This is done until the liquid loading in the mixed gas reaches a desirable level. Then they are switched off. Large droplets may then settle. Third, the test part of the shock tube receives the aerosol composition. There is no flow through the endwall gate valve since the pressure difference over it is zero. When the ball valve in the test section has been opened, gas may flow into the dump tank from the test section. The aerosol mixture is pulled into a plug flow from the test portion into the dump tank as gas flows through it. The aerosol mixture is sent into the dump tank through a ball valve. Currently, the driven segment gate valve does not experience any pressure change. Close the endwall gate valve and the ball valve to prevent any flow. Smooth-walled tubes with a homogenous aerosol approaching the endwall are produced.

3.6 Diagnostics and Visualization

There were outcomes from tests done in shock tubes given when discussing various shock tubes. After that, surveying some of the techniques and procedures utilized to achieve these and other comparable outcomes.

3.6.1 Pressure Transducers

Dynamic pressure gauges with a fast reaction time (approximately 1μs) are often used in shock tubes. Like PCB transducers, they come in two varieties: piezoelectric and piezo-resistive. The main selection criteria of the pressure sensor are based on the geometrical and operational conditions since the last one will affect the sensitivity of the measurements. When subjected to pressure oscillations, certain natural crystals develop an electric potential difference between their sides. The crystal response is linear and proportionate to the measured potential difference and pressure differential. For piezo-electric gauges, it may be converted into a voltage fluctuation or a variation in electric resistance. The tube's incident and reflected shock waves and the various pressure values may be measured by determining the distance and time elapsed between the triggering of two pressure gauges. Using the formula Mi=W/a, the Mach number of a shock wave is calculated. Where W is the incident shock wave velocity, and a is the sound speed in the gas. Flexible pressure transducers are installed at various positions along the shock tube walls, allowing for the production of the (x, t) graph of the fluid domain under consideration [127]–[130].

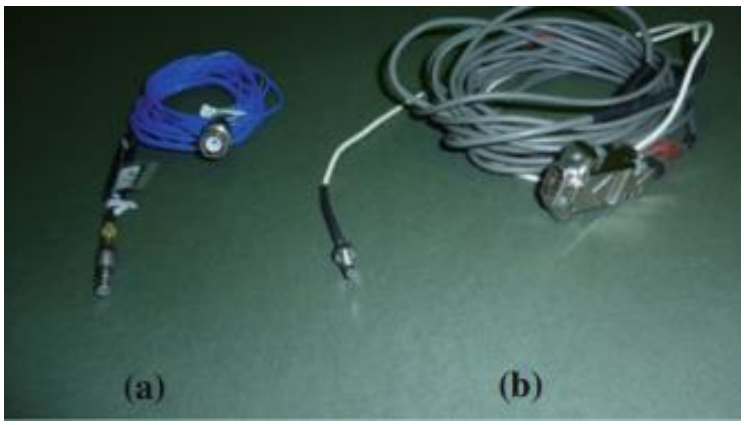

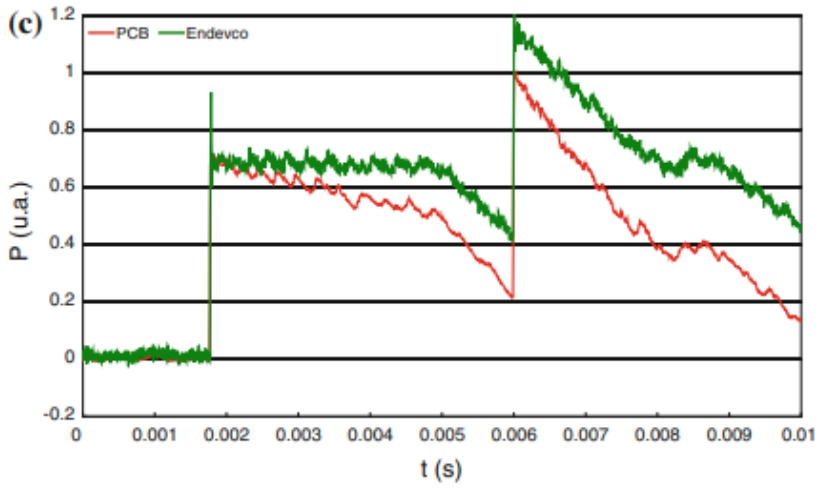

Figure 23. a- PCB piezo-electric, b- transducers, and c- During the same run, they collected signals indicating the proximity of their faces to one another. [130]

PCB transducers (Figure 23) can detect shock or blast wave passes; however, a 0.5 mm layer of silicone covering is required for reliable pressure measurement [131].

3.6.2 Visualization Techniques

Different devices are used to detect the ignition inside the shock tube. For the Shock tube, flow field parameters may be studied using a broad range of spectroscopic approaches, both steady and transient, that can be applied to a wide range of samples and environments. These approaches use the known spectroscopic features of electronic and rovibrational transitions of specific target species and may offer quantitative and non-invasive diagnostic measurement findings. Shock tubes have been used to measure the chemical composition and gas-dynamic parameters using absorption and emission techniques. Recently, Using the external photoelectric effect, photomultiplier tubes (PMTs) in figure (24) are better in reaction time and sensitivity (low- -light-level detection) [132]. Medical devices, analytical

instruments, and industrial measuring systems all use them. It is critical to be aware of the circumstances of the incident light before beginning any measurement. The quartz window in the shock-tube body may be fitted with a photomultiplier tube to detect the ignition delay based on C.H.* emission signals formed during the combustion process at 431.5 nm using a narrow band-pass filter, which is generated during the combustion process.

Figure 24. complete assemblies in protective housings of PMT [111].

CHAPTER 4: TEST RIG DESIGNING, FABRICATION AND CHARACTERIZATION

4.1 Introduction

This chapter of this study will go over all of the stages involved in designing and manufacturing the test rig arrangement chosen to achieve the objectives. The significant elements of the suggested experimental approach and setup are discussed in detail in the first section of the chapter. In addition, several design and manufacturing changes were made to the chosen design before it reached its final form, which is detailed in further depth in the concluding portion of this chapter.

4.2 Method for Experimentation

The literature study stated that the shock tube would be a suitable method for this study's experiments. Under various beginning temperatures and equivalency ratios, a specifically developed state-of-the-art spherical bomb test rig will be used to determine the laminar and turbulent flame speed of liquid fuels. As seen in Figure 25, an experimental design plan was created by analyzing past designs and incorporating the essential aspects of those designs into this dissertation.

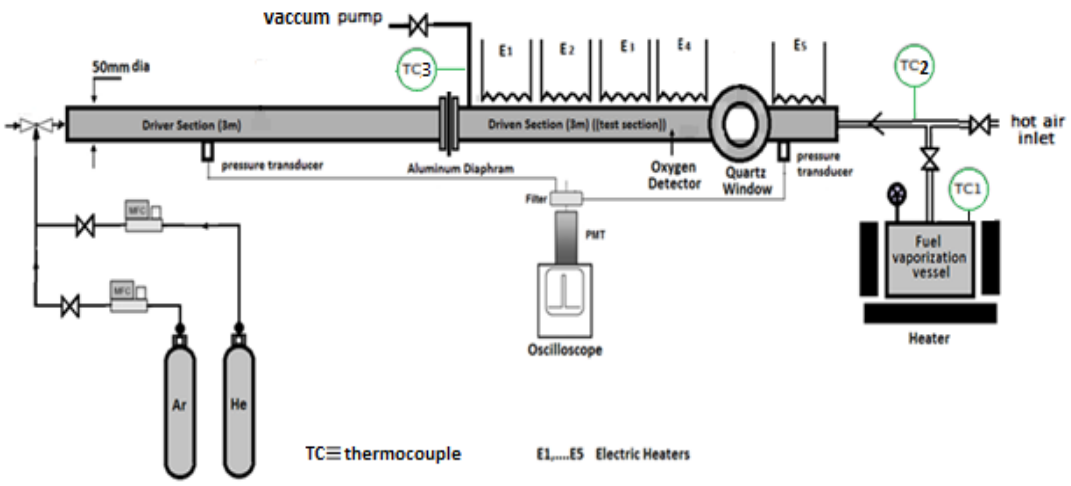

Figure 25. schematic view of the shock tube experimental setup using the evaporated heated pot

The measurements will be conducted in a standard shock tube as explained in the introduction of this proposal; the test rig design can be described as follow: It consists of a long tube with 6 m length, which is supposed to be 120 times [99] the tube diameter (50 mm) this due to avoiding catching up of the reflected rarefaction wave with the incident shock wave before the incident shock is generated inside the tube. The given shock tube is divided into two parts: driver section (3m) and driven section or test section (3m), Figure 7. A thin aluminium diaphragm separates the two sections. The driver section is supplied with helium as the main driver gas, and Argon is added to match the acoustic impedance of the shock heated driven gas. The two gases are pumped to the driver section using two high-pressure mass-flow controllers. The flow of helium and Argon are controlled by mass flow controllers (MFC). The driven section will be fitted with an Oxygen detector to measure the mixture O_2 content ratio. The driven section (test section) is provided with a quartz window towards the end of the tube. The driven section was also heated using nine standard electric heaters [133] and 90 cm in length for the one heater. A total capacity of 90 W per heater is applied to maintain the test section at a temperature ranging from 150°C to 250°C in order for liquid fuel to evaporate. Each segment of the driven test section is heated by mounting three heaters around its surface area distributed by 120 ° apart. Figure (26) shows the arrangement of the heater around the tube.

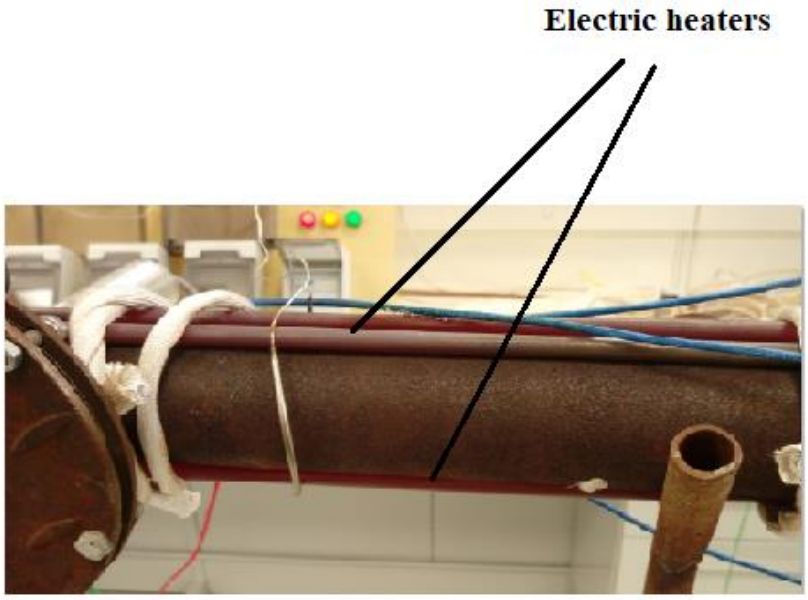

Figure 26. Electric heaters around the tube

Several exposed locations were covered with fibreglass insulation (see Figure (27)). The insulation properties can be found in Appendix E. In addition, there was a temperature controller for each heated jacket. Finally, a heating tape was put around the manifold that connects the mixing tank to the shock tube to prevent condensation during the filling operation.

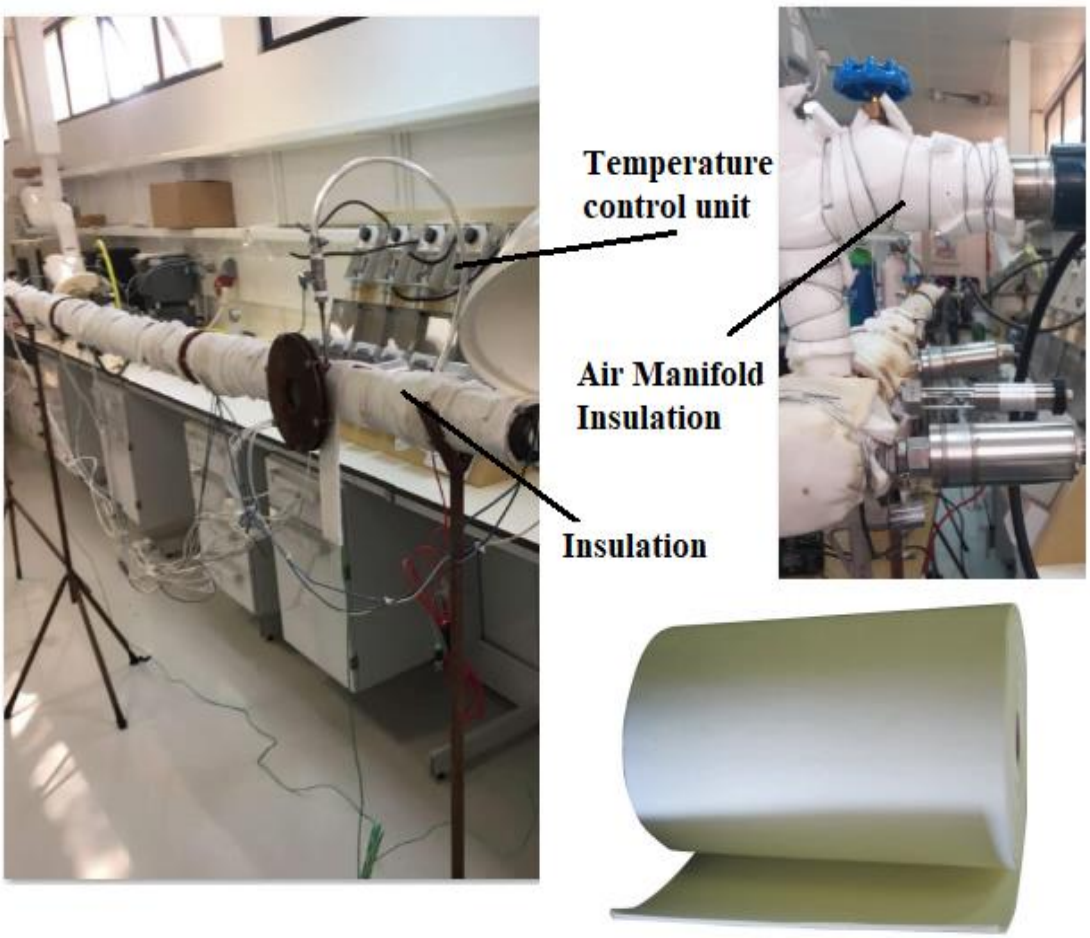

Figure 27. Insulation of the test section and air inlet connection

There are two ways of loading the fuel inside the driven section. The first method (see Figure (25)) uses the direct evaporated fuel prepared by heating fuel inside an insulated pot surrounded by an electric heater and a heater below the pot to convert the fuel phase to vapour. However, the main challenge of this method is the occurrence of fuel condensation in the connections before the inlet to the tube. The second technique (see Figure (28)) is to inject the fuel droplets directly into the shock tube in two ways: either to use the fuel injector and which requires high pumping pressure of the fuel, or to use the injector gun that uses the compressed air to suck the fuel and deliver it to the tube in automized spray fuel with more homogenously

mixture with air. The first injection method is challenging to apply due to the poor mixing with air, and the mixture will be difficult to ignite. The other injection is the method utilized for fuel injection;. However, the compressed air lowers the fuel temperature of the mixture, the heating inside the driven section will maintain the temperature at the required value. The electric heaters of the test section will be switched on for about 45 minutes prior to the experiment to ensure the evaporation of the tested fuels fully and set the required initial temperature of the experiment. Fabrication of the shock tube will be made from steel. Different sealing materials will be used to ensure no leakage from the two sections of the shock tube. An external electric heater will control the inside temperature of the test section. The test section of the shock tube will be covered with fibreglass insulation (made from a ceramic fibre that withstands till 1260 °C) to avert any probability of fuel vapour condensation inside the shock tube. Insulation must also be placed in all fuel lines to avoid condensation of the vaporized fuel. Air is delivered to the shock tube using a heat gun since it can efficiently control the airflow rates and air temperature. The test section is fitted with a quartz window capable of withstanding the high temperature and pressure of the shock waves. Independent temperature measurements inside both sections of the shock tube will be carried out using a type k thermocouple connected to a data acquisition system (DAQ).

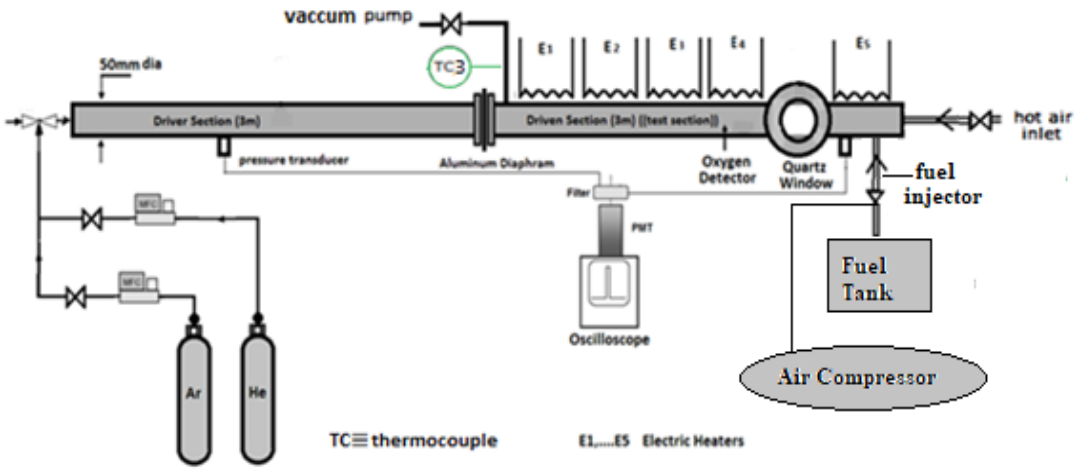

Figure 28. schematic view of the shock tube experimental setup using the fuel injection method

4.3 Measurement Devices

This section contains the components and characteristics of all of the measurement devices and an explanation of the methods used to place them on the shock tube.

4.3.1 Pressure Measurement

The pressure transducer is a device used to monitor the pressure inside the shock tube, as mentioned in Chapter 3, section 3.6.1. It converts the pressure into an electrical signal, and then it is essential to convert this electrical signal to a physical property which is pressure, for our purpose. In this study, five pressure transducers were used to detect the pressure across the tube. They were distributed four in the driven section and one in the driver section. Their location is explained in Figure (29), and the first sensor is located 2 cm apart from the endwall of the driven section for detecting the onset of ignition when it has occurred. The four pressure transducers in the test section have recorded the pressure amplitude in which the incident shock

velocity slope across the driven section will be determined and thus the Mach number.

In the first two positions from the endwall, the mounted pressure sensors are PCB Piezotronics (PXM01MD0) [134], which have a pressure measurement range of 0 to 25 bars and an operating temperature range of 0 to 120°C. The required power source is 28 DCV. Their features a pressure output response of 10pC/psi, which is converted to a voltage measurement by employing an inline PCB Pierzotronics charge converter on the circuit board (Model 422E35)

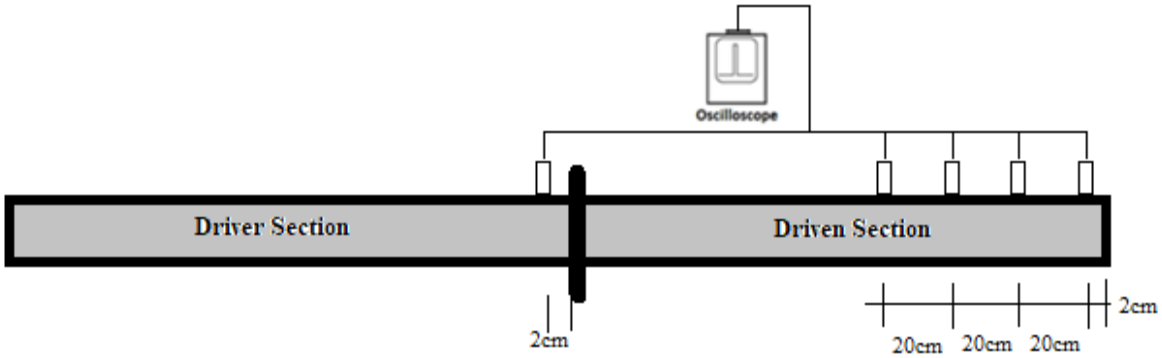

Figure 29. schematic view of the five pressure transducers distribution across the shock tube

A calibration unit in the hydraulic machine laboratory in Qatar University (Beamex Multifunction Calibration unit Figure (30-C)) was used to finish the calibration process before using the transducers in our experiments under power excitation of 28 DCV. The pressure transducer was connected to the testing machine and delivered specific pressures as a calibration procedure. It was necessary to record the output signal and then compare it to the calibration charts that came with the sensors. In the end, it was determined that both pressure sensors were functioning correctly and providing accurate data. Furthermore, the result as is shown in figure (27):

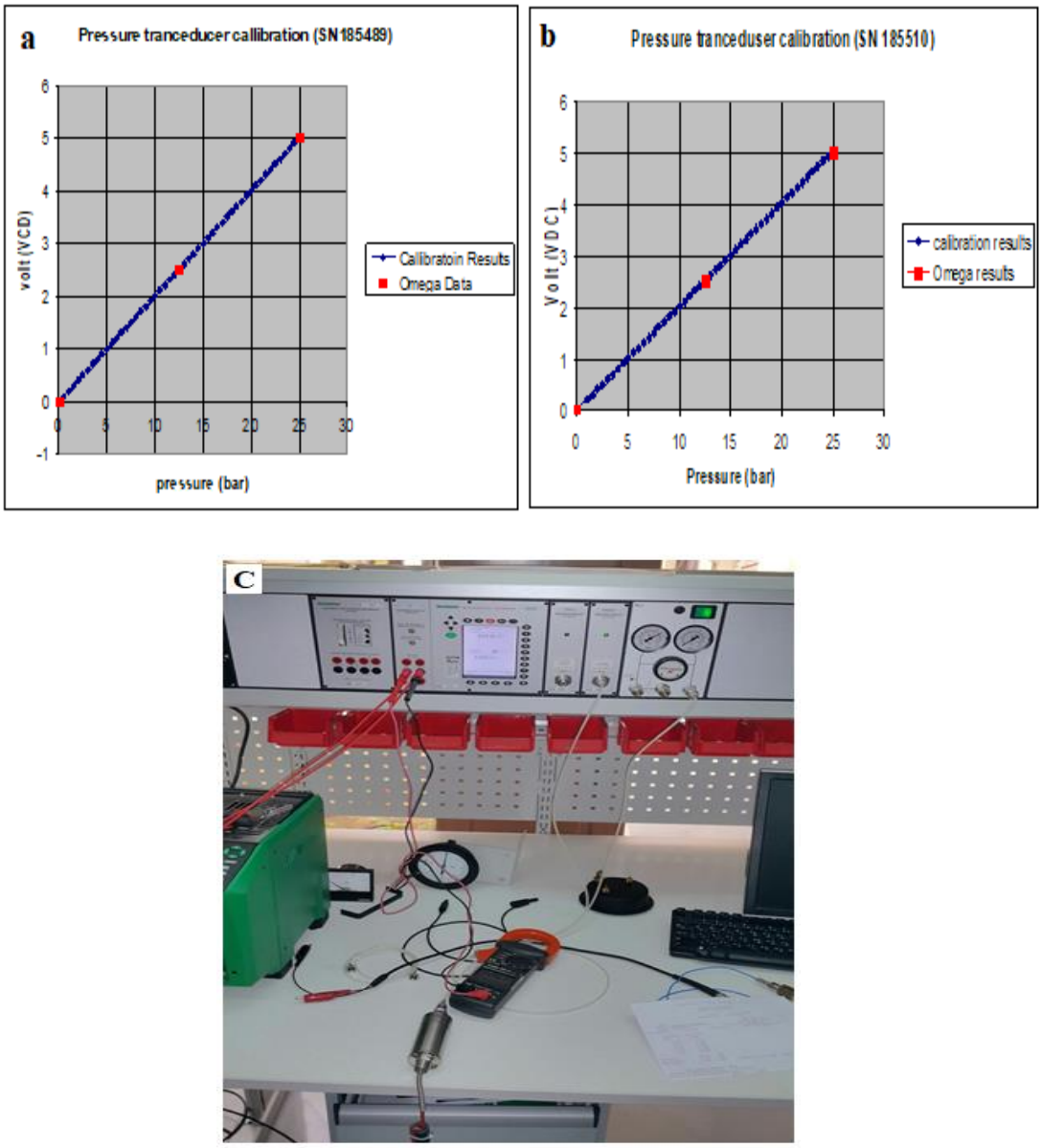

Figure 30. Substantial convergence between the datasheet and the actual data obtained from the calibration unit (Beamex Multifunction). (a) Driver section transducer (SN 185489). (b) Driven section transducer (SN 185510) (c) Pressure sensor calibration unit in Qatar University.

The piezoresistive high temperature and pressure transmitter, called 35XHTC [135], is the other three pressure transducers used in the experiments on velocity measurements; therefore, it is suitable for working in places like this one. Pressure

from the flush diaphragm moves through an oil-filled capillary to the silicon measurement cell, where it can be readout. A schematic representation of the 35XHTC pressure transducer is shown in Figure 31.

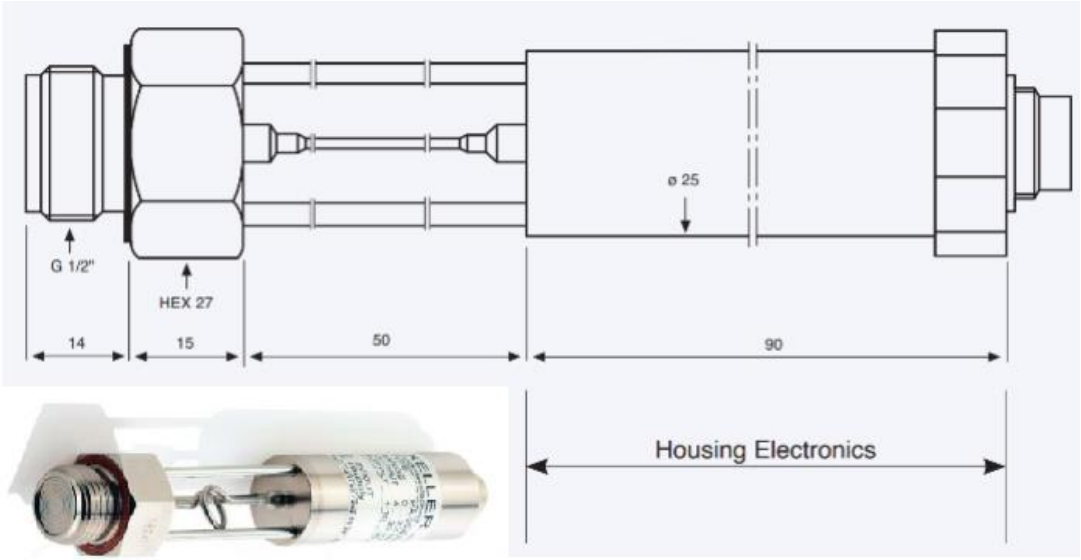

Figure 31. a schematic and graphic picture of the (model 35XHTC) pressure transducer

A local Qatari company has calibrated the pressure transducer to create the pressure-current calibration charts. Appendix B includes a calibration certificate from the company that includes these charts. The sensor had to be calibrated first, and then a suitable location on the Shock tube side wall was identified. The desirable location to put the sensor as in Figure 27. By cutting a hole through its body and installing a special adapter fitting created at Qatar University mechanical workshop, G1/2 internal threads were marked, as illustrated in Figure 32.

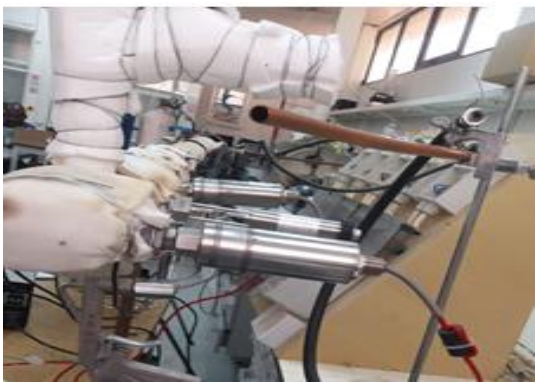

Figure 32. Side view of the mounting of the pressure transducer on the tube

4.3.2 (DAQ) GW-Instek Oscilloscope

The GW-Instek oscilloscope (Model GDS-3152) has been chosen as part of this dissertation. It includes a 150 MHz sampling rate and can record screenshots of waveforms and sampling data in Excel spreadsheet CSV format. Using a Photomultiplier tube (PMT) and two pressure transducers, 25000 sample points are available for each test condition (Section 4.4). However, due to the need to read other transducers, the GW-Instek can only register the readings of two transducers; a Tektronix Digital Oscilloscope (Model TDS3032B) [136] is used with other two pressure sensors. Both oscilloscopes are shown in Figure 33.

(a) (b)

Figure 33. Oscilloscopes used in experiments, a- GW-Instek oscilloscope (Model GDS-3152) b- Tektronix Digital Oscilloscope (Model TDS3032B)

4.3.3 Temperature Measurement

Five different k-type thermocouples [137] (Figure (34)) were used in this study to measure the temperature across the test section and to check the temperature's uniformity through the 3 m length of the driven section. In addition, one thermocouple is mounted on the outlet pipe of the driven section to the vacuum pump to have an accurate reading of the temperature of the air-fuel mixture, to avoid the shield radiation [138] issues due to the small volume of the tube, which affects the reading of the thermocouple inside the tube. The other four thermocouples are fixed on the tubular sidewall to check the uniformity of the temperature across the whole length of the test heated section.

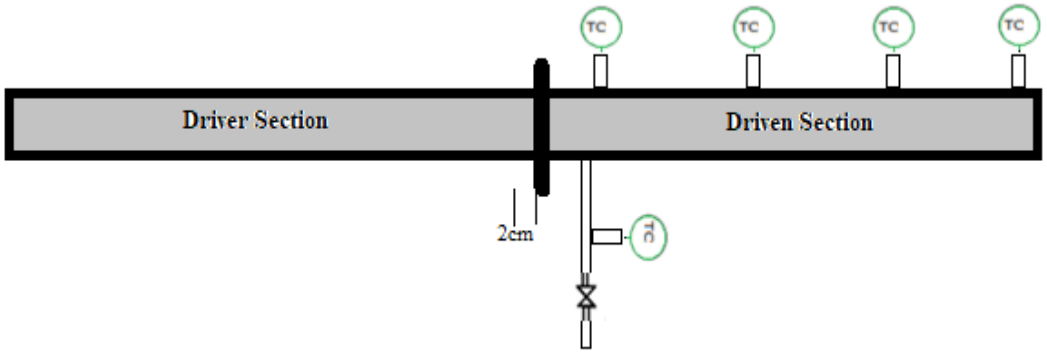

Figure 34. Photo of thermocouple used in this study and schema showing thermocouple distribution across the test section

The characteristics of the k-type thermocouple were found to be suitable for use in this dissertation [137] (see appendix C).

A series of temperature calibration tests were carried out to ensure that the driven area was kept at a constant temperature. The test section length of 300 cm is shown in Figure (35).

Temperature uniformity within ±5°C maximum of the fixed points of 100, 150, and 200 °C was attained. A more significant temperature decrease is approaching the diaphragm section, as seen by these uniformity distributions over the driven segment.

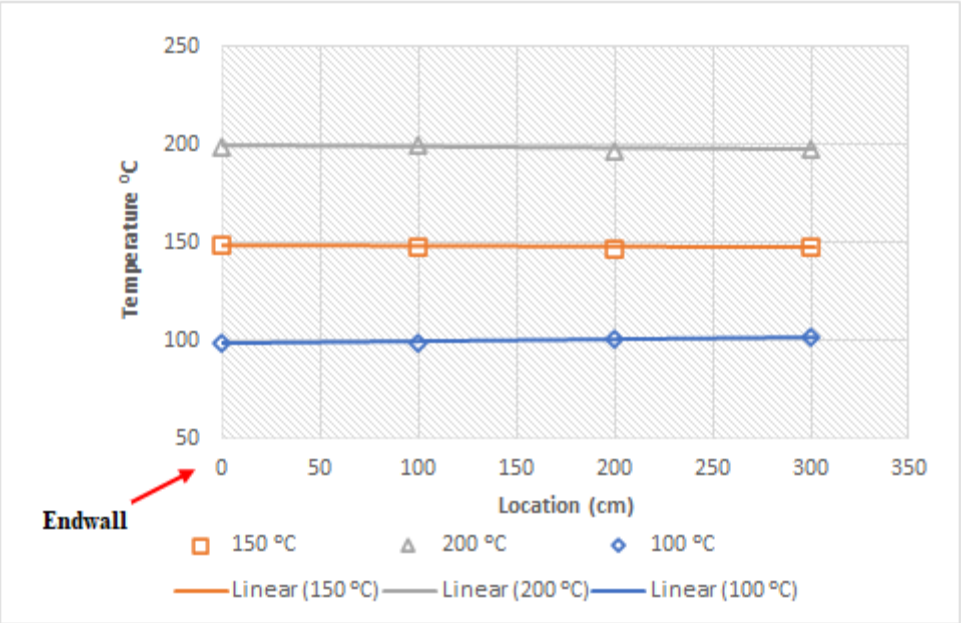

Figure 35. Several Temperatures readings on different locations along the test section.

Another calibration for the temperature readings is to know the time required to reach a set point temperature for the four thermocouples mounted in the driven section. Again, all sensors show acceptable agreement in temperature within time, as seen from Figure (33). Finally, it is crucial to mention that the heating system's maximum temperature was 246 °C as per Figure (34).

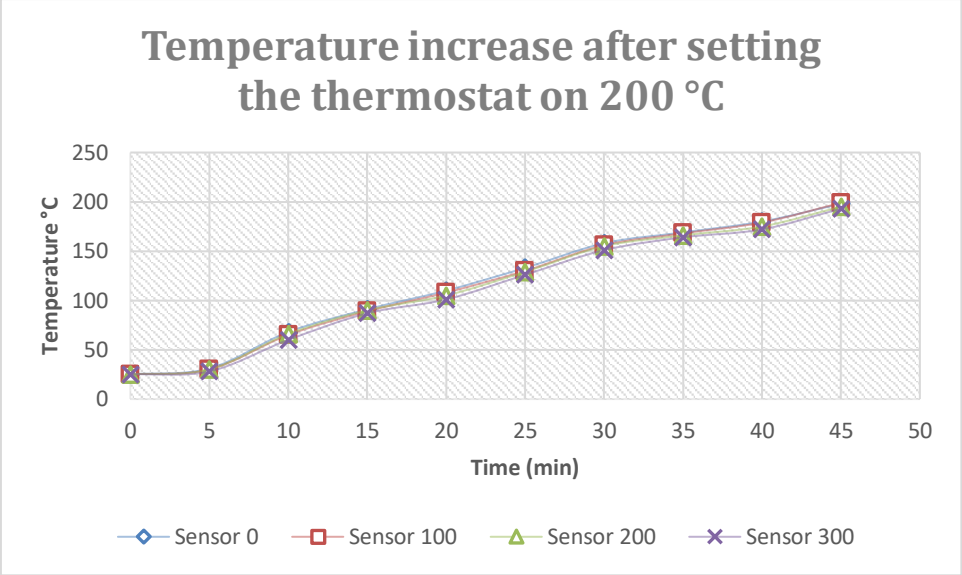

Figure 36. The time required for the four thermocouples to read the set 200 °C

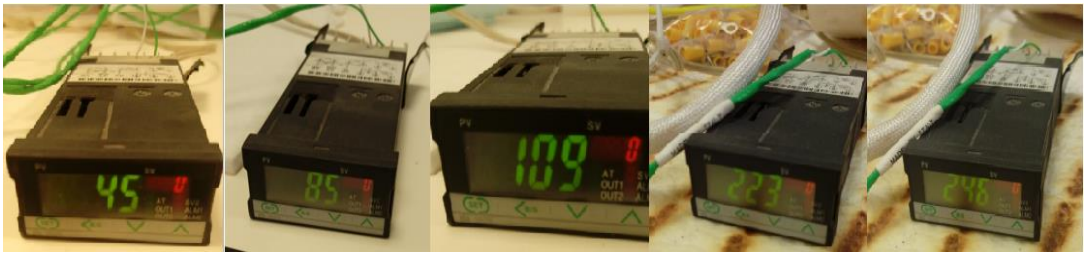

Figure 37. Photos show the temperature increase as the heating for the tube increases.

4.3.4 Driver Section Rupture Test

An inert gas combination of argon, helium, and nitrogen is charged in the driver section to produce a shock wave that passes from the driver section to the driven or test section. Then this shock initiates the ignition of the fuel-air mixture. The description of the experiment in sectionn4.2 states that an aluminium sheet (based on ASTM E252-06(2013) standard test method)[139] is sandwiched between the two portions; when subjected to the high pressure created in the driver section, the aluminium sheet ruptures, causing an ignition to occur as a result of the shock wave

receiving the endwall of the driven section. The aluminium foil is 0.3mm thick and had been cut to have the diaphragm shape, and it is necessary to consider the flatness of the layers when it is doubled in case of using more than one layer.

The need of finding precisely the pressures used in the experiment to estimate the number of aluminium layers required at this pressure. Figure (38) shows the pressure transducer in the driver portion after the aluminium foil was ruptured, illustrating how the pressure dropped.

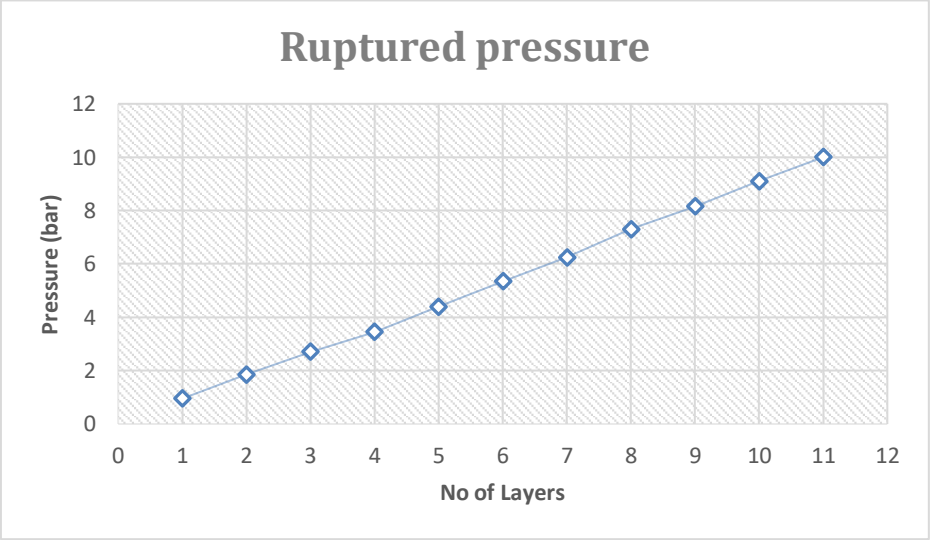

Figure 38. calibration of the shock wave initial pressure based on the number of aluminium sheets that separates driven and driver sections

Figure (39-a) illustrates the increase in the pressure of the driver section as a snapshot from the DAQ, and Figure (36-b) explains the rupture moment and how the pressure decreases suddenly across the diaphragm. The pressure signal is recorded using the fifth thermocouple mounted 2 cm apart from the diaphragm.

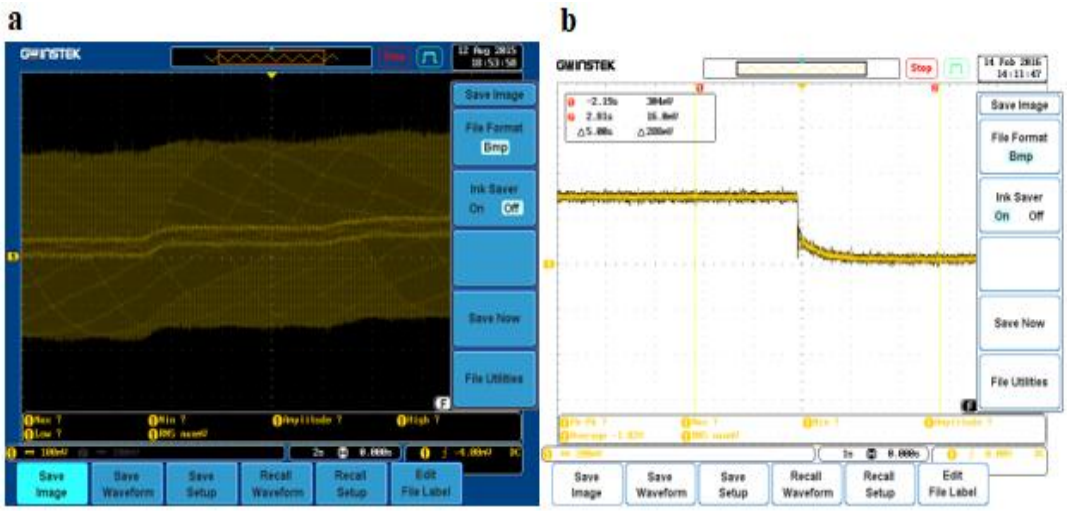

Figure 39. (a) Oscilloscope shows that the increasing pressure charges the inert gas mixture. (b) Display of the moment when the aluminium diaphragm had collapsed.

The display of the diaphragm before and after the rupture is explained in figure (40), in which obviously how a set of aluminum layers are fixed in the flange explicitly designed for the diaphragm.

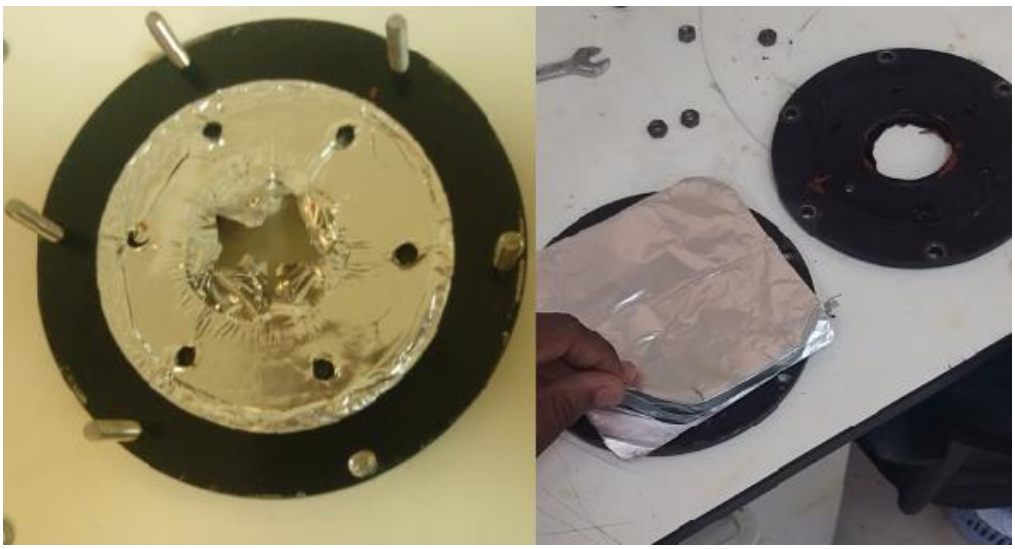

Figure 40. The diaphragm before and after the rupture

4.3.5 Shock Tube leaking Test

The leakage test was done for both driver and driven sections. This is because mainly the tube consists of six main segments connected by flange and screw-nut connections and the possibility of leaking from ports of pressure transducers, thermocouples, and O_2 detectors. Furthermore, the leakage test for the driver section was performed under cold conditions since no heating in this segment used the three driver gases used in tailoring the experiment (He, Ar, and N_2). Therefore, the process starts by filling the driver section with the specified gas, then monitoring the pressure using a standard pressure gauge (Bourdon gauge) (see figure (42)) and seeing how it decreases with time. Finally, all gases were compressed into the tube till they reached 20 bar. The system is withstanding for all gases in the first 30 minutes. This time is sufficient to finish the transient experiment, as shown in Figure (41).

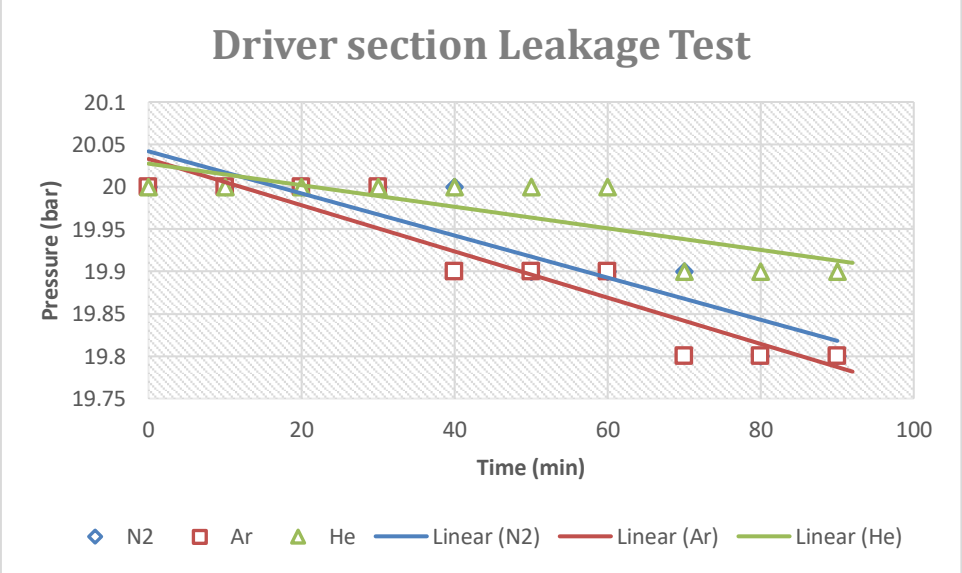

Figure 41. Cold leak test in the driver section for all gases used in the experiments

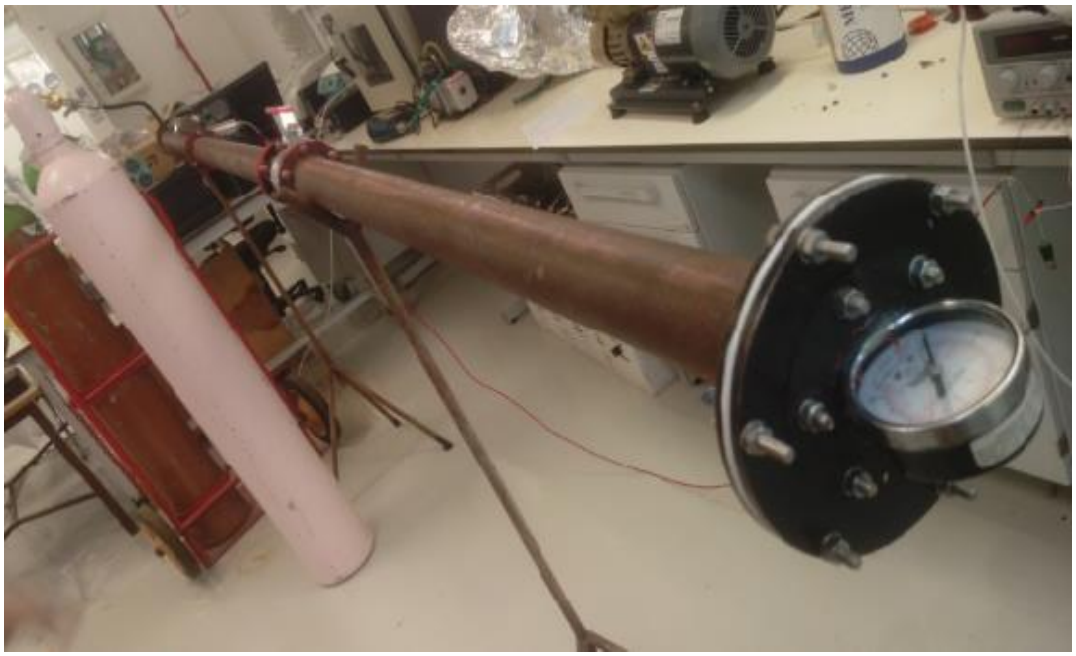

Figure 42. The leakage test for the driver test

The leak test for the driven section was conducted for both cold and hot conditions since this area of the shock tube has many ports and the influence of heating in the silicon used between the segments. Therefore, the air was used to be increased its temperature to test the leaking for different sets (100, 150, and 200 °C). The ideal gas equation of state is used to compute the number of air miles, and the pressure sensor is used to evaluate the pressure at each corresponding temperature:

$$PV = nR_uT \qquad (9)$$

Where P [kPa] is the pressure inside the driven section, V [m^3] is the total volume of the test section, which is 5.9×10^{-3} m^3, R_u is the universal gas constant (8.3144 KJ/kg K), T is Temperature [K] n is the number of air moles which is supposed to be equal

to any value of P, and T. Table 9 summarizes the results of the hot leak test.

Based on the safety considerations and the computed dynamic and thermal stresses created within the tube, the maximum pressure that this shock tube may achieve before rupture is 20 bar.

Table 9. Hot leakage experiment

Reading	**1**	**2**	**3**
Temperature [K]	373	423	473
Pressure [Kpa]	101.377	114.967	128.556
Air Moles [mole]	1.93×10^{-4}	1.9286×10^{-4}	1.929×10^{-4}

4.3.6 Equivalence Ratio (Φ) Control

Air-fuel mixtures may be described using the equivalency ratio (**Φ**), which indicates whether they are rich (**Φ** >1), stoichiometric (**Φ** =1), or lean. Therefore, variations in the equivalency ratio must be examined for their impact on ID times in this dissertation. As a consequence, the experiment's equivalency ratio must be established. The gas detector apparatus is often used in safety applications to detect the presence of hazardous gas in a place by measuring the quantity or percentage volume of the gas present. In addition, it can emit an alert sound in the event of a leak or when the quantity of dangerous gas is released beyond a specified threshold. Such applications may be found in various places, including oil refining and stations, boiler rooms, the petrochemical industry, mining, and others.

As part of this research, an OC-F08 fixed gas detector installed on the wall is used to sense the percentage volume of oxygen in the shock tube heated section (0-30.0

per cent O_2 volume) before the ignition process in order to estimate the equivalency ratio for each test scenario under consideration.

The OC-F08 gas detector has been adequately calibrated before being used in studies, and the calibration certificate can be found in Appendix B. The calibration certificate can be found in Appendix B. The OC-F08 gas detector, installed on the wall and utilized in this dissertation, is shown in Figure (43).

Figure 43. Explanation of different sets of O_2 readings

This particular type of gas detectors was chosen for use in this dissertation due to the nature of the equivalence ratio determination since the available gas analyzer in Qatar University in Heat Engine Lab its operation principle is based on induction of a sample of the air-fuel mixture to the device and then analyze it; however, this is only suitable with the dry gaseous sample, and the mixture sucked from the test section has a vaporized fuel that can be easily condensed before reaching the device. So, the need after that for a device that can detect the oxygen ratio without withdrawing a mixture sample. In addition to the mentioned justification of using the gas detector, there are several, which are as follows:

- Stable signal, strong repeatability, rapid reaction, and high accuracy are all desirable characteristics.
- An LED screen that shows the gas type and concentration and the unit and instrument status, among other things.
- A protection mechanism and an alert are provided to avoid excessive gas concentration leakage or assault. The gas concentration is shown in % vol, parts per million (ppm), % LEL, or milligrams per cubic meter (m^3/hr).
- Operation of the remote control through infrared
- A data logger and a data restoration feature are included.
- Suitable for use in combustion-related applications.
- Resolution of 0.1 % LEL, the accuracy of 3 % F. S., and repeatability of 1 % are all achieved with this instrument.
- The reaction time is less than 20 seconds, and the sensor detects oxygen concertation in the desired range (19.5 % to 20.2 %)
- It may also detect various other gases (such as CH4, C3H8, H2, NH3, and CO2).

The tested fuels' equivalency ratios are calculated by implementing the below-mentioned processes. Initially, the Calculation of the stoichiometric equivalence ratio $(A/F)_s$ from the complete chemical combustion reaction for one mole of diesel fuel:

$$C_{16}H_{34} + 24.5\,(O_2 + 3.76N_2) \rightarrow 16CO_2 + 17H_2O + 92.12N_2 \qquad (11)$$

$$\Phi = \frac{\left(\frac{A}{F}\right)_s}{\left(\frac{A}{F}\right)_a} \qquad (12)$$

$$\left(\frac{A}{F}\right)_a = \frac{Actual\ mass\ of\ air}{Actual\ mass\ of\ Fuel} \qquad (13)$$

In the above equations, the actual mass of fuel can be determined and injected

inside the tube for the required value of the equivalence ratio. The below curve correlation (Figure (44)) is developed to determine the relationship between the O_2 reading and the equivalence ratio.

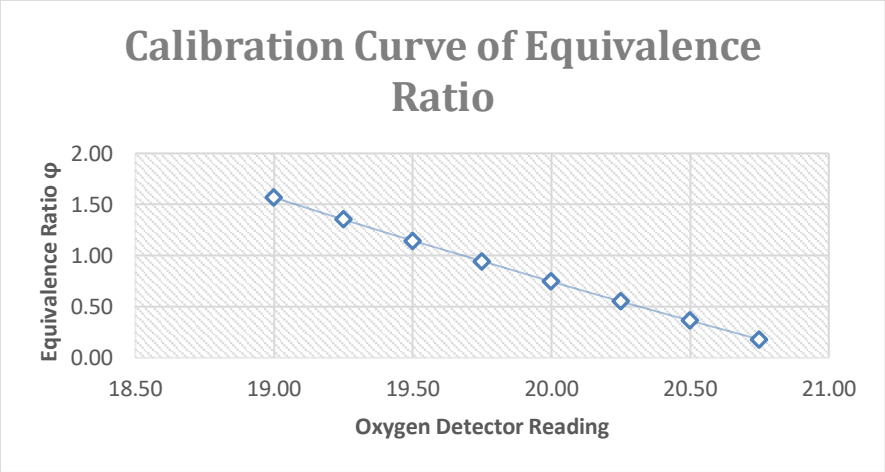

Figure 44. Calibration curve of the equivalence ratio based on the Oxygen detector reading

4.4 Tested Fuel Blends

This study will test the following fuels: conventional diesel, GTL, and a 50/50 mix of conventional diesel and GTL (see Figure (45)). The chemical and physical parameters of the examined fuels are listed in Table 2.3. However, properties in detail are shown in the following Table 10. In a 50:50 volumetric ratio, diesel fuel and GTL are blended. The preparation method for the fuel blend ad the mix physical and chemical properties are explained by Sadig et al. [30]

Table 10. properties of experiment fuels

Parameter	**GTL**	**Diesel**	**Blend [D50:G50]**
Known Formula	$C_{16}H_{34}$	$C_{16}H_{34}$	$C_{16}H_{34}$
Density [kg/m^3]	770	830	792

Cetane No	77	55	64
Average Boiling Temp [°C]	260	275	263
Flash Point [°C]	77	55	71
H/C	2.125	2.125	2.125
HHV [MJ/kg]	49.3	42.9	46.2

Figure 45. A photo of the fuel tested in the Shock Tube

4.5 Compressor, Air inlet characterization, and Vacuuming of the system

The compressor was used for the second fuel loading method since the injector needs high pressure to suck the Factors fuel droplets into the system. The compressor used as a general-purpose air compressor is already available in the Energy and Environment laboratory at Qatar University, as shown in Figure (46). The compressed air, as mentioned above, sucked the fuel that had been prepared in the fuel tank through a special fuel hose. The air enters the driven tube through the air heater (heat gun), and the reason for choosing is its capability of controlling the air temperature and flow rates. The air temperatures can reach 660 °C. This hot air will decrease the time needed for heating the test section since the air temperature inside

the tube can reach 100 °C for a moderate temperature range from the air heater.

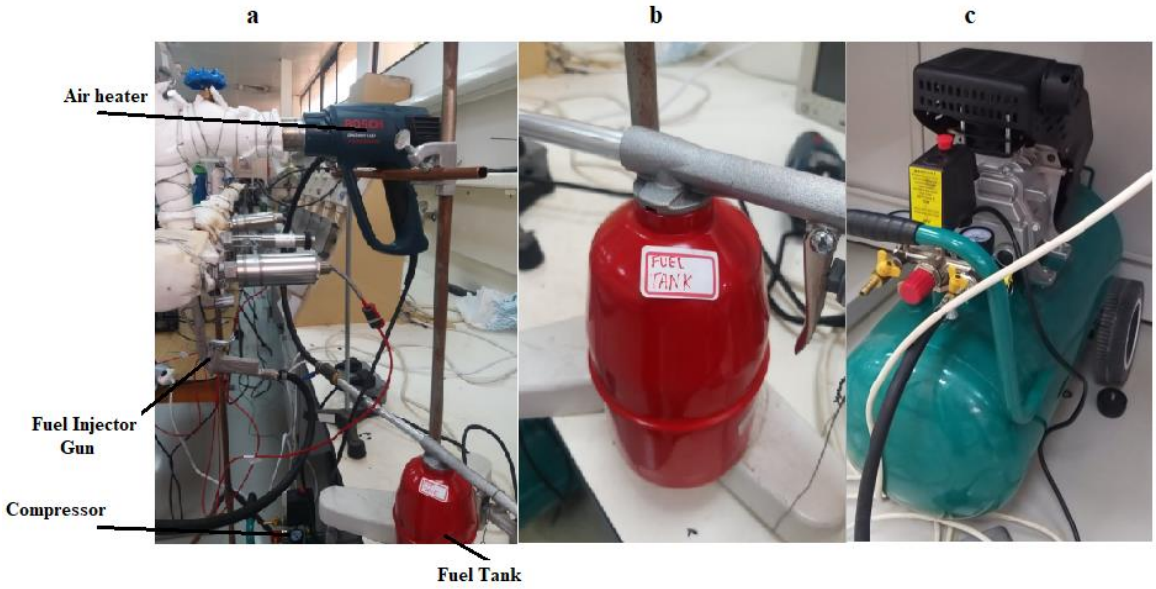

Figure 46. a- The air inlet system to the shock tube involving the compressor, fuel tank, air heater, and fuel injector b- Fuel tank c- Air compressor.

4.6 Final Experimental Procedure for Ignition Delay Measurement

The following steps are the procedures followed for the test rig operation and then measuring the ignition delay for the required fuel.

- Initially, the system was cleaned, and the air was compressed inside the driven tube to remove any deposits from the previous experiments. These deposits can be residues of fuel or waste of the aluminium diaphragm after the rupture process.
- The tested fuel was prepared in the fuel tank and checked all the connections between the tank, compressor, and air heater.
- The exhaust fans are turned on to evacuate any vaporized smoke from the sealant, saturated insulation, and fuel vapour.

- The diaphragm was prepared by gathering the required number of layers based on the required pressure in the driver section and checking the sealing of the diaphragm, then waiting for 20 minutes till the sealant was strengthened.
- The diaphragm was remounted on its location between the two sections and reconnected all the flanges of the tube.
- The electric heaters around the driven section were turned on for at least 45 minutes and observed the temperature increase across the tube every 5 minutes until they reached the required condition.
- The air was fed inside the tube using the air heater at low pressure, and the air temperature was monitored till the required level.
- The driver gas was released inside the driver part with the required mixing ratio or relentless pressure of the driver section.
- The DAQ in Figure (47) was prepared with the suitable setting of capturing the signal of the pressure transducer.

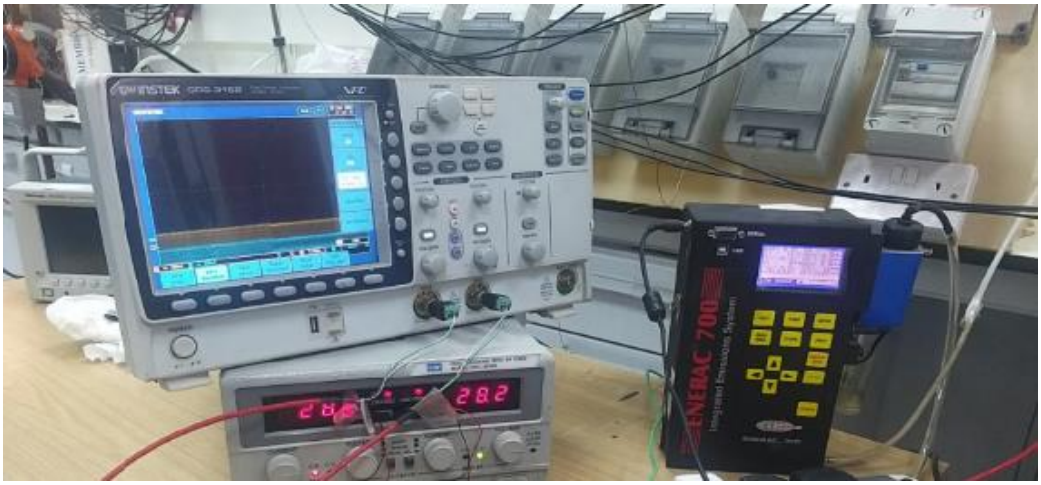

Figure 47. The DAQ was ready to capture the signal.

- Carefully, the fuel was induced inside the driven section by pressing the injector for one time, and the O2 detector reading was noticed and waited till it reached the required value.
- The rupture was initiated using the control valve in the driver section and simultaneously snapped the pressure wave at the rupture time.
- The vacuum pump exhausted the ignited gases and emissions outside the tube. They then waited for the system until cooled by convection to remove the aluminium waste parts after the rupture to start a new trial.

CHAPTER 5: RESULTS AND DISCUSSION

5.1 Introduction

This chapter presents the experimental results that have been obtained from the shock tube tests. Initially, an experimental and numerical investigation of the effects of the diaphragm pressure ratio and its position on a heated shock tube performance is shown in the following few sections, followed by measuring the incident shock velocity to calculate the Mach number of the determined driver pressure and the presentation of the ignition delay time measurements for conventional diesel, GTL, and diesel-GTL fuel blend.

5.2 Characterization of Shock tube for ID measurement

5.2.1 Incident Shock Velocity Measurement

For the experiment to be successful, it must be able to produce a high-velocity shock wave, as previously mentioned. In order to understand how fast the shock wave travels back to the source, it is necessary to measure how fast the driven tube moves. Viscous processes or a partial rupture of the diaphragm usually result in the incident shock wave's attenuation as it travels down the tube. Therefore, the magnitude of experimental discrepancies hidden beneath the reflected shock wave will be calculated based on the attenuation level.

Different driver gas velocity profiles (Helium, Nitrogen, and Argon) displayed in Figure (48) were obtained at a loading driver pressure of 10 bar throughout the experiment. The driven section is monitored for attenuation at (2.3%2.18% and 1.96%) for each gas, every one meter of distance travelled. This is the most significant distance that may be used to measure the speed of the shock wave, depending on where the sidewall ports are placed on the tube. The shock's velocity

declines linearly during the last one metre of the driven tube due to the different factors of non-idealities such as non-ideal rupture of the diaphragm [140], boundary layer effects, and driver gas contamination. Therefore, the shock tube was used to gather shock-wave attenuation data for Helium, Nitrogen, and Argon across a broad range of pressures, as shown in figure (49).

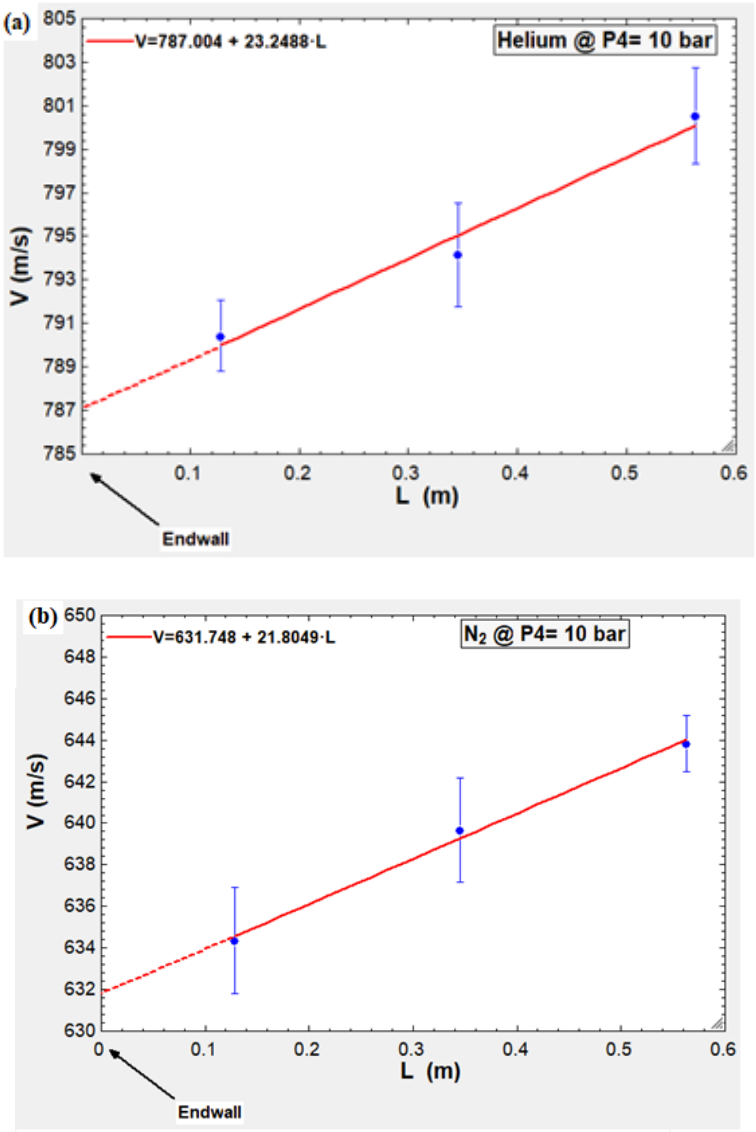

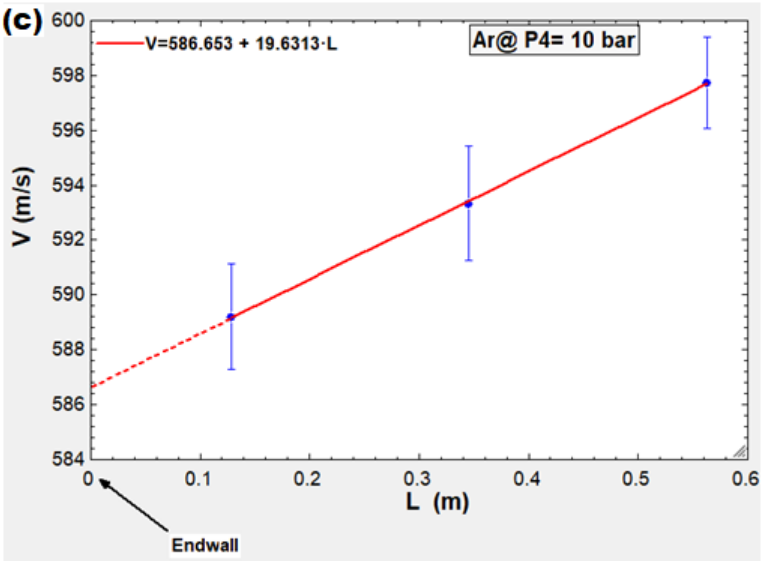

Figure 48 The extrapolation of the incident wave speed at the endwall for approximately the last 60 cm of the driven section. (a) Helium (b) Nitrogen (c) Argon

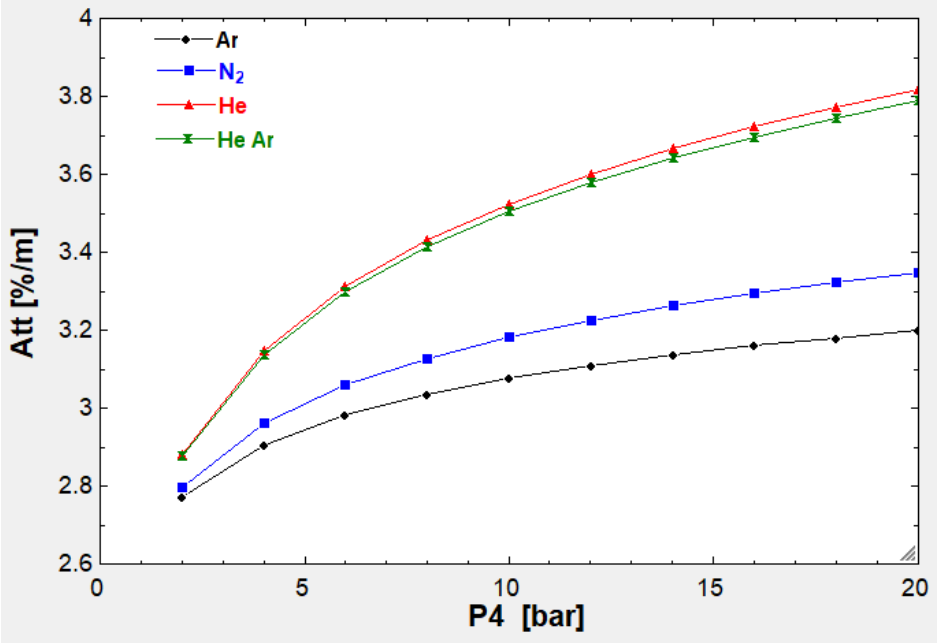

Figure 49 Attenuation of the shock tube for different driver gases pressure at an initial temperature of 200 °C.

The attenuation of the incident shock wave velocity rises in proportion to the

increase in the driver's gas rupture pressure. According to figure (49), Helium has a more considerable attenuation value than other gases. This is because the velocity of the shock wave is measured to be the greatest in Helium, which increases the thickness of the boundary layer over the driven length. Furthermore, the viscosity of Argon reaches its maximum around 200 degrees Celsius, which affects the thickness of the boundary layer as it increases [141]–[143].

The shock tube measurements have several obstacles, including nonideal effects, restricted test time availability, and a lack of agreement on defining measurement errors. For the new shock tube to be evaluated in terms of performance, it must calculate the error percentage of all of the related measurements. The distance and the time it takes for the shock wave to travel between side-wall transducers have a role in shock velocity measurement. Therefore, the accuracy of both of these measurements is critical. The size and location of the transducer holes and the geometry of the driven section are potential causes of inaccuracy for distance measurement.

Furthermore, the electrical equipment used for time measurement (counters, wires, and pressure transducers) has the same characteristics. The theory of uncertainty propagation is used to calculate the overall uncertainty in shock velocity measurements. For a shock travelling at (Mach number between 1.2 to 1.6) between transducers 250 cm apart, this interval corresponds to a standard uncertainty of 0.1% of the measured time. The estimated uncertainty of the distance between the ends of successive pairs of holes in the tube wall is ± 0.15 mm.

5.2.2 Mach Number

The isentropic Mach number is shown in the figure (50), whereas the Mach number based on the measurements that have been made via the shock tube is shown

in the figure (50). The Engineering Equation Solver (EES) package models the isentropic formulas (Appendix F). It demonstrates that the incidence shock wave velocity rises when the charging pressure in the driver section is raised to a higher level. Tests are performed on three distinct kinds of gases (Helium, Argon, and Nitrogen) to determine whether or not the requisite ignition pressure and pressure conditions were present when the ignition occurred. Furthermore, it has been proven that the experimental trend for all three gases fits the isentropic model (Rankine–Hugoniot) predicted and discussed in section (3.2). The use of Helium as a driving gas may also result in the most significant potential Mach number being achieved due to the high velocity, as seen in figure (48-a). However, due to the viscous effects, the divergence between the model and the experimental data widens as the rupture pressure increases, reaching a maximum of 2.3% difference at the highest Mach number and maximum recorded pressure of 18 bar.

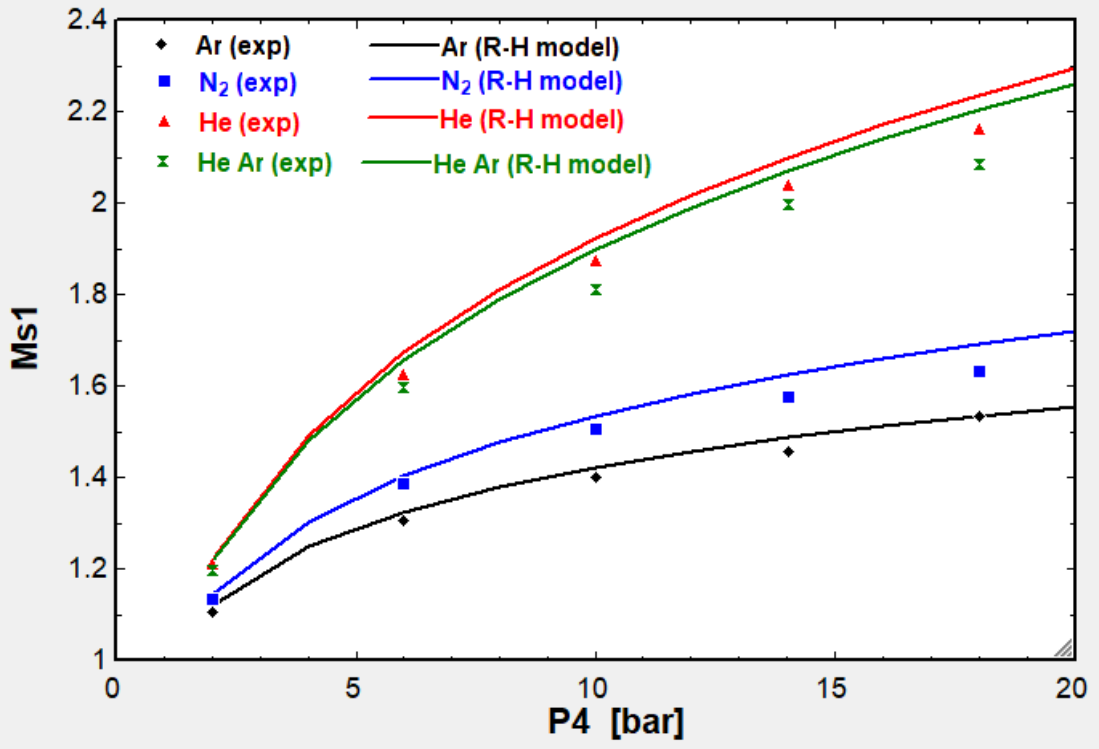

Figure 50 Incident shock Mach number dependency on different driver loading pressures

5.2.3 Test Time

It is essential to record the test time, which represents the time interval between the commencement of the rupture process and the collision of the incident contact surface caused by the incident shock wave and the enlarged contact surface caused by the fan wave that travels through the driver section after the rupture. When the expansion wave, reflected from the end cap of the driver section, reaches the test spot, the test time is over. There are several methods to extend the test time that is discussed by Campbell et al. [144]–[146]he most common technique that has been used is driver gas tailoring, in which the driving gas may be adjusted by blending in a gas with a lower sound speed, such as nitrogen, carbon dioxide, Argon or propane, in order to provide equal pressures on both sides of the contact surface after it has passed through the reflected shock wave. As a result, no wave is reflected again to the testing area since the contact surface has become stationary. For example, in Figure (51), both Nitrogen and Argon have greater test time values than the Helium. However, their capability to reach the required test condition of reflected pressure is less. Thus, a driver gas tailoring technique is necessary, so adding a tiny ratio of either Argon or Nitrogen to the Helium to get an extended test time by 32 % with good achieving of the required conditions (reduce only 5%).

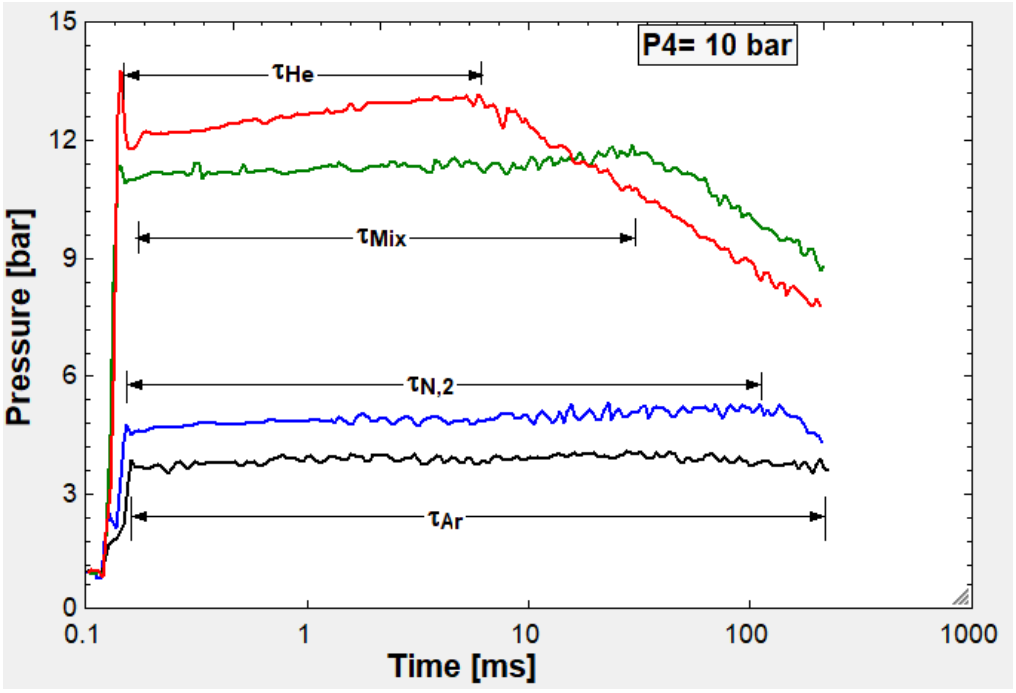

Figure 51 Test time experiment for several tailoring driver gases at a rupture pressure of 10 bar and initial temperature of 200°C.

The effect of the mixing ratio for using Argon as a tailoring gas on the required conditions can be seen in figure (52), which explains experimentally that as the mixing ratio increases by 5%, the Mach number, for example, reduces by 0.6% and reflected pressure 2.51%. The selected mixing ratio in this study was between 5% to 20%.

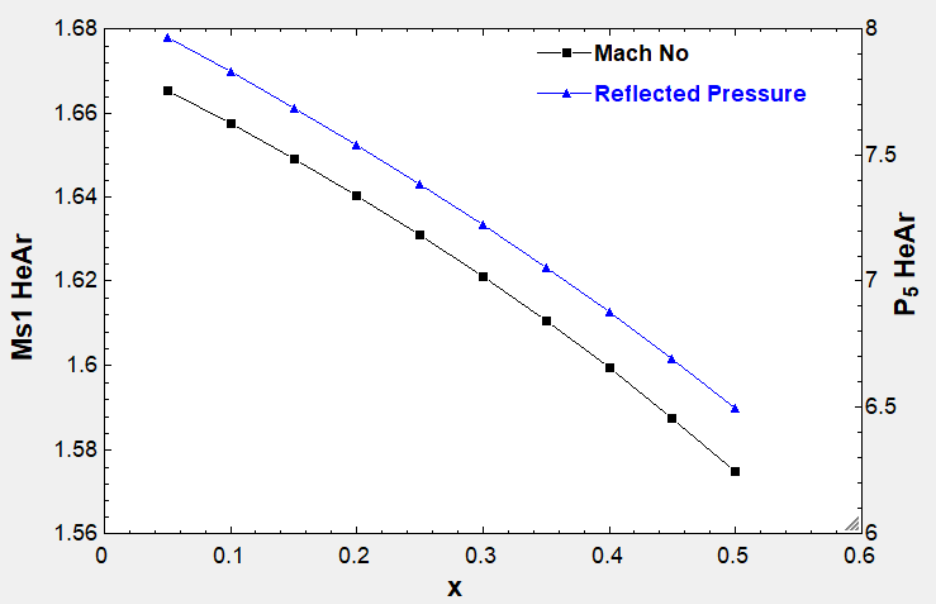

Figure 52 The effect of tailoring gas mixing ratio on the required conditions

5.3 Effect Diaphragm pressure ratio and its position

This topic was published in the journal of Energy Science and Engineering reference [147]. The primary purpose of studying this topic is to investigate numerically and experimentally the performance of the shock tube with different values of the pressure ratios across the diaphragm and the effect of the diaphragm location on the performance and mainly on the obtained Mach numbers. The numerical model simulated the fluid flow inside a shock tube test facility. Five different pressure ratios were implemented during the experiment, and performance evaluation depended on the strength of the incident-shock Mach number.

The inviscid numerical model solver used transient two-dimensional time-accurate Navier-Stokes CFD. In addition, a two-dimensional inviscid density-based time-accurate model was developed to conduct the parametric study. The inviscid model discarded the viscosity effect and reduced the Navier-Stokes equation to the Euler equation. Euler equation can only be seen as the Navier-Stokes equation with zero

viscosity and zero thermal conductivity. The Euler equations used for the understudy numerical model as given as follow:

$$\frac{\partial U}{\partial t}+\frac{\partial E}{\partial x}+\frac{\partial F}{\partial y}=0 \qquad \textbf{(14)}$$

Where U represents the conserved variable of the Euler equation in cartesian coordinates two dimensions. The E and F variables, along with U variable definition, is given below in equation (2)

$$U=\begin{bmatrix}\rho\\ \rho u\\ \rho v\\ \varepsilon\end{bmatrix},\ E=\begin{bmatrix}\rho u\\ \rho u^2+p\\ \rho uv\\ \varepsilon\end{bmatrix},\ F=\begin{bmatrix}\rho v\\ \rho uv\\ \rho v^2+p\\ v(\varepsilon+p)\end{bmatrix} \qquad \textbf{(15)}$$

Since the energy equation was activated in the CFD model, the below equations are included in the numerical model.

$$\varepsilon=\frac{1}{\gamma-1}\left(\frac{P}{\rho}\right)+\frac{1}{2}(u^2+v^2) \qquad \textbf{(16)}$$

Where ε is the specific energy, ρ is the density, u, and v are the velocities per unit mass in the x and y direction, respectively.

The parametric study is including different diaphragm positions and pressure ratios. In order to implement all the boundary conditions for each diaphragm's position, three primary models' geometries should be obtained first in the Design Modeler (Fig. 53).

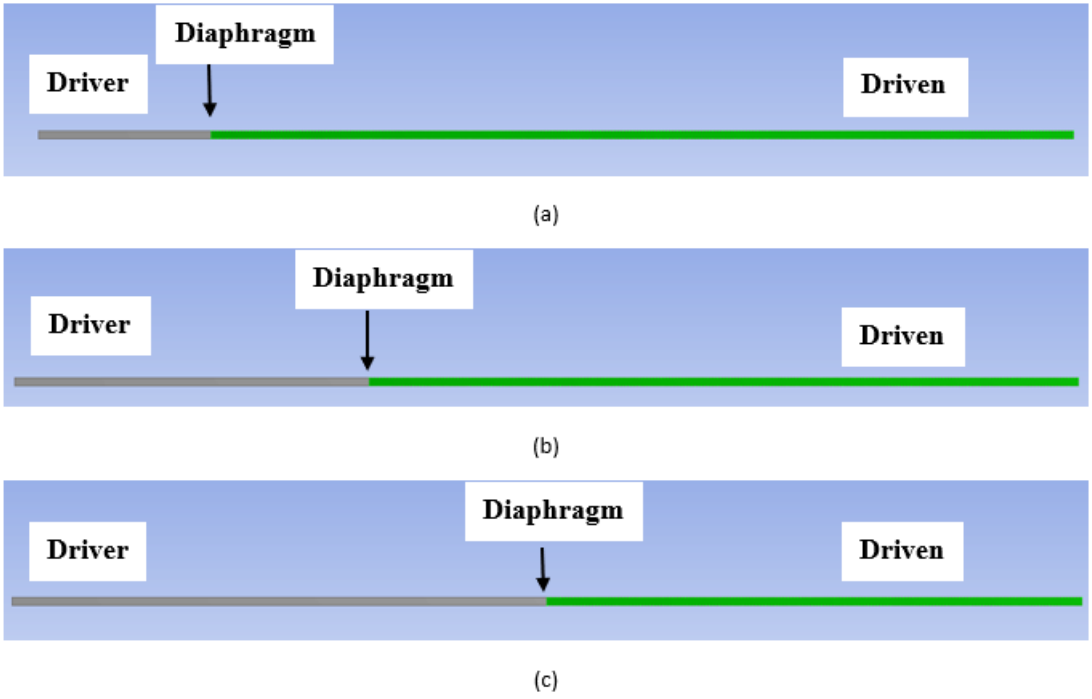

Figure 53 The geometry of the shock tube with different diaphragm locations; (a) Diaphragm at 1m (b) Diaphragm at 2m (c) Diaphragm at 3

Meshing the flow domain was done using the uniform quadrilateral method. The two longitudinal edges of both driver and driven sections were divided; equally, and the division length equalled 1mm. Conducting a mesh dependence study was done by having the pressure distribution at rapture time while increasing the element number. The solution's independence of the mesh element's number was saturated when using 300,000 elements with 306051 nodes. Previous studies only refined the meshing at the diaphragm location to shorten the computational time. In this study, the refinement took place within all the edges of the shock-tube geometry. Although the refinement of the entire geometry increases the computational time, the result's accuracy was sufficiently acceptable. Although mesh dependence study is the most used method in finding the best element size for the model, it is sometimes

considered time-consuming. Orthogonal Quality, Ortho Skew, and Aspect Ratio are the three main parameters located in the fluent mesh statistics, which also indicate the mesh quality. Those values are usually compared with a given acceptable range mentioned in [26] to examine the mesh quality range and time of solution convergence. Table 1 below showed the quality parameters assigned to the study mesh.

Table 11 Mesh quality parameters

Mesh quality indicator	**Value**	**Acceptable range**
Minimum Orthogonal Quality	9.99996e-01	Above 0.01
Maximum Ortho Skew	3.76414e-06	Below 0.95
Maximum Aspect Ratio	2.79720e+00	Below 500

In order to obtain a wave reflection from the shock tube-ends, driver (high pressure) and driven (low pressure) section ends were closed. Solid walls boundary was assigned to the edges of the 2D shock tube, and no fluid penetration occurs. The total length of the shock tube was 6m, and the diaphragm was made by splitting the tube shape with a 2D edge. Diaphragm pressure was set to zero in order to eliminate its added pressure value to the pressure ratio between driven and driver sections. Since no heater was attached to the driver section, the driver section's initial temperature was 300K (T4). In contrast, as the driven section was connected to heater coils, its initial temperature was 423K (T1). All the initial conditions values of the CFD simulation can be shown below in Table 12.

Table 12 Initial Boundary conditions of the numerical study

Working fluid

Boundary conditions	Argon (10%) + Helium (90%)		Air	
	P4 (bar)	T4 (K)	P1 (KPa)	T1 (K)
Case 1	6	300	1	423.15
Case 2	7	300	1	423.15
Case 3	8	300	1	423.15
Case 4	9	300	1	423.15
Case 5	10	300	1	423.15

A density-based explicit solver is used to discretize the governing equation of the flow in time and space. To obtain an accurate and stable solution, the conserved governing equation followed a double-precision and second-order upwind scheme were used as in [148]. For the explicit time-dependent solution, the size of the time step was set to 1e-5 seconds which provide convergence after ten iterations. The solution time interval duration was determined by the time step size (10e-5) and the number of time steps (2000).

The model introduced a parametric study regarding three different diaphragm positions from the driver section endwall (1m, 2m, and 3m) and five pressure ratios (6-10) for each position. In addition to yielding the incident and reflected wave Mach numbers (M_S and M_r), reflected wave temperature was also considered a shock tube performance indicator. The incident Mach numbers (M_S) for the diaphragm middle position from the experiment were compared against those conducted from the model, and good matching was observed. The experiment was conducted for five pressure ratios with one diaphragm position (3m), while the simulation includes all the suggested diaphragm positions for the five diaphragm pressure ratios. The exact working fluids (90% He and 10% Ar) are considered for the experiment and numerical model. The shock-tube performance was obtained depending on the value

of the incident and reflected wave Mach number, and reflected wave temperature. More details about the model can be found in the published article [144]

5.3.1 Experimental Results

As mentioned in the experimental setup (Chapter 4), the velocity of the shock wave is measured by knowing the travel time of the shock wave between the two pressure sensors. Figure (53) illustrates the two sensors' pressure readings versus time. Therefore, the incident velocity could be easily obtained when the time difference between the two pressure peaks is known.

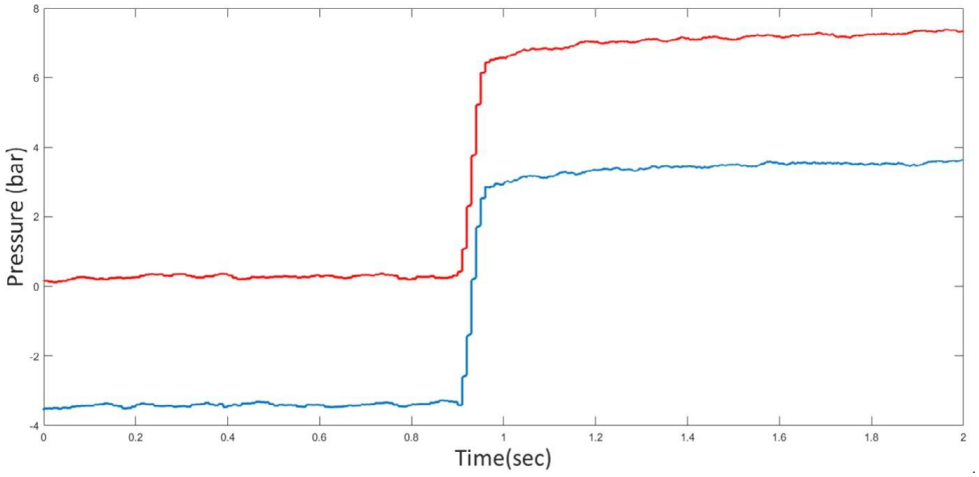

Figure 54. Sample results of the experiment at P_4=8 bar

The experiment was repeated for five pressure ratios, and five shock-wave velocities were obtained. The incident Mach number associated with each wave velocity was obtained, as shown in Figure (54) below.

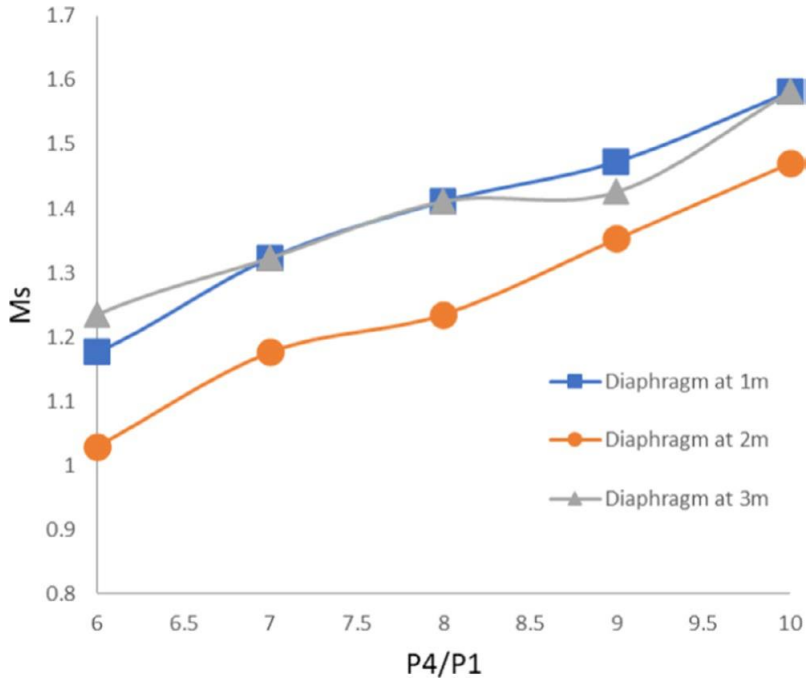

Figure 55. Incident Mach number dependency on diaphragm's location and pressure ratio

5.3.2 Numerical Results

When the diaphragm rapture at t=0, the driver and driven pressure change from their initial value, the driver region pressure will start to decrease in response to expansion wave formation. In contrast, the driven section pressure will increase due to the developed compression wave propagation and diffusion. Eventually, the working fluid pressure across the tube will reach a relaxing stage with an intermediate value when the wave stops moving. The pressure profile over the shock length is almost the same at the first time increment of the transient study (0.1 ms), as shown in Figure (55) below:

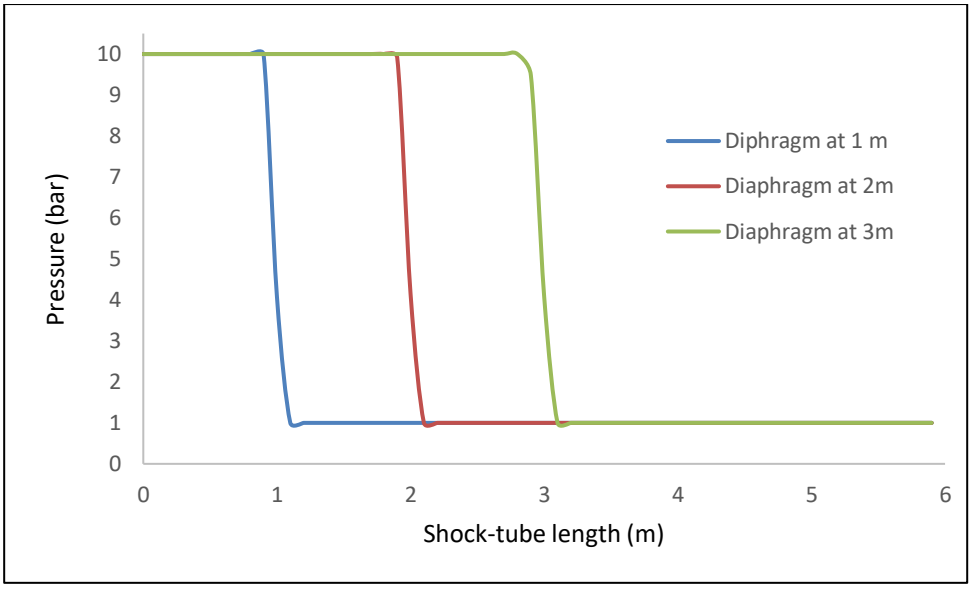

Figure 56. Pressure distribution at the rapture incident (0.0001sec)

The reflected wave (Mach number and temperature) property also presents a key performance indicator between diaphragm position models. Since the ST is described as a 1-D problem, the pressure-temperature distribution only changes in the direction parallel to the following with almost zero gradients perpendicular to the flow (56).

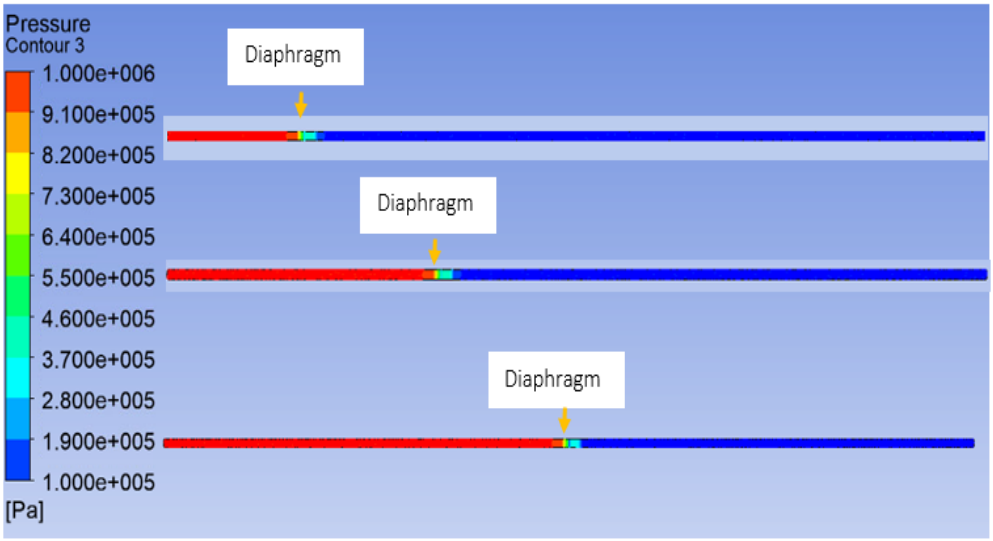

(a)

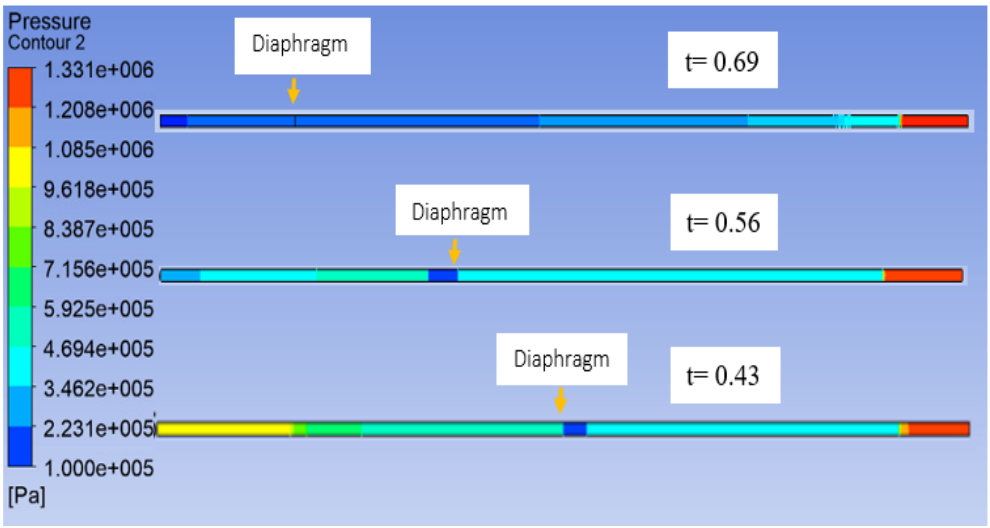

(b)

Figure 57. Pressure contour (a) At the incident of rapture (b) After compression wave reflected from the driver section end-wall.

Figure (56-a) shows the pressure distribution at the first-time step (0.1ms) after the rapture when the compression wave travels along the driven section. The flow discontinuity and the contact surface are shown in Figure (56-b) when the wave is reflected from the driven end-wall. As expected, the wave reflects with high pressure and temperature, which may exceed the value of P_4. However, the time required for the wave to reach the driven and driver end-wall is directly proportional to the distance between the diaphragm and the end-wall. In other words, in this study, a 1m change in the diaphragm position will result in a 0.13ms change in the wave reflection from the driver end-wall. The previous rule applies to the two reflected waves (expansion and compression). Therefore, In Figure (56-b), the reflected expansion wave could not be detected in positions (1m and 2m) for the selected time (0.69ms and 0.56ms), as the expansion waves have already been reflected and reached a relaxation sonic condition.

5.3.3 Validation

The validation of the numerical model was conducted by comparing its values against those observed in the ST experiment. Only one diaphragm position was adopted in the comparison study (middle position) while including all the pressure ratios (6-10).

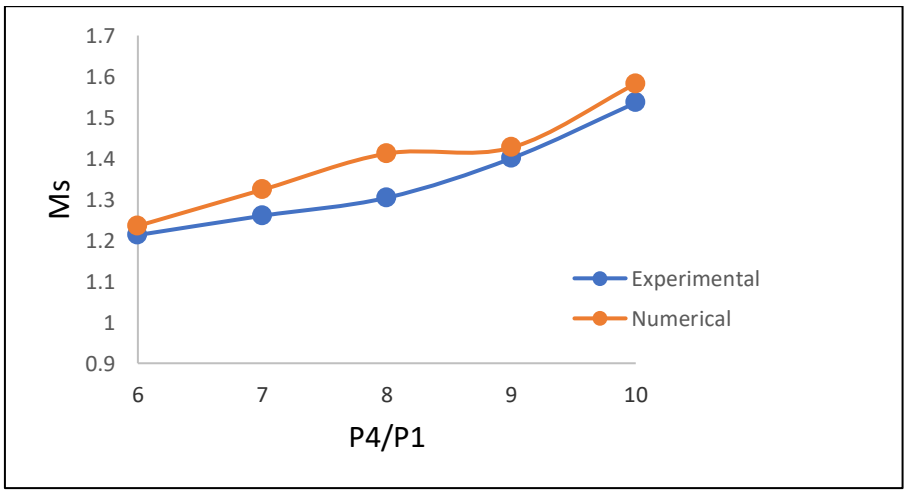

Figure 58. Diaphragm pressure ratio Vs. Incident Mach number (M_i)

Figure (57) illustrates that the values follow increasing trends with pressure increasing. However, the numerical results are approximately 6% larger than the experimental ones at low-pressure values. This may be due to the viscous effect of the gas mixture at low pressure. In contrast, an error of 1% is obtained at 9 and 10 pressure ratios, indicating the reduction of the viscous losses.

5.3.4 Parametric Results

(M_i) dependency on diaphragm position and pressure ratios were combined in one graph, as shown in Figure (54), which compares the effect of the pressure ratios on (M_i) value for the different diaphragm positions. As the diaphragm pressure ratio increased as expected, the velocity of the shock wave and hence its associated Mach

number rose significantly. However, when the diaphragm is located at 2m from the left end, the wave Mach number is 20% smaller than the Mach number obtained at other diaphragm positions (2m and 3m). On the other hand, the two diaphragm locations (1m and 3m) developed approximately the same Mach numbers for the different pressure ratios except for 6 and 9 pressure ratios. For example, in pressure ratio 6 of the diaphragm position-1 model, the Mach number was 5% higher than the Mach number provided by position 3 for the same pressure value. On the other hand, it was clearly shown that diaphragm position 2 (2m) overall reduced 13% in Mach number compared to the other two positions.

The wave velocity increases significantly when the shock wave is reflected from the driven end with high temperature and pressure. Hence, the Mach number associated with the reflected wave (M_r) is higher than the incident one. It is clearly shown in Figure (58) that M_r is almost independent of the diaphragm position except for pressure ratio 10 when the diaphragm position-3 model tends to have a higher M_r Value.

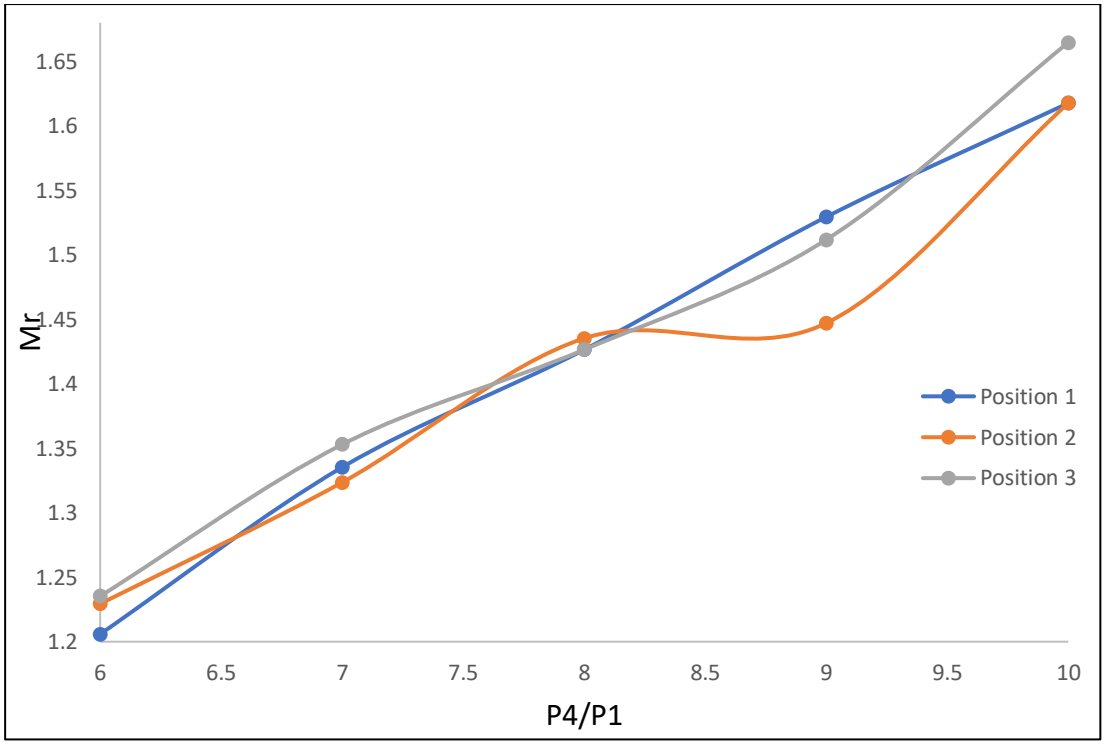

Figure 59. The change of reflected wave Mach number with diaphragm's location and pressure ratio

The wave velocity increases significantly when the shock wave is reflected from the driven end with high temperature and pressure. Hence, the Mach number associated with the reflected wave (M_r) is higher than the incident one. It is clearly shown in Figure.58 that M_r is almost independent of the diaphragm position except for pressure ratio 10 when the diaphragm position-3 model tends to have a higher M_r Value.

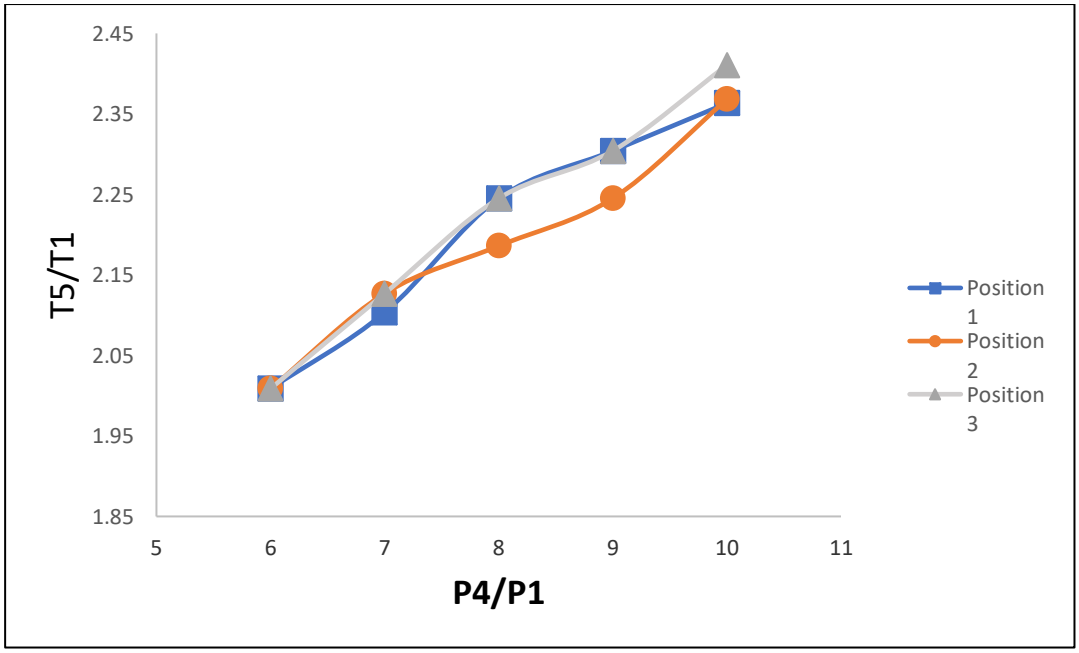

Figure 60. The change of reflected wave temperature with the diaphragm's location and pressure ratio

The temperature behind the reflected wave is also essential in finding the ID time of a fuel using the ST setup. Figure (59). shows the pressure ratios effect on the reflected wave temperature (T5) divided by the initial temperature of the driven side before the rapture (T1). As the pressure ratio increases, the temperature behind the reflected shock wave increases for all the diaphragm positions. The temperature T5 in pressure ratios (6-7) for all the diaphragm position models have the same values (850K-900K). At high-pressure ratios (10-8) diaphragm position-3 model gave high T5 values (1020K, 975K, and 950K) compared to other positions models. Diaphragm position-3 model T5 temperature is almost 10K higher than T5 diaphragm position-1 model and 20K higher than T5 of diaphragm position-2 model.

5.4 Ignition Delay time measurements

The pressure transducers (explained in section 4.3.1) measured the ignition delay

times) in contact with the end-wall. It was determined that time zero of the ignition delay period had been reached by monitoring the sudden rise in pressure at the Endwall that occurred when the incident shock wave arrived.

There are two distinct spikes in side-wall pressure seen in the pressure trace figure (60). The data are recorded by an oscilloscope as explained in section 4.3.2, so every trace is 25000 points processed to the final figure (60). The incident shock wave causes the first increase in pressure, and the reflected shock wave causes the second rise in pressure. The raw data is shown in appendix (E), and all processed data are tabulated in appendix (G) for all experimental conditions.

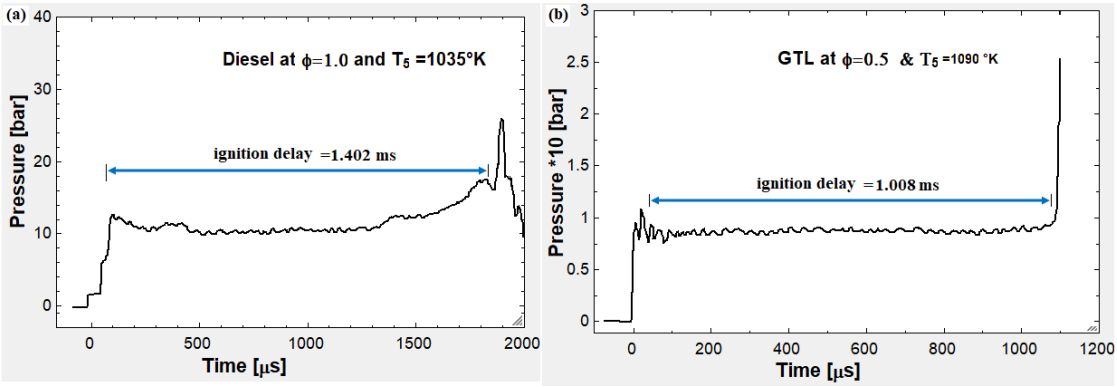

Figure 61 A sample representation of ignition delay time experiment (a) Diesel at Φ=1.0 and T5=1035 K (b) GTL at Φ=1.0 and T_5=1035 K

Experiments on ignition delay times for Diesel, GTL, and a blend of Diesel and GTL were done using the shock tube facility. The conditioned reflected temperature, estimated using the Rankine-H model, is displayed for all data. In addition, Davidson et al., Alturaifi et al., and Penyazkov's [79], [109], [124] investigation is compared to the Diesel findings shown in Figure (61).

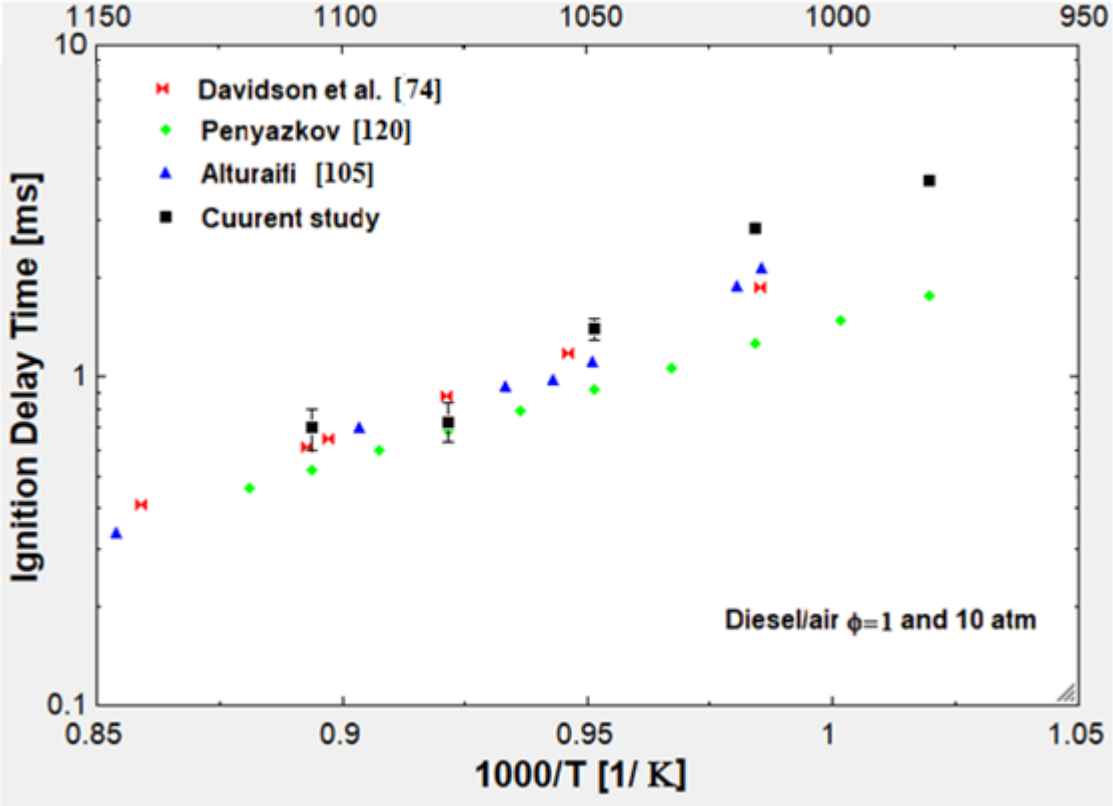

Figure 62 Ignition delay time comparison of Diesel with a comparison of previous three studies at Φ=1.0 and P=10 bar

For a range of 982 K to 1115 K, the ignition delay times depend on the reflected ignition temperature for Diesel fuel. As the temperature of the ignition source rises, the ignition delay becomes shorter and shorter. According to the log scale, the differences between Davidson, Alturaifi, and Penyazkov were 1.8 %, 2.05 %, and 4.8 %, respectively. This variance is mainly the result of the differences in shock tube facility design for fuel loading procedures and the limitations imposed by design capabilities to address safety issues. For example, the study of both Davidson and Alturaifi used an aerosol shock tube in which an accurate fueling to the tube using laser techniques to check the uniformity of the fuel across the test section as described in table (8) in chapter four.

In contrast, the current study depends on the O_2 sensor reading, which only checks the air-fuel ratio in a specific position in the test section. This leads to dealing with a non-homogeneous mixture and then affecting the ignition delay time reading. However, these disparities in the data's general trend may be tolerated.

For the GTL investigation, as shown in figure (62), the recent study by Joshua et al. [95] experimented with the GTL fuel using the aerosol shock tube. They tested at a lean combustion condition (Φ=0.5) and covered a higher range of reflected ignition temperatures until 1300 K at a pressure of 10 bar. Their study was based on the higher temperature investigation, while the current research focuses on the intermediate temperature range. Nevertheless, in the meeting range of ignition reflected temperatures (1000 to 1120K), an average difference of 0.98 % between their model and the present analysis suggests a high agreement. Therefore, the current data can be extrapolated for the uncovered range for a complete comparison. According to Yu G et al. [78], a model was developed to predict the ignition delay times for GTL over a broader range of reflected temperature; however, they did not specify the type of GTL that was used; however, the current results can be validated with their model, with the difference averaging only 2.8 %.

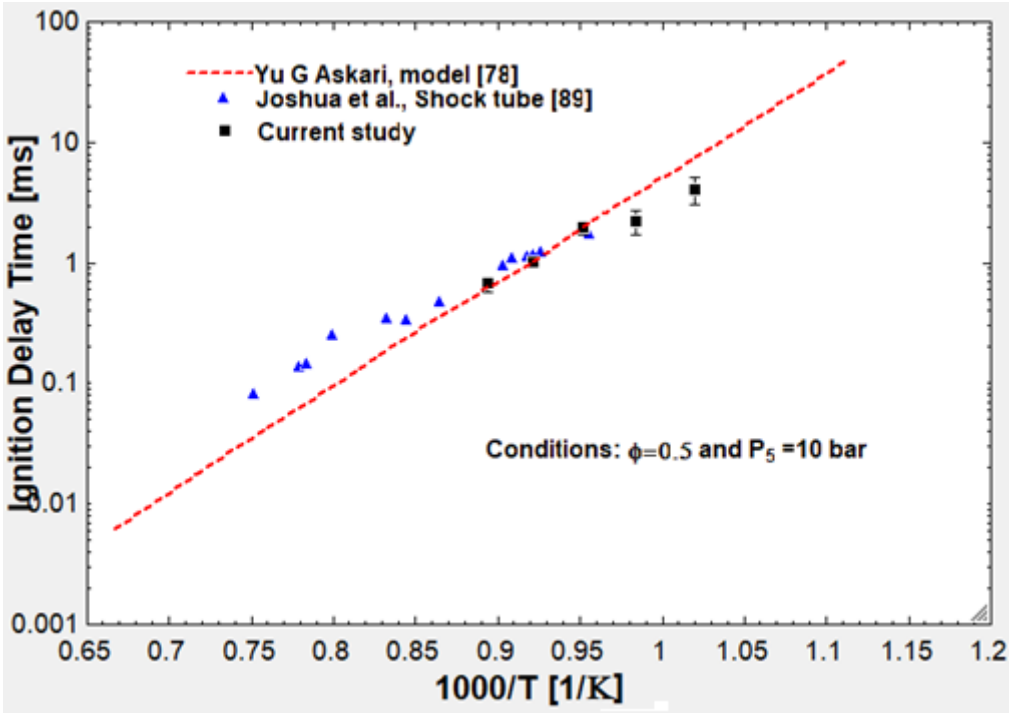

Figure 63 Ignition delay time comparison of GTL with a comparison Joshua et al. at Φ=0.5 and P=10 bar

The experiments were also carried out on 50-50 Diesel-GTL blends tested under various pressure, temperature, and equivalency ratio circumstances, as presented in figure (63). The findings are compared to those obtained using just diesel and only GTL. In stoichiometric circumstances, the blend ignition delay is often close to the GTL ignition delay time at 975 K. Once the temperature is above 1000 K, the three fuels are almost equivalent and have the same ignition delay time value, ranging between 2 and 1 ms. At long last, when the ignition delay time measurements for the blended fuels are in the middle of the pure Diesel and GTL data. For the lean air-fuel mixture, at the starting temperature of 980 K, also the same as the stoichiometric condition, the blend ignition delay time is close to the GTL fuel; however, when the temperature elevated beyond 1000 K, all the ignition delay measurements are approximately identical with the Diesel fuel and have the same observation and

conclusion as stated by Joshua et al.

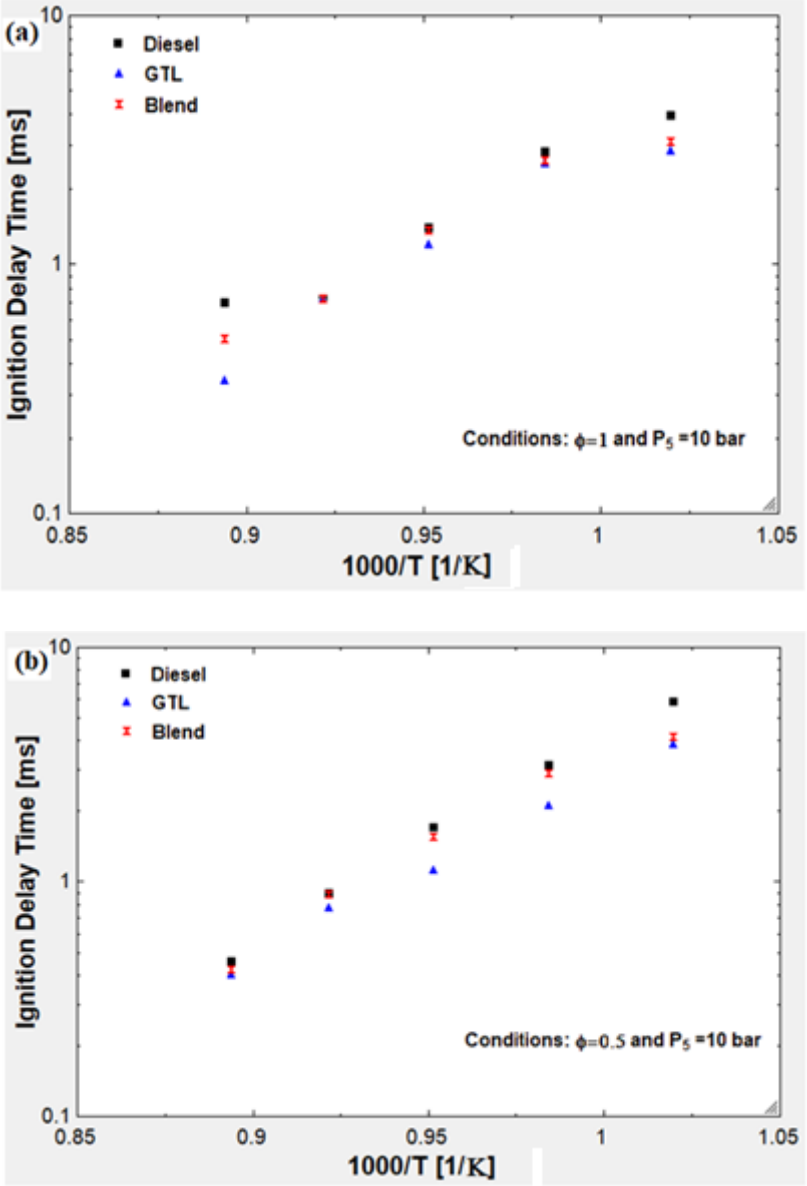

Figure 64 Ignition delay times for 50-50 Diesel-GTL compared to Diesel and GTL at 10 bar (a) stoichiometric condition (b) lean conditions

In addition to that, it is beneficial to see how the pressure and equivalence ratio are affecting the ignition delay time behaviour. For example, in figure (64), The reflected pressure affects the ignition delay times since the shorter ignition delay for the higher value of the reflected pressure for the exact condition of reflected

temperature and equivalence ratio. In the case of equivalence ratio variation, the shorter ignition delay time values were registered for the stoichiometric ignition, and this is reasonable due to the well homogenous mixing of air with fuel. In contrast, the maximum ignition delay was around 10 ms for the rich mixture.

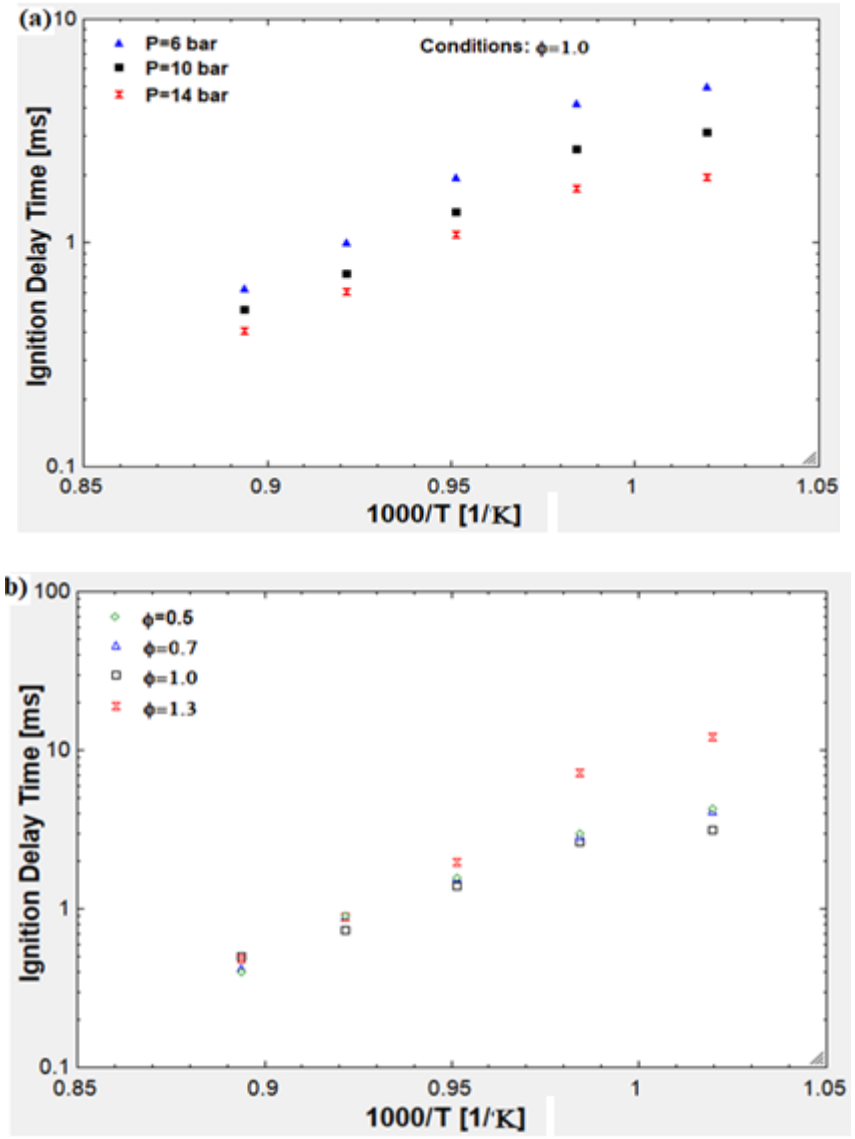

Figure 65 Ignition delay time variation for Diesel-GTL blend (a) various initial pressures (b) different equivalence ratios

Uncertainties exist in measuring this ignition delay time over a broad range of parameters. However, the uncertainty associated with temperature is the most

significant contributing factor to the measurement uncertainty of ignition delay measurements. Changing the temperature by even a small amount causes a significant variation in the ignition delay time. As mentioned in chapter 3, the temperature is found using the Rankine–Hugoniot (Equation 8). The measurement that contributes the most significant to the inaccuracy in the circumstances is mainly due to the shock speed, and the factors leading to this uncertainty are discussed in section 5.2.1. For T 5 and P 5 values, the uncertainty in shock wave velocity is still the most significant contribution to uncertainty. Due to measurement error in gas-phase fuel mole fraction for each experiment, the mixture composition estimate is also subject to additional uncertainty under these settings. A temperature uncertainty of 15–20 K (see appendix H) is calculated for the data reported above for the post-reflected shock zone (T 5), the same as Joshua et al. [95]. Due to the reduced amount of aerosolized fuel present before evaporation, the uncertainty values for lower equivalency ratios are often less (15 K, or better), resulting in a smaller contact area at the interface of the fuel injector after it has been opened. In addition, the fluctuation in temperature causes uncertainty in the timing of the ignition. A rough estimate of the ignition delay time uncertainty of 10% average for the blended fuel was obtained by adjusting T5, P5, and Φ as input variables. As you can see in Figures 61 and 62, there are certain sample-specific uncertainties.

CHAPTER 6: CONCLUSION AND RECOMMENDATIONS

This Dissertation studies the ignition delay of GTL fuel and its blends with standard diesel in a newly developed and produced shock tube test apparatus. As the biggest producer of GTL goods, Qatar was given a thorough explanation for why it should be at the forefront of research into GTL blended fuel characteristics. The new test rig was designed based on the suggestions of previous research using the heated approach.

The first study evaluated shock tube performance through experimental and computational studies. The Shock Tube working fluid was a combination of an Ar-He mixture in the driver section and Air in the driven section. The shock tube setup was operated under five pressure ratios while attaching its diaphragm to the middle. Along with the experimental setup, a two-dimensional ST geometry was simulated using the transient inviscid model. The numerical parametric study introduced three different diaphragm positions and pressure ratios. The results mainly depend on finding the Mach number corresponding to each condition (diaphragm pressure and location). The numerical model appeared to simulate the real case scenario of the ST when validating its results with the model results. Based on the parametric study of the numerical model, one can state that:

1- The understudy experimental ST setup can be simulated numerically using the 2D inviscid-transient CFD model with an acceptable error of less than 6% over the pressure ratios range.
2- When the diaphragm pressure ratios increased, increasing in the incident and reflected Mach numbers could be obtained for all three diaphragm position models.

3- Diaphragm position-2 model gave a low supersonic shock-wave Mach number and low reflected shock wave temperature values compared to the other two positions. Therefore, position-2. In contrast, Diaphragm position-1 and diaphragm middle position models almost giving the same high values of the incident, reflected Mach numbers, and reflected shock wave temperature.

4- As the diaphragm is located near the driver's end, high rapture pressure is generated, and hence, high wave velocity can be obtained. On the other hand, the expansion fan wave (state 3) will require a fewer time to arrive at the driver end and relax to sonic conditions. Therefore diaphragm position 3 (middle of the ST) provides a good compromise between staring gas pressure at the rapture and expansion fan relaxation time effect.

5- Therefore, diaphragm position-2 is more suitable for finding the IDT of gaseous fuel as it required a low Mach number. In contrast, diaphragm positions 1 and 3 models are pretty ideal in finding the IDT of Diesel fuels, as they provide a higher Mach number and reflected wave temperature values.

The usage of the ST as a facility for (IDT) investigations has been dominant for decades. More than 300 published studies with different test conditions for several types of fuels and many kinds of shock tube designs have findings related to chemical kinetics,articularly ignition delay [149]–[156]. This is due to that it is instantly (in microseconds) brings the reactive gas mixture to a well-defined temperature and pressure so that quick chemical reactions may be studied under zero-dimensional circumstances without affecting transport processes. When conducting ignition delay investigations, the shock tube was often calibrated by measuring the IDT of fuels and presenting it over the range of temperatures and pressures that had been determined. As stated by the Rankine-Hugoniot equations

[157], a given Mach Number and shock velocity derive the pressure (P5) and temperature (T5) necessary. However, the diaphragm along the ST can be mounted in any position along the tube, affecting the finding of Mach number and thus the IDT. Therefore, diaphragm position no. 2 was more suitable for finding the IDT of gaseous fuel than other positions, requiring a low Mach number. However, for the gaseous fuels [150], [151], [153], [158], [159]the diaphragm location follows position no. 2 (approximately, the driven and driver section have the same length). In contrast, diaphragm positions 1 and 3 models were pretty ideal in finding the IDT of Diesel fuels, as they provided a high Mach number and high reflected wave temperature values as in the references [23], [124], [151], [160]–[164].

The ignition delay properties of Diesel, GTL, and Diesel GTL blends were investigated under various conditions, including different pressures, temperatures, equivalency ratios, and dilutions. Several studies have been conducted on the autoignition of various diesel, GTL, and Diesel GTL mixes at low to intermediate temperatures and increased pressures. Therefore, the tests were carried out in order to illustrate the effects of temperature, equivalence ratio, and pressure on the time of ignition delays. A future study might concentrate on igniting additional diesel surrogates with GTL and using a broad temperature range for thoroughly validating components that have not been extensively explored in the literature.

The aerosol shock tube technique was the best choice for low-pressure hydrocarbon fuels since fuel condensation challenges and fuel vapour uniformity across the test section will be achieved. In this regard, a Lazer diagnostics system can be implemented to detect the homogeneity of the air-fuel across the test section.

To overcome the nonideality of the thermal boundary layer, the driver gas temperature can be elevated to a limit, not make an essential change in its density.

The main challenge in ignition delay time measurements when using the shock tube facility is the repeatability of the experiments. This is because it is difficult to perform many experiments in a short period due to the difficulty in refixing the diaphragm for the next trial test, which makes it challenging to repeat the experiments. Furthermore, to run more tests in a short time, the installation of the aluminium foil requires a hardening time of at least 4 hours. As a result, developing and discovering a method for rapid diaphragm installation would be beneficial. Furthermore, the evacuation of exhaust fumes and the condensed liquid fuel process contribute to prolonging the period between now and the future trial.

Another problem that must be addressed is fuel condensation. Suppose the injected fuel does not evaporate entirely within the driven zone. It might accumulate inside the tube and lead to misfiring even if the oxygen detector indicates it is within the flammability range. Because of this, the aerosol shock tube is a better solution to the issue of the fuel preparation unit being coupled directly to the driven portion and only allowing the atomized fuels to be charged within the tube.

Furthermore, at higher initial temperatures (>200°C), the sealant material releases smoke, which is particularly noticeable for the seals between the flanges. This will influence the equivalency ratio measurement since the oxygen detector treats this quantity of smoke as a fuel vapour in its analyses.

Finally, other fuel blends can be studied, particularly for the biofuels, such as jojoba oil, corn oil, and waste cooking oil [30].

REFERENCES

[1] U. S. Energy Information Administration, “Transportation and Electric Power Sectors,” *EIA*, Aug. 26, 2021.

[2] U.S Department of Energy, “Comprehensive Annual Energy Data and Sustainability Performance- Energy Efficiency & Renewable,” Aug. 2021. Accessed: Jun. 10, 2020. [Online]. Available: https://ctsedwweb.ee.doe.gov/Annual/Report/Report.aspx

[3] U. . E. I. Adminstration, “Gasoline and Diesel Fuel Update. ,” *EIA*, 1980.

[4] E. Union, *Directive 2009/28/EC of the European Parlement and of the council*. 2009, pp. 16–62.

[5] M. A. Bassiony, A. Ibrahim, and M. M. El-Kassaby, “An experimental study on the effect of using gas-to-liquid (GTL) fuel on diesel engine performance and emissions,” *Alexandria Engineering Journal*, vol. 55, no. 3, pp. 2115–2124, 2016, doi: 10.1016/j.aej.2016.06.026.

[6] A. Tsolakis *et al.*, “Effect of Gas-to-Liquid Diesel Fuels on Combustion Characteristics , Engine Emissions , and Exhaust Gas Fuel Reforming . Comparative Study,” no. 2005, pp. 2377–2384, 2006, doi: 10.1021/ef060332a.

[7] T. Wu, Z. Huang, W. Zhang, J. Fang, and Q. Yin, “Physical and Chemical Properties of GTL - Diesel Fuel Blends and Their Effects on Performance and Emissions of a Multicylinder DI Compression Ignition Engine,” no. 1999, pp. 1908–1914, 2007, doi: 10.1021/ef0606512.

[8] V. F. Produktionstechnik, “Characterization of the Autoignition of Single Droplets of Fischer-Tropsch Fuels and Development of Surrogates,” 2012.

[9] Kibong Cho, Suhan Park, Hyun Gu Roh, and Chang Sik Lee, “Combustion

and Emission Reduction Characteristics of GTL-Biodiesel Fuel in a Single-Cylinder Diesel Engine," 2019.

[10] C. Eigenbrod and P. Rickmers, "Experiments on Induction Times of Diesel-Fuels and its Surrogates," no. June 2015, 2010.

[11] R. H. Clark, D. J. Wedlock, and R. A. Cherrillo, "Future fuels and lubricant base oils from Shell Gas to Liquids (GTL) technology," 2005.

[12] A. M. Elbashir, A. T. Saker, and S. F. Ahmed, "Effect of Utilizing a Novel Intake Manifold Design on Smoke Emissions and Particulate Size Distributions of a Gas-to-Liquid Diesel Engine," *Journal of Energy Resources Technology, Transactions of the ASME*, vol. 144, no. 2, Feb. 2022, doi: 10.1115/1.4050967.

[13] T. L. Alleman and R. L. Mccormick, "Fischer-Tropsch Diesel Fuels-Properties and Exhaust Emissions: A Literature Review," 2003.

[14] S. Czernik and A. v. Bridgwater, "Overview of applications of biomass fast pyrolysis oil," *Energy and Fuels*, vol. 18, no. 2, pp. 590–598, Mar. 2004, doi: 10.1021/ef034067u.

[15] O. Doustdar, M. L. Wyszynski, H. Mahmoudi, and A. Tsolakis, "Enhancing the properties of Fischer-Tropsch fuel produced from syngas over Co/SiO2 catalyst: Lubricity and Calorific Value," in *IOP Conference Series: Materials Science and Engineering*, Sep. 2016, vol. 148, no. 1. doi: 10.1088/1757-899X/148/1/012092.

[16] H. Jahangiri, J. Bennett, P. Mahjoubi, K. Wilson, and S. Gu, "A review of advanced catalyst development for Fischer-Tropsch synthesis of hydrocarbons from biomass derived syn-gas," *Catalysis Science and Technology*, vol. 4, no. 8. Royal Society of Chemistry, pp. 2210–2229, 2014.

doi: 10.1039/c4cy00327f.

[17] P. M. Morgan *et al.*, “982488 Some Comparative Chemical, Physical and Compatibility Properties of Sasol Slurry Phase Distillate Diesel Fuel International Fall Fuels and Lubricants Meeting and Exposition,” 2018.

[18] T. L. Alleman and R. L. Mccormick, “Fischer-Tropsch Diesel Fuels – Properties and Exhaust Emissions : A Literature Review,” *SAE*, no. 724, 2003.

[19] J. L. (John L. Lumley, *Engines : an introduction*. Cambridge University Press, 1999.

[20] D. R. Haylett, D. F. Davidson, and R. K. Hanson, “Ignition delay times of low-vapor-pressure fuels measured using an aerosol shock tube,” *Combustion and Flame*, vol. 159, no. 2, pp. 552–561, Feb. 2012, doi: 10.1016/j.combustflame.2011.08.021.

[21] T. J. Bruno, “Improvements in the measurement of distillation curves. 1. A composition-explicit approach,” *Industrial and Engineering Chemistry Research*, vol. 45, no. 12, pp. 4371–4380, Jun. 2006, doi: 10.1021/ie051393j.

[22] J. D’Alessio, M. Lazzaro, and P. Massoli, “Carbonaceous aerosols from diesel fuel pyrolysis in shock tube,” *Journal of Aerosol Science*, vol. 27, no. SUPPL.1, 1996, doi: 10.1016/0021-8502(96)00330-8.

[23] H. E. Saleh and M. Y. E. Selim, “Shock tube investigation of propane-air mixtures with a pilot diesel fuel or cotton methyl ester,” *Fuel*, vol. 89, no. 2, pp. 494–500, Feb. 2010, doi: 10.1016/j.fuel.2009.09.010.

[24] H. E. Saleh, “The preparation and shock tube investigation of comparative ignition delays using blends of diesel fuel with bio-diesel of cottonseed oil,” *Fuel*, vol. 90, no. 1, pp. 421–429, Jan. 2011, doi: 10.1016/j.fuel.2010.08.019.

[25] S. A. Ashter, “6 - Mechanics of Materials,” in *Thermoforming of Single and Multilayer Laminates*, S. A. Ashter, Ed. Oxford: William Andrew Publishing, 2014, pp. 123–145. doi: https://doi.org/10.1016/B978-1-4557-3172-5.00006-2.

[26] O. Glebova, *Gas to Liquids: Historical Development and Future Prospects*. 2013.

[27] US Energy Information Administration, “Gas-to-liquids plants face challenges in the U.S. market,” *Today in Energy*, Feb. 19, 2014.

[28] G. Evans and C. Smith, “5.11 - Biomass to Liquids Technology,” in *Comprehensive Renewable Energy*, A. Sayigh, Ed. Oxford: Elsevier, 2012, pp. 155–204. doi: https://doi.org/10.1016/B978-0-08-087872-0.00515-1.

[29] J. C. J. Bart, N. Palmeri, and S. Cavallaro, “Evolution of biodiesel and alternative diesel fuels,” in *Biodiesel Science and Technology*, Elsevier, 2010, pp. 713–782. doi: 10.1533/9781845697761.713.

[30] A. M. Sadeq, M. A. Bassiony, A. M. Elbashir, S. F. Ahmed, and M. Khraisheh, “Combustion and emissions of a diesel engine utilizing novel intake manifold designs and running on alternative fuels,” *Fuel*, vol. 255, Nov. 2019, doi: 10.1016/j.fuel.2019.115769.

[31] Y. M. Abdellatif, A. T. Saker, A. M. Elbashir, and S. F. Ahmed, “Combustion and emissions of a gas-to-liquid diesel engine utilizing optimized spiral-helical intake manifold designs,” *Journal of Energy Resources Technology, Transactions of the ASME*, vol. 143, no. 6, Jun. 2021, doi: 10.1115/1.4050342.

[32] S. F. Ahmed, M. T. Gergawy, and M. A. B. Sadiq, Abdellatif M, “Ac ce pt Ma sc r ot Co ed ite d Investigating the Effect of Utilizing New Induction

Manifold Designs on the Combustion Characteristics and Emissions of a DI Diesel Engine Ac ce pt sc t N ot Co py ed d," no. c, 2018, doi: 10.1115/1.4041543.

[33] N. Phasukarratchai, "Phase behavior and biofuel properties of waste cooking oil-alcohol-diesel blending in microemulsion form," *Fuel*, vol. 243, pp. 125–132, May 2019, doi: 10.1016/j.fuel.2019.01.003.

[34] P. Dinesha, S. Kumar, and M. A. Rosen, "Performance and emission analysis of a domestic wick stove using biofuel feedstock derived from waste cooking oil and sesame oil," *Renewable Energy*, vol. 136, pp. 342–351, Jun. 2019, doi: 10.1016/j.renene.2018.12.118.

[35] Z. Yaakob, M. Mohammad, M. Alherbawi, Z. Alam, and K. Sopian, "Overview of the production of biodiesel from Waste cooking oil," *Renewable and Sustainable Energy Reviews*, vol. 18. pp. 184–193, 2013. doi: 10.1016/j.rser.2012.10.016.

[36] D. Capuano, M. Costa, S. di Fraia, N. Massarotti, and L. Vanoli, "Direct use of waste vegetable oil in internal combustion engines," *Renewable and Sustainable Energy Reviews*, vol. 69. Elsevier Ltd, pp. 759–770, Mar. 01, 2017. doi: 10.1016/j.rser.2016.11.016.

[37] A. M. Sadeq, M. A. Bassiony, A. M. Elbashir, S. F. Ahmed, and M. Khraisheh, "Combustion and emissions of a diesel engine utilizing novel intake manifold designs and running on alternative fuels," *Fuel*, vol. 255, Nov. 2019, doi: 10.1016/j.fuel.2019.115769.

[38] A. Abu-Jrai *et al.*, "Performance, combustion and emissions of a diesel engine operated with reformed EGR. Comparison of diesel and GTL fuelling," *Fuel*, vol. 88, no. 6, pp. 1031–1041, Jun. 2009, doi: 10.1016/j.fuel.2008.12.001.

[39] Y. M. Abdellatif, A. T. Saker, A. M. Elbashir, and S. F. Ahmed, “Combustion and emissions of a gas-to-liquid diesel engine utilizing optimized spiral-helical intake manifold designs,” *Journal of Energy Resources Technology, Transactions of the ASME*, vol. 143, no. 6, Jun. 2021, doi: 10.1115/1.4050342.

[40] C. Chen *et al.*, “Study of the characteristics of PM and the correlation of soot and smoke opacity on the diesel methanol dual fuel engine,” *Applied Thermal Engineering*, vol. 148, pp. 391–403, Feb. 2019, doi: 10.1016/j.applthermaleng.2018.11.062.

[41] A. M. Elbashir, A. T. Saker, and S. F. Ahmed, “Effect of Utilizing a Novel Intake Manifold Design on Smoke Emissions and Particulate Size Distributions of a Gas-to-Liquid Diesel Engine,” *Journal of Energy Resources Technology, Transactions of the ASME*, vol. 144, no. 2, Feb. 2022, doi: 10.1115/1.4050967.

[42] J. B. Heywood, *Internal combustion engine fundamentals*. McGraw-Hill, 1988.

[43] C. Sung and H. J. Curran, “Using rapid compression machines for chemical kinetics studies,” *Progress in Energy and Combustion Science*, vol. 44, pp. 1–18, 2014, doi: 10.1016/j.pecs.2014.04.001.

[44] C. Wadkar and P. Chinnathambi, “An Experimental Study on the Factors Affecting Ethanol Ignition Delay Times in a Rapid Compression Machine,” no. April, 2019, doi: 10.4271/2019-01-0576.

[45] Q. Fan and Y. Qi, “Effect of Thermodynamic Conditions on Spark Ignition to Compression Ignition in Ultra-Lean Mixture Using Rapid Compression Machine,” pp. 1–17, 2019, doi: 10.4271/2019-01-0963.Abstract.

[46] H. Liu, H. Zhang, Z. Shi, H. Lu, G. Zhao, and B. Yao, “Performance Characterization and Auto-Ignition Performance of a Rapid Compression Machine,” pp. 6083–6104, 2014, doi: 10.3390/en7096083.

[47] G. Mittal and C. J. Sung, “Aerodynamics inside a rapid compression machine,” *Combustion and Flame*, 2006, doi: 10.1016/j.combustflame.2005.10.019.

[48] C. Allen, G. Mittal, C. Sung, E. Toulson, and T. Lee, “An aerosol rapid compression machine for studying energetic-nanoparticle-enhanced combustion of liquid fuels,” *Proceedings of the Combustion Institute*, vol. 33, no. 2, pp. 3367–3374, 2011, doi: 10.1016/j.proci.2010.06.007.

[49] G. Mittal, S. M. Burke, V. A. Davies, B. Parajuli, W. K. Metcalfe, and H. J. Curran, “Autoignition of ethanol in a rapid compression machine,” *Combustion and Flame*, vol. 161, no. 5, pp. 1164–1171, 2014, doi: 10.1016/j.combustflame.2013.11.005.

[50] G. Kukkadapu, K. Kumar, C. Sung, M. Mehl, and W. J. Pitz, “Autoignition of gasoline and its surrogates in a rapid compression machine,” *Proceedings of the Combustion Institute*, vol. 34, no. 1, pp. 345–352, 2013, doi: 10.1016/j.proci.2012.06.135.

[51] A. B. Mansfield and M. S. Wooldridge, “High-pressure low-temperature ignition behavior of syngas mixtures,” *Combustion and Flame*, vol. 161, no. 9, pp. 2242–2251, 2014, doi: 10.1016/j.combustflame.2014.03.001.

[52] S. Schlatter, B. Schneider, Y. M. Wright, and K. Boulouchos, “N-heptane micro pilot assisted methane combustion in a Rapid Compression Expansion Machine,” vol. 179, no. x, pp. 339–352, 2016, doi: 10.1016/j.fuel.2016.03.006.

[53] A. Kumar, M. Uddi, and C. Sung, “Two-line thermometry and H 2 O measurement for reactive mixtures in rapid compression machine near 7.61 m,” *Combustion and Flame*, vol. 159, no. 12, pp. 3493–3501, 2012, doi: 10.1016/j.combustflame.2012.06.020.

[54] M. T. Donovan, X. He, B. T. Zigler, T. R. Palmer, M. S. Wooldridge, and A. Atreya, “Demonstration of a free-piston rapid compression facility for the study of high temperature combustion phenomena,” vol. 137, pp. 351–365, 2004, doi: 10.1016/j.combustflame.2004.02.006.

[55] O. Taeck and N. Iida, “The investigation about the effects of thermal stratification in combustion chamber on HCCI combustion fueled with DME / n -Butane using Rapid Compression Machine,” *Experimental Thermal and Fluid Science*, vol. 39, pp. 123–133, 2012, doi: 10.1016/j.expthermflusci.2012.01.016.

[56] L. Yu *et al.*, “Exploration of chemical composition effects on the autoignition of two commercial diesels: Rapid compression machine experiments and model simulation,” *Combustion and Flame*, vol. 204, pp. 204–219, Jun. 2019, doi: 10.1016/j.combustflame.2019.03.007.

[57] G. Huanyu, Y. Zheng, H. Zhen, and L. U. Xingcai, “Experimental study of n -heptane ignition delay with carbon dioxide addition in a rapid compression machine under low-temperature conditions,” vol. 57, no. 30, pp. 3953–3960, 2012, doi: 10.1007/s11434-012-5331-8.

[58] G. Cho, D. Jeong, G. Moon, and C. Bae, “Controlled auto-ignition characteristics of methane e air mixture in a rapid intake compression and expansion machine,” *Energy*, vol. 35, no. 10, pp. 4184–4191, 2010, doi: 10.1016/j.energy.2010.07.002.

[59] S. Drost, R. Schießl, M. Werler, J. Sommerer, and U. Maas, “Ignition delay times of polyoxymethylene dimethyl ether fuels (OME2 and OME3) and air: Measurements in a rapid compression machine,” *Fuel*, vol. 258, Dec. 2019, doi: 10.1016/j.fuel.2019.116070.

[60] P. Park and J. C. Keck, “Rapid Compression Machine Measurements of Ignition Delays for Primary Reference Fuels International Congress and Exposition,” 2018.

[61] D. Darcy *et al.*, “A high-pressure rapid compression machine study of n - propylbenzene ignition,” *Combustion and Flame*, vol. 161, no. 1, pp. 65–74, 2014, doi: 10.1016/j.combustflame.2013.08.001.

[62] S. Wang *et al.*, “Experimental and modeling study of the autoignition for diesel and n-alcohol blends from ethanol to n-pentanol in shock tube and rapid compression machine,” *Combustion and Flame*, vol. 227, pp. 296–308, May 2021, doi: 10.1016/j.combustflame.2021.01.019.

[63] H.H. Wolfer, “Ignition lag in diesel engines, translated by royal aircraft establishment,” *Farnborough Library*, vol. 358, no. UDC 621-436.047, 1938.

[64] S.-I. Kwon, M. Arai, and H. Hiroyasu, “Ignition Delay of a Diesel Spray Injected into a Residual Gas Mixture,” *JOURNAL OF ENGINES*, vol. 100, 1991, [Online]. Available: https://www.jstor.org/stable/44554500

[65] M. Lapuerta, J. Sanz-Argent, and R. R. Raine, “Ignition characteristics of diesel fuel in a constant volume bomb under diesel-like conditions. Effect of the operation parameters,” *Energy and Fuels*, vol. 28, no. 8, pp. 5445–5454, Aug. 2014, doi: 10.1021/ef500535j.

[66] A. A. Aradi, T. W. Ryan Ill, and O. Toronto, “Cetane Effect on Diesel Ignition Delay Times Measured in a Constant Volume Combustion Apparatus,” 1995.

[67] Kei MIWA, and Tsunehiro OHMIJA, and Toshio NISHITANI, “A Study of the Ignition Delay of Diesel Fuel Spray Using a Rapid Compression Machine,” 1988.

[68] S. Kobori, T. Kamimoto, and A. A. Aradi, “A study of ignition delay of diesel fuel sprays,” *International Journal of Engine Research*, vol. 1, no. 1, pp. 29–39, 2000, doi: 10.1243/1468087001545245.

[69] D. F. Davidson, Y. Zhu, J. Shao, and R. K. Hanson, “Ignition delay time correlations for distillate fuels,” *Fuel*, vol. 187, pp. 26–32, Jan. 2017, doi: 10.1016/j.fuel.2016.09.047.

[70] D. R. Haylett, P. P. Lappas, D. F. Davidson, and R. K. Hanson, “Application of an aerosol shock tube to the measurement of diesel ignition delay times,” *Proceedings of the Combustion Institute*, vol. 32 I, no. 1, pp. 477–484, 2009, doi: 10.1016/j.proci.2008.06.134.

[71] S. Gowdagiri, W. Wang, and M. A. Oehlschlaeger, “A shock tube ignition delay study of conventional diesel fuel and hydroprocessed renewable diesel fuel from algal oil,” *Fuel*, vol. 128, pp. 21–29, Jul. 2014, doi: 10.1016/j.fuel.2014.02.064.

[72] “1982-Thermal Radiation During Spray Combustion Behind Reflected Shock Waves”.

[73] R. W. Hurn and K. J. Hughes, “Combustion characteristics of diesel fuels as measured in a constant-volume bomb,” 1952.

[74] M. Engineering, “Thermal ignition theory applied to diesel engine autoignition,” vol. 5, no. 2, pp. 193–204, 2004.

[75] R. R. Tacina, “Ignition of Lean Fuel-Air Mixtures In a Premixing-Prevaporizing Duct ’at Temperatures up to 1000 K,” Dec. 1980.

[76] J.A. Tevelde and L.J. Spadaccini, “Autoignition Characteristics of No. 2 Diesel Fue,” NASA Lewis Research Center, 1981.

[77] L. J. Spadaccini and J. A. Tevelde, “Autoignition Characteristics of Aircraft-Type Fuels*,” 1982.

[78] A. G. M. B. Mustayen, X. Wang, M. G. Rasul, J. M. Hamilton, and M. Negnevitsky, “Thermodynamic analysis of diesel engine ignition delay under low load conditions,” *Energy Reports*, vol. 8, pp. 495–501, Jun. 2022, doi: 10.1016/j.egyr.2022.01.201.

[79] M. Assad, V. v Leschevich, O. G. Penyazkov, K. L. Sevrouk, V. E. Tangirala, and N. D. Joshi, “Auto-ignition of Diesel Fuel at High Temperatures and Pressures.”

[80] I. Shahridzuan Abdullah, A. Khalid, N. Jaat, R. Saputra Nursal, H. Koten, and Y. Karagoz, “A study of ignition delay, combustion process and emissions in a high ambient temperature of diesel combustion,” *Fuel*, vol. 297, Aug. 2021, doi: 10.1016/j.fuel.2021.120706.

[81] G. Kukkadapu and C. J. Sung, “Autoignition study of ULSD#2 and FD9A diesel blends,” *Combustion and Flame*, vol. 166, pp. 45–54, Apr. 2016, doi: 10.1016/j.combustflame.2015.12.022.

[82] D. R. Haylett, D. F. Davidson, and R. K. Hanson, “Ignition delay times of low-vapor-pressure fuels measured using an aerosol shock tube,” *Combustion and Flame*, vol. 159, no. 2, pp. 552–561, Feb. 2012, doi: 10.1016/j.combustflame.2011.08.021.

[83] S. Gersen, H. Darmeveil, and H. Levinsky, “The effects of CO addition on the autoignition of H 2, CH 4 and CH 4/H 2 fuels at high pressure in an RCM,” *Combustion and Flame*, vol. 159, no. 12, pp. 3472–3475, Dec. 2012, doi:

10.1016/j.combustflame.2012.06.021.

[84] G. Yu *et al.*, “THEORETICAL PREDICTION OF LAMINAR BURNING SPEED AND IGNITION DELAY OF GAS TO LIQUID FUEL,” 2016. [Online]. Available: http://proceedings.asmedigitalcollection.asme.org/pdfaccess.ashx?url=/data/conferences/asmep/90988/

[85] L. D. Thi, Y. Zhang, and Z. Huang, “Shock tube study on ignition delay of multi-component syngas mixtures - Effect of equivalence ratio,” in *International Journal of Hydrogen Energy*, Apr. 2014, vol. 39, no. 11, pp. 6034–6043. doi: 10.1016/j.ijhydene.2014.01.170.

[86] O. Asgari, S. K. Hannani, and R. Ebrahimi, “Improvement and experimental validation of a multi-zone model for combustion and NO emissions in CNG fueled spark ignition engine,” *Journal of Mechanical Science and Technology*, vol. 26, no. 4, pp. 1205–1212, Apr. 2012, doi: 10.1007/s12206-012-0229-6.

[87] K. Kumar, C. J. Sung, and X. Hui, “Laminar flame speeds and extinction limits of conventional and alternative jet fuels,” *Fuel*, vol. 90, no. 3, pp. 1004–1011, Mar. 2011, doi: 10.1016/j.fuel.2010.11.022.

[88] C. v. Naik *et al.*, “Detailed chemical kinetic mechanism for surrogates of alternative jet fuels,” *Combustion and Flame*, vol. 158, no. 3, pp. 434–445, Mar. 2011, doi: 10.1016/j.combustflame.2010.09.016.

[89] C. Ji, Y. L. Wang, and F. N. Egolfopoulos, “Flame studies of conventional and alternative jet fuels,” *Journal of Propulsion and Power*, vol. 27, no. 4, pp. 856–863, 2011, doi: 10.2514/1.B34105.

[90] S. Dooley *et al.*, “The combustion kinetics of a synthetic paraffinic jet aviation

fuel and a fundamentally formulated, experimentally validated surrogate fuel," *Combustion and Flame*, vol. 159, no. 10, pp. 3014–3020, Oct. 2012, doi: 10.1016/j.combustflame.2012.04.010.

[91] A. T. Holley, Y. Dong, M. G. Andac, F. N. Egolfopoulos, and T. Edwards, "Ignition and extinction of non-premixed flames of single-component liquid hydrocarbons, jet fuels, and their surrogates," *Proceedings of the Combustion Institute*, vol. 31 I, no. 1, pp. 1205–1213, 2007, doi: 10.1016/j.proci.2006.07.208.

[92] K. Kitano, I. Sakata, and R. Clark, "Effects of GTL Fuel Properties on DI Diesel Combustion," 2005.

[93] O. Askari, M. Elia, M. Ferrari, and H. Metghalchi, "Auto-Ignition Characteristics Study of Gas-to-Liquid Fuel at High Pressures and Low Temperatures," *Journal of Energy Resources Technology, Transactions of the ASME*, vol. 139, no. 1, Jan. 2017, doi: 10.1115/1.4033983.

[94] K. Choi, S. Park, H. G. Roh, and C. S. Lee, "Combustion and emission reduction characteristics of GTL-biodiesel fuel in a single-cylinder diesel engine," *Energies (Basel)*, vol. 12, no. 11, Jun. 2019, doi: 10.3390/en12112201.

[95] J. W. Hargis, S. P. Cooper, O. Mathieu, B. Guo, and E. L. Petersen, "High-temperature ignition behavior of conventional and GTL fuels using an aerosol shock tube," *Combustion and Flame*, vol. 226, pp. 490–504, Apr. 2021, doi: 10.1016/j.combustflame.2020.12.030.

[96] H. Song, K. S. Quinton, Z. Peng, H. Zhao, and N. Ladommatos, "Effects of oxygen content of fuels on combustion and emissions of diesel engines," *Energies (Basel)*, vol. 9, no. 1, 2016, doi: 10.3390/en9010028.

[97] J. N. Bradley and R. J. Emrich, “Shock Waves in Chemistry and Physics,” vol. 224, no. 1963, pp. 65–67, 2004, doi: 10.1119/1.1969408.

[98] J. P. Ananthu and N. Asok Kumar, “Performance evaluation of shock tube with helium and carbon dioxide using numerical simulation,” in *Journal of Physics: Conference Series*, Aug. 2019, vol. 1240, no. 1. doi: 10.1088/1742-6596/1240/1/012138.

[99] W. A. Martin and S. Diego, “A Review of Shock Tubes and Shock Tunnels,” 1959.

[100] Ozer Igra and Friedrich Seiler, *Experimental Methods of Shock Wave Research*. 2016. Accessed: Mar. 16, 2022. [Online]. Available: http://www.springer.com/series/8774

[101] Peter O.K. Krehl, “History of Shock Waves, Explosions and Impact A Chronological and Biographical Reference,” 2009. doi: 10.1007/978-3-540-30421-0.

[102] P. H. D. {communicated and J. Thorpe, “Explosion waves and shock waves VI. The disturbance produced by bursting diaphragms with compressed air B y W il l ia m P a y m a n.” [Online]. Available: https://royalsocietypublishing.org/

[103] A. G. Boyer, “Design, Instrumentation and performance of the UTIAS 4-in.x 7-in. Hypersonic Shock Tube,” Toronto, Oct. 1965.

[104] T. Suzuki *et al.*, “Shock tube study of particles’ motion behind a planar shock wave,” *Measurement Science and Technology*, vol. 16, no. 12, pp. 2431–2436, Dec. 2005, doi: 10.1088/0957-0233/16/12/005.

[105] O. Sadot, “Experimental Studies of Shock Wave-Related Phenomena at the Ben-Gurion University: A Review,” in *31st International Symposium on*

Shock Waves 1, 2019, pp. 31–44.

[106] O. Igra, G. Hu, J. Falcovitz, and W. Heilig, "Blast wave reflection from wedges," *Journal of Fluids Engineering, Transactions of the ASME*, vol. 125, no. 3, pp. 510–519, May 2003, doi: 10.1115/1.1567310.

[107] O. Igra, J. Falcovitz, and O. Amann, "Simulation of the starting flow in a wedge-like nozzle," 1998.

[108] L. Houas, G. Jourdan, L. Schwaederlé, R. Carrey, and F. Diaz, "A new large cross-section shock tube for studies of turbulent mixing induced by interfacial hydrodynamic instability," *Shock Waves*, vol. 12, no. 5, pp. 431–434, Mar. 2003, doi: 10.1007/s00193-002-0173-y.

[109] S. A. Alturaifi, R. L. Rebagay, O. Mathieu, B. Guo, and E. L. Petersen, "A Shock-Tube Autoignition Study of Jet, Rocket, and Diesel Fuels," *Energy and Fuels*, vol. 33, no. 3, pp. 2516–2525, Mar. 2019, doi: 10.1021/acs.energyfuels.8b04290.

[110] J. W. Hargis, S. P. Cooper, O. Mathieu, and E. L. Petersen, "A New Aerosol Shock-Tube Facility for the Study of Mixtures with Large Hydrocarbons."

[111] D. F. Davidson, Y. Zhu, J. Shao, and R. K. Hanson, "Ignition delay time correlations for distillate fuels," *Fuel*, vol. 187, pp. 26–32, 2017, doi: 10.1016/j.fuel.2016.09.047.

[112] B. Shu *et al.*, "A shock tube and modeling study on the autoignition properties of ammonia at intermediate temperatures," *Proceedings of the Combustion Institute*, vol. 37, no. 1, pp. 205–211, 2019, doi: 10.1016/j.proci.2018.07.074.

[113] R. S. Tranter and B. R. Giri, "A diaphragmless shock tube for high temperature kinetic studies A diaphragmless shock tube for high temperature kinetic studies," vol. 094103, 2008, doi: 10.1063/1.2976671.

[114] A. Haselbacher, S. Balachandar, and S. W. Kieffer, “Open-ended shock tube flows: Influence of pressure ratio and diaphragm position,” *AIAA Journal*, vol. 45, no. 8, pp. 1917–1929, Aug. 2007, doi: 10.2514/1.23081.

[115] S. R. Nagaraja, J. K. Prasad, and G. Jagadeesh, “Theoretical-experimental study of shock wave-assisted metal forming process using a diaphragmless shock tube,” *Proceedings of the Institution of Mechanical Engineers, Part G: Journal of Aerospace Engineering*, vol. 226, no. 12, pp. 1534–1543, Dec. 2012, doi: 10.1177/0954410011424808.

[116] I. D. S. Rego, Y. Miyoshi, T. Ando, and K. Goto, “Development of a Large Diameter Diaphragmless Shock Tube for Use in Gas-Dynamic Laser Experiments,” *Engineering Sciences Reports, Kyushu University Institutional Repository*, vol. 29, no. 2, pp. 283–288, 2008, doi: 10.15017/14578.

[117] Raymond Brun and Lucien Z. Dumitrescu, “Shock Waves @ Marseille I,” 1995. doi: 10.1007/978-3-642-78829-1.

[118] David A. Russell, “Studies of the Effects of Cross-Sectional Area Change and BoundaryLayer Growth on Shock Wave Motion,” California Institute of Technology, Pasadena, California, 1961.

[119] R. F. Dressler, “Turbulent Flow in Shock Tubes of Varying Cross Section *,” 1954.

[120] N. Asano, “Shock waves and non-stationary flow in a duct of varying cross-section,” *Journal of Fluid Mechanics*, vol. 46, no. 1, pp. 111–128, Mar. 1971, doi: 10.1017/S0022112071000429.

[121] B. E. L. Deckker and J. Gururajat, “AN INVESTIGATION OF SHOCK WAVE BEHAVIOUR IN DUCTS WITH A GRADUAL OR AREA SUDDEN ENLARGEMENT IN CROSS-SECTIONAL.”

[122] W. Chester, “The Propagation of Shock Waves along Ducts of Varying Cross Section,” vol. 6, H. L. Dryden, Th. von Kármán, G. Kuerti, F. H. van den Dungen, L. Howarth, and J. Pérès, Eds. Elsevier, 1960, pp. 119–152. doi: https://doi.org/10.1016/S0065-2156(08)70111-X.

[123] R. A. Alpher and D. R. White, “Flow in shock tubes with area change at the diaphragm section,” *Journal of Fluid Mechanics*, vol. 3, pp. 457–470, 1958.

[124] D. F. Davidson, D. R. Haylett, and R. K. Hanson, “Development of an aerosol shock tube for kinetic studies of low-vapor-pressure fuels,” *Combustion and Flame*, vol. 155, no. 1–2, pp. 108–117, Oct. 2008, doi: 10.1016/j.combustflame.2008.01.006.

[125] D. R. Haylett, D. F. Davidson, and R. K. Hanson, “Second-generation aerosol shock tube: An improved design,” *Shock Waves*, vol. 22, no. 6, pp. 483–493, Nov. 2012, doi: 10.1007/s00193-012-0383-x.

[126] R. K. Hanson, “AEROFROSH : A Shock condition calculator for multi-component fuel aerosol-laden flows”.

[127] S. Downes, A. Knott, and I. Robinson, “Towards a shock tube method for the dynamic calibration of pressure sensors Subject Areas :,” 2014.

[128] M. Zelan, F. Arrhén, P. Jarlemark, and O. Mollmyr, “Characterization of a fiber-optic pressure sensor in a shock tube system for dynamic calibrations,” *Metrologia*, vol. 48, p. 48, doi: 10.1088/0026-1394/52/1/48.

[129] Z. Yao, X. Liu, C. Wang, and W. Yang, “Improved traceable measurement of the reflected step pressure in shock tube with the compensation of shock wave attenuation,” *Aerospace Science and Technology*, vol. 107, p. 106302, 2020, doi: 10.1016/j.ast.2020.106302.

[130] J. Salminen, S. Saxholm, J. Hämäläinen, and R. Högström, “Advances in

traceable calibration of cylinder pressure transducers," *Metrologia*, vol. 57, no. 4, Aug. 2020, doi: 10.1088/1681-7575/ab8fb9.

[131] v Rodriguez, G. J. R Saurel 1, and L Houas, "Solid-particle jet formation under shock-wave acceleration," *Phys Rev E Stat Nonlin Soft Matter Phys .*, 2013, doi: 10.1103/PhysRevE.88.063011.

[132] "PHOTOMULTIPLIER TUBES PHOTON IS OUR BUSINESS Basics and Applications THIRD EDITION (Edition 3a)," 2007.

[133] S. Grzejnictwo, "Product Catalogue," SZCZECIN POLAND, 2008.

[134] Omega, "All Stainless Steel Transducer/Transmitter Multimedia Compatibility High-Performance Silicon Technology Imperial Model." Accessed: May 20, 2022. [Online]. Available: https://www.omega.com/omegaFiles/pressure/pdf/PX309.pdf

[135] Killer SensorsONE Ltd, "High Temperaure Pressure Transmitter." Accessed: Mar. 18, 2022. [Online]. Available: www.SensorsONE.co.uk

[136] T. Inc, "User Manual TDS3000B Series Digital Phosphor Oscilloscopes." [Online]. Available: www.tektronix.comwww.valuetronics.com

[137] "User' s Guide ® MADE IN CL540A and CL540AZ Thermocouple Source User' s Guide ® MADE IN CL540A and CL540AZ Thermocouple Source CL540A and CL540ZA Thermocouple Source CL540A CL540ZA."

[138] G. Y. Pech, "A Practical Thermocouple Shield," Toronto, Jun. 1964.

[139] TANZANIA BUREAU OF STANDARDS, "TBS/G TDC4 (5006) P3-Aluminium foil for Packing-Specification," 2020. Accessed: Mar. 19, 2022. [Online]. Available: http://www.puntofocal.gov.ar/notific_otros_miembros/tza394_t.pdf

[140] D. R. White, "Influence of diaphragm opening time on shock-tube flows,"

Cambridge University Press, vol. 4, no. 6, pp. 585–599, May 1958.

[141] B. Sturtevant and E. Slachmuylders, “End-wall heat-transfer effects on the trajectory of a reflected shock wave,” *Physics of Fluids*, vol. 7, no. 8, pp. 1201–1207, 1964, doi: 10.1063/1.1711362.

[142] Baganoff Donald, “Experiments on the wall-pressure history in shock-reflexion processes,” California Institute of Technology, Pasadena California, 1964.

[143] H. de Oliveira Piva, “ELECTRON BEAM MEASUREMENTS OF DENSITY IN SHOCK WAVES REFLECTING FROM A COLD WALL Thesis by,” California Institute of Technology, Pasadena California, 1968.

[144] M. F. Campbell, T. Parise, A. M. Tulgestke, R. M. Spearrin, D. F. Davidson, and R. K. Hanson, “Strategies for obtaining long constant-pressure test times in shock tubes,” *Shock Waves Journal*, Mar. 2014, [Online]. Available: http://crf.sandia.gov/http://hanson.stanford.edu/

[145] T. A. Brubbs and F. E. Belles, “Contact-Surface Tailoring in Real Shock Tubes,” Washington DC, Oct. 1965. [Online]. Available: https://ntrs.nasa.gov/search.jsp?R=19650025800

[146] A. R. Amadio, M. W. Crofton, and E. L. Petersen, “Test-time extension behind reflected shock waves using CO2-He and C3H8-He driver mixtures,” *Shock Waves*, vol. 16, no. 2, pp. 157–165, Dec. 2006, doi: 10.1007/s00193-006-0058-6.

[147] Y. Badri, A. Elbashir, A. Saker, and S. F. Ahmed, “An experimental and numerical investigation of the effects of the diaphragm pressure ratio and its position on a heated shock tube performance,” *Energy Science and Engineering*, 2022, doi: 10.1002/ese3.1090.

[148] A. Jayakumar, A. Danam, and A. N. Kumar, “Shock Tube Performance Studies With Air And Carbon Di-Oxide Using Numerical Simulation,” 2014. [Online]. Available: http://www.ijser.org

[149] Y. Heng, G. Li, J. Liang, and Z. Zhang, “Ignition characteristics of ethanol – hydrogen mixtures with di ff erent hydrogen contents at elevated initial temperatures,” *Fuel*, vol. 281, no. 1178, p. 118742, 2020, doi: 10.1016/j.fuel.2020.118742.

[150] X. Jiang, J. Chen, W. Huang, and H. Zhao, “Interpreting the e ff ect of hydrogen addition on the auto-ignition of branched alkane : A case study of iso -butane / hydrogen / O 2 / Ar mixtures,” *Fuel*, vol. 284, no. July 2020, p. 119019, 2021, doi: 10.1016/j.fuel.2020.119019.

[151] A. C. Merkel and G. Ciccarelli, “Diesel spray ignition behind a reflected shock wave,” *Combustion and Flame*, vol. 217, pp. 237–247, Jul. 2020, doi: 10.1016/j.combustflame.2020.04.004.

[152] D. Nativel, P. Niegemann, J. Herzler, M. Fikri, and C. Schulz, “Ethanol ignition in a high-pressure shock tube : Ignition delay time and high-repetition-rate imaging,” *Proceedings of the Combustion Institute*, vol. 000, pp. 1–9, 2020, doi: 10.1016/j.proci.2020.07.021.

[153] S. Saxena, M. S. P. Kahandawala, and S. S. Sidhu, “A shock tube study of ignition delay in the combustion of ethylene,” *Combustion and Flame*, vol. 158, no. 6, pp. 1019–1031, 2011, doi: 10.1016/j.combustflame.2010.10.011.

[154] A. J. Sundararaj, B. C. Pillai, and K. R. Guna, “Thermochimica Acta Experimental investigation of effect of temperature on ignition behaviour of seeded refined kerosene,” *Thermochimica Acta*, vol. 683, no. May 2019, p. 178469, 2020, doi: 10.1016/j.tca.2019.178469.

[155] B. L. Wang, H. Olivier, and H. Gro, “Ignition of shock-heated H 2 -air-steam mixtures,” vol. 133, pp. 93–106, 2003, doi: 10.1016/S0010-2180(02)00552-7.

[156] C. Yang, W. Wang, Y. Li, and X. Cheng, “Quantitative study on chemical effects of actual / simulated recirculated exhaust gases on ignition delay times of n-heptane / ethanol fuel blends at elevated temperature,” *Fuel*, vol. 263, no. August 2019, p. 116327, 2020, doi: 10.1016/j.fuel.2019.116327.

[157] G. Ben-Dor, O. Sadot, and O. Igra, “30th International Symposium on Shock Waves 2 ISSW30-Volume 2.”

[158] L. Dinh, Y. Zhang, and Z. Huang, “ScienceDirect Shock tube study on ignition delay of multi-component syngas mixtures e Effect of equivalence ratio,” *International Journal of Hydrogen Energy*, vol. 39, no. 11, pp. 6034–6043, 2014, doi: 10.1016/j.ijhydene.2014.01.170.

[159] W. Xia *et al.*, “Shock tube and modeling study of ignition delay times of propane under O 2 / CO 2 / Ar atmosphere,” *Combustion and Flame*, vol. 220, pp. 34–48, 2020, doi: 10.1016/j.combustflame.2020.06.024.

[160] O. S. M. Abu-elyazeed, “On the ignition delay of two types of Castor oil bio-diesel using shock tube experiments,” *FUEL*, vol. 144, pp. 157–163, 2015, doi: 10.1016/j.fuel.2014.12.041.

[161] V. N. Hoang and L. D. Thi, “Experimental study of the ignition delay of diesel/biodiesel blends using a shock tube,” *Biosystems Engineering*, vol. 134, pp. 1–7, Jun. 2015, doi: 10.1016/j.biosystemseng.2015.03.009.

[162] Y. Qiu *et al.*, “An experimental and modeling study of autoignition characteristics of butanol/diesel blends over wide temperature ranges,” *Combustion and Flame*, vol. 217, pp. 175–187, Jul. 2020, doi:

10.1016/j.combustflame.2020.03.031.

[163] A. J. Sundararaj, K. R. Guna, and M. William, “Experimental investigation of the effect of temperature on ignition of modified kerosene,” pp. 1–9, 2021, doi: 10.1177/1468087420988191.

[164] T. Tsuboi, T. Hozumi, K. Hayata, and K. Ishii, “Study of diesel spray combustion in air containing burnt gas using a shock tube,” *Combustion Science and Technology*, vol. 177, no. 3, pp. 513–537, Mar. 2005, doi: 10.1080/00102200590909094.

APPENDIX A: FISHER-TROPSCH FUELS SPECIFICATIONS [13]

Property	Method*	F-T "N" & Sasol F-T	F-T "K":	No.2	CARB	Blend 1	Blend 2	Blend 3	Shell	CARB	50:50 F-T: CARB blend
FeedStock		Natural Gas	Natural Gas						Natural Gas		
Density, 15°C	D4052	0.7769	0.7779	0.8547	0.8308	0.8292	0.8140	0.7909	0.7845	0.8337	0.8089
API Gravity		50.6	50.3	34.0	38.7	39.1	42.2	47.3	54		47.9
Distillation, °C	D86										
IBP		189	185	184	203	192	191	193	210	175	191
10%		209	208	214	218	209	209	209	260	213	224
50%		256	257	259	249	258	258	258	300	268	282
90%		331	332	312	290	318	322	329	331	332	322
FBP		356	358	342	351	348	356	359	338	363	348
Viscosity 40°C, cSt	D445	2.43	2.42	2.35	2.42	2.35	2.36	2.40	3.57		2.91
Flash Point, °C	D93	67		69					72		101
Cetane number	D613	>73.7	73.3	40.3	49.4	50.9	55.2	62.2	>74†		69.0
Cetane Index	D4737									53.7	
Sulfur, mass%	D4294	0.001	0.002	0.022	0.028	0.018	0.015	0.006		0.01	
Sulfur, ppmw	D5453								<5‡		
SFC Aromatics, vol%	D5186										
Total		2.68	2.46	38.22	9.91	27.05	20.40	9.92	0.1		6.8
Mono-									0.1		1.1
Poly-									0.1		0.1
Total Aromatics, mass%	No method given									18.1	
HPLC Aromatics, mass%		0.47		32.78	6.65						
Mono-		0.44		23.39	6.62						
Di-		0.03		8.70	0.03						
Poly-		<0.01		0.69	<0.01						
FIA, vol%	D1319										
Aromatics											
Olefins											
Saturates											
Carbon, wt%	D5291								84.91		85.54
Hydrogen, wt%									14.97		14.71
Oxygen, wt%	By Dif		0.3						Negligible		Negligible
Nitrogen, ppmw	D5291								0.67		0.35
Cloud Point, °C	D2500								3		-5
Pour Point, °C	D97								0		-9
Unadditized SLBOCLE, g	D6078								1700		
Additized SLBOCLE, g									4050		3900
Unadditized HFRR, µm	D6079								420/540/570		
Additized HFRR, µm									210		590/570
HHV, MJ/kg	D240								47.11	45.60	
LHV, MJ/kg									43.92	42.77	

* ASTM Method unless otherwise specified
U Unknown company
tDensity at 20°C
† Above measurement capability
‡ Below measurement capability

Property	Method*	PetroSA	No.2	Shell F-T	Cert. Diesel	No.2	CARB	ULSD	F-T	20% F-T: 80% LS	F-T[U]	CARB	LSHC
FeedStock		Natural Gas		Natural Gas							Natural Gas		
Density, 15°C	D4052	0.8042		0.7845	0.8302	0.849	0.831	0.811	0.781	0.806	0.7803	0.8379	0.8168
API Gravity		44.0											
Distillation, °C													
IBP		229.9	188	240	177	186	194	241	215	238	222	191	208
10%	D86	235.3	212	260	217	225	217	246	258	247	257	215	232
50%		254.7	256	291	303	266	249	251	289	255	288	253	277
90%		323.7	307	325	315	311	285	261	325	281	324	308	321
FBP		361.2	331	336	338	337	344	285	337	322	337	330	343
Viscosity 40°C, cSt	D445	2.98		3.47	2.7	2.62	2.42	2.41	3.21	2.55	32.04	2.457	2.921
Flash Point, °C	D93	97		109	67	76	69	101	98	100	98	72	85
Cetane number	D613	48.9		>74.8	47.4	47	45	67	84	79	81.1	48.4	64.6
Cetane Index	D4737		48.7	78.3	48.3								
Sulfur, mass%	D4294	<5											
Sulfur, ppmw	No method given										0	175	1
Sulfur, ppmw	D2622					300	300	<10	<10	<10			
Sulfur, ppmw	D5453		200	<10	430								
SFC Aromatics, vol%													
Total	D5186	9.18				32.5	8.9	1.2	0.2	0.6	1.2	20.1	9.9
Mono-											1.2	15.0	8.9
Poly-		0.21									0.0	5.1	1.0
HPLC Aromatics, mass%													
Mono-													
Di-													
Poly-													
FIA, vol%	D1319												
Aromatics			24.7		31.9								
Olefins			1.5		1.5								
Saturates			73.8		66.6								
Carbon, wt%	D5291	83.98	86.11			86.6	86.0	85.6	84.8	85.3	84.77	86.48	85.70
Hydrogen, wt%		14.43	13.37			13.4	13.9	14.4	15.1	14.6	15.12	13.48	14.3
Oxygen, wt%	By Dif	1.59	<0.03			0.0	0.1	0.0	0.1	0.1	0.11	0.05	0
Nitrogen, ppmw	D5291										2	9	<1
Cloud Point, °C	D2500	<-60		4	-16						0	-24	-4
Pour Point, °C	D97	<-60									-1	-33	-7
Unadditized SLBOCLE, g	D6078	1950											
Additized SLBOCLE, g		3800											
Unadditized HFRR, µm	D6079	600											
Additized HFRR, µm		255											
HHV, MJ/kg	D240	46.69	46.14			42.7	43.1	43.4	43.9	43.5	47.2	45.9	46.3
LHV, MJ/kg		43.63	43.19								43.9	42.6	43.3

* ASTM Method unless otherwise specified
U Unknown company
‡Density at 20°C
† Above measurement capability
‡ Below measurement capability

Property	Method*	No.2 "A"	CARB	ExxonMobil F-T Diesel	ExxonMobil F-T Naphtha	No.2 "B"	UK diesel	ExxonMobil 280-700 Cut	ExxonMobil 300-700 Cut	ExxonMobil 280-800 Cut	ExxonMobil 280-900 Cut
FeedStock				Natural Gas	Natural Gas			Natural Gas	Natural Gas	Natural Gas	Natural Gas
Density, 15°C	D4052	0.845	0.842	0.774	0.731	0.846	0.854	0.768	0.772	0.778	0.785
API Gravity	D287										
Distillation, °C											
IBP		191	210	194	71	174	184	136	173	174	174
10%	D86	226	229	231	113						
50%		261	253	286	167	291	288	252	257	273	291
90%		308	291	327	220						
FBP		344	344	338	253	390	345	330	332	375	390
Viscosity 40°C, cSt	D445	2.63	2.79	2.66	0.87						
Flash Point, °C	D93	69	82	60	<40	69.5	77.5	41.1			69.5
Cetane number	D613	45.5	50.2	74	>74	53.0	50.1	70.0	71.8	71.8	
Cetane index	D4737					56.5	50.8	80.2	81.0	80.2	82.3
Sulfur, mass%	D4294										
Sulfur, ppmw	D2622	300	300	0	0						
Sulfur, %	RD 86/10					0.04	0.05	0	0	0	0
SFC Aromatics, vol%											
Total	D5186			0.26	0.01						
Mono-											
Poly-											
Total Aromatics, %	D1319	31.9	8.7								
HPLC Aromatics, mass%											
Mono-											
Di-											
Poly-						27.9	26.7	0	0	0	0
Total Aromatics, %	IP-391					7.1	6.4	0	0	0	0
Polyaromatics, %											
Carbon, wt%	D5291										
Hydrogen, wt%											
Oxygen, wt%	By Dif										
Nitrogen, ppmw	D5291										
Cloud Point, °C	D5771					-6	-5	-36	-36	-33	-10
CFPP, °C	IP 309					-7	-18	-45	-46	-33	-15
Pour Point, °C	D97										
HHV, MJ/kg	D240										
LHV, MJ/kg											

* ASTM Method unless otherwise specified
U Unknown company
‡Density at 20°C
† Above measurement capability
‡ Below measurement capability

APPENDIX B: PRESSURE TRANSDUCER CALIBRATION

O M E G A E N G I N E E R I N G I N C.

PRESSURE TRANSDUCER
FINAL CALIBRATION

0.00 - 25.00 BAR
Excitation 28.000 Vdc

Job: Serial: 185489
Model: PXM01MD0-025BARG5T Tested By: CHRIS
Date: 2/4/2015 Temperature Range: +16 to +71 C
Calibrated: 0.00 - 25.00 BAR Specfile: PXM01-5T

Pressure BAR	Unit Data Vdc
0.00	0.001
12.50	2.510
25.00	5.012
12.50	2.510
0.00	0.000

Balance 0.001 Vdc
Sensitivity 5.011 Vdc
80% Shunt 4.007 Vdc Change at 0.00 BAR (-INPUT to -OUTPUT)

ELECTRICAL LEAKAGE: PASS
PRESSURE CONNECTION/FITTING: G 1/4 Female
ELECTRICAL WIRING/CONNECTOR: Green = + Signal
White = - Signal
Black = - Excitation
Red = + Excitation
Blue & Orange = Shunt

This Calibration was performed using Instruments and Standards that are traceable to the United States National Institute of Standards Technology.

S/N	Description	Range	Reference	Cal Cert
0078/90-03	AUTO 1000 PSI DRUCK	0 - 25.00 BAR	C-2501	C-2501
US37046448	AT34970 DMM	Unit Under Test	C-2465	C-2465

Q.A. Representative : *Chris Diaz* Date: 2/4/2015

This transducer is tested to & meets published specifications. After final calibration our products are stored in a controlled stock room & considered in bonded storage. Depending on environment & severity of use factory calibration is recommended every one to three years after initial service installation date.

Omega Engineering Inc., One Omega Drive, Stamford, CT 06907
http://www.omega.com email: info@omega.com phone (800) 826-6342

O M E G A E N G I N E E R I N G I N C.

PRESSURE TRANSDUCER
FINAL CALIBRATION

0.00 - 25.00 BAR
Excitation 28.000 Vdc

Job: Serial: 185489
Model: PXM01MD0-025BARG5T Tested By: CHRIS
Date: 2/4/2015 Temperature Range: +16 to +71 C
Calibrated: 0.00 - 25.00 BAR Specfile: PXM01-5T

Pressure BAR	Unit Data Vdc
0.00	0.001
12.50	2.510
25.00	5.012
12.50	2.510
0.00	0.000

Balance 0.001 Vdc
Sensitivity 5.011 Vdc
80% Shunt 4.007 Vdc Change at 0.00 BAR (-INPUT to -OUTPUT)

ELECTRICAL LEAKAGE: PASS
PRESSURE CONNECTION/FITTING: G 1/4 Female
ELECTRICAL WIRING/CONNECTOR: Green = + Signal
White = - Signal
Black = - Excitation
Red = + Excitation
Blue & Orange = Shunt

This Calibration was performed using Instruments and Standards that are traceable to the United States National Institute of Standards Technology.

S/N	Description	Range	Reference	Cal Cert
0078/90-03	AUTO 1000 PSI DRUCK	0 - 25.00 BAR	C-2501	C-2501
US37046448	AT34970 DMM	Unit Under Test	C-2465	C-2465

Q.A. Representative : *Chris Diaz* Date: 2/4/2015

This transducer is tested to & meets published specifications. After final calibration our products are stored in a controlled stock room & considered in bonded storage. Depending on environment & severity of use factory calibration is recommended every one to three years after initial service installation date.

Omega Engineering Inc., One Omega Drive, Stamford, CT 06907
http://www.omega.com email: info@omega.com phone (800) 826-6342

TEYSEER INDUSTRIAL SUPPLIES AND SERVICES CO. W.L.L.
P.O. Box: 40523 St. No. 11 Gate No. 74 Bldg. No. 163
Industrial Area, Doha State of Qatar
Tel: (974) 44585400 Fax: (974) 44607637

Certificate of Calibration

Print Date: 13-Jan-2021 **Cert No.** 551220084326883

Customer:
QATAR UNIVERSITY/DR.SAMER AHMED
DOHA-QATAR

Work Order No.	QA-10042365	Purchase Order No.	CASH
Cal ID No.	233531.0143	Serial No.	233531.0143
Equipment ID	N/A	Department	N/A
Equipment Type	PRESSURE TRANSDUCER	Performed By	JOE MANNIX RETUERNE
Manufacturer	KELLER	Received Condition	IN TOLERANCE
Model No.	PA-35XHTC	Returned Condition	IN TOLERANCE
Range / Size	0 to 1000 bar	Calibration Date	12-Jan-2021
Temp/RH	20.8°C / 51 %	Calibration Interval	12 MONTHS
		Calibration Due Date	12-Jan-2022

Calibration Notes:
Site Location: MPC Lab
See attached 1 page calibration data

Reference Instruments Used in Calibration

I.D.	Description	Model No.	Serial No.	Manufacturer	Cal. Due Date	Traceability No.
5150000	ADVANCE MODULAR CALIBRATOR	DPI620	3150000	DRUCK INC	Dec 10, 2021	551220083865766
DC6341	PORTABLE PRESSURE CALIBRATOR	3130-G2M	3287519	FLUKE	Sep 28, 2021	551220083242137

Procedures Used in Calibration

Procedure Name	Description
MPC-PTG-001	Pressure Transmitters and Switches, General, rev01, Jan-28-2020

Calibration Performed By:

JOE MANNIX RETUERNE
Calibration Technician

QC Approval

RICHARD POSANSO
QA/QC Inspector

Page 1 of 1

(CERT, Rev 7)

Calibration Report of PRESSURE TRANSDUCER

Procedure Ref.	[illegible]	Work Order No.	[illegible]
Calibration ID	[illegible]	Serial Number	[illegible]
Asset ID	NONE	Model No.	[illegible]
Manufacturer	[illegible]	Calibration Date	[illegible]

MEASUREMENT ACCURACY

Pressure Input	Current Output (Expected)	Lower Limit	As Found	As Left	Upper Limit	Result	Uncertainty (U)
[illegible]	[illegible]	[illegible]	[illegible]	[illegible]	[illegible]	[illegible]	[illegible]
[illegible]	[illegible]	[illegible]	[illegible]	[illegible]	[illegible]	[illegible]	[illegible]
[illegible]	[illegible]	[illegible]	[illegible]	[illegible]	[illegible]	[illegible]	[illegible]
[illegible]	[illegible]	[illegible]	[illegible]	[illegible]	[illegible]	[illegible]	[illegible]
[illegible]	[illegible]	[illegible]	[illegible]	[illegible]	[illegible]	[illegible]	[illegible]
[illegible]	[illegible]	[illegible]	[illegible]	[illegible]	[illegible]	[illegible]	[illegible]
[illegible]	[illegible]	[illegible]	[illegible]	[illegible]	[illegible]	[illegible]	[illegible]
[illegible]	[illegible]	[illegible]	[illegible]	[illegible]	[illegible]	[illegible]	[illegible]
[illegible]	[illegible]	[illegible]	[illegible]	[illegible]	[illegible]	[illegible]	[illegible]
[illegible]	[illegible]	[illegible]	[illegible]	[illegible]	[illegible]	[illegible]	[illegible]

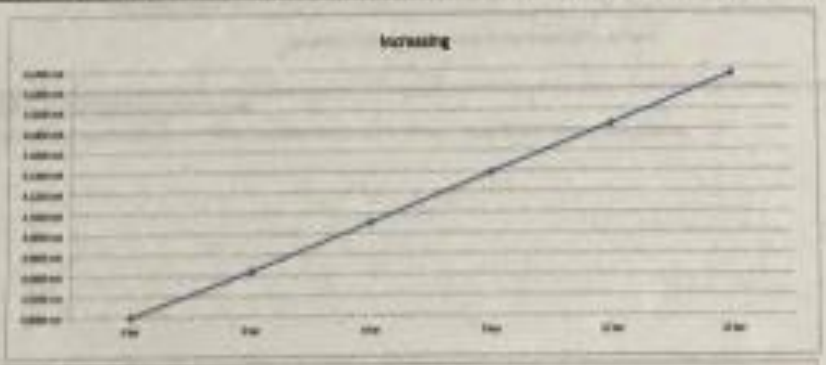

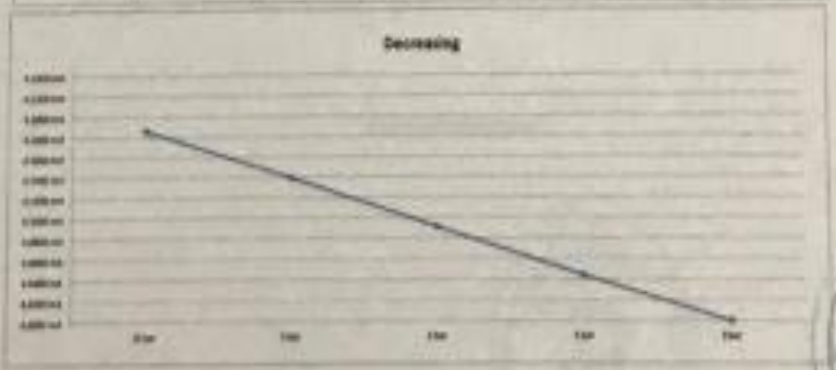

Confidential: Controlled Document
Cannot be reproduced without the approval of the Quality Department

MICRO PRECISION

Tisco

Calibration Report of PRESSURE TRANSDUCER

Procedure Ref:	MPC-PTD-001	Work Order No.:	QA-20XXXXX
Calibration ID:	22XXX1XX3	Serial Number:	22XXX1XX3
Asset ID:	1XXX	Model No.:	PA-3XXXTC
Manufacturer:	KELLER	Calibration Date:	January 12, 2021

Statements of Pass or Fail Conformance

The uncertainty of measurement has been taken into account when determining compliance with specification.
All measurements and test results quoted intended to ensure the probability of false accept does not exceed 2% in compliance with ANSI/NCSL Z540.3-2006

The status of compliance with the acceptance criteria is reported as:

PASS – Compliant with specification

PASS* – The measured value is within acceptance limits.
However, a portion of the expanded uncertainty of measurement at 95% exceeds the specified tolerance

FAIL* – The measured value is not within the acceptance limits.
However, a portion of the expanded uncertainty of measurement at 95% is within the specified tolerance

FAIL – Not compliant with specification

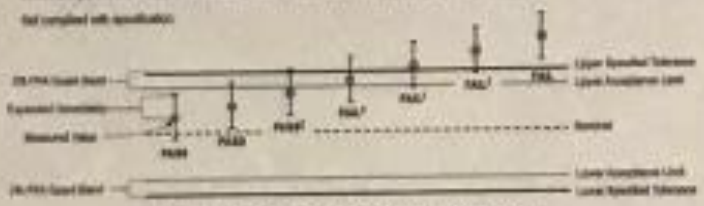

Acceptance limits for 2% probability of false accept (PFA) guard band

The expanded uncertainty of measurement is stated as the standard uncertainty of measurement multiplied by the coverage factor k = 2, which for a normal distribution corresponds to a coverage probability of approximately 95%, unless otherwise stated.

This calibration report complies with ISO/IEC 17025:2017 and ANSI/NCSL Z540.3-2006, Method 5 — Guard Bands Based on Test Uncertainty Ratio

- End of Calibration Report -

TISCO

Confidential: Consider Incomer

Page 3 of 3

APPENDIX C: K-TYPE THERMOCOUPLE PROPERTIES

Specifications

(Unless otherwise indicated all specifications are rated from a nominal 23 °C, 70 % RH for 1 year from calibration)

General	
Accuracy	±(0.015% of Reading + 0.009 mV)
Cold Junction Compensation	± 0.45°F (±0.25 °C)
Millivolt Range	-13.000 to 80.000 mV
Operating Temperature Range	-25 to 60 °C (-10 to 140 °F)
Temperature Drift	≤ 50 ppm of range (includes mV and Cold Junction)
Relative Humidity Range	10 % ≤RH ≤90 % (0 to 35 °C), Non-condensing
	10 % ≤RH≤ 70 % (35 to 60 °C), Non-condensing
Size With Boot	4.96 x 2.73 x 1.79 inches, 126 x 69 x 45 mm (L x W x H) 5.67 x 3.06 x 2.05 inches, 144 x 78 x 52 mm (L x W x H)
Weight With Boot	8.4 ounces, 0.24 kg (including batteries) 11 ounces, 0.32 kg (including batteries)
Batteries	Four "AA" Alkaline 1.5V (LR6)
Battery Life	50 Hours
Optional NiMh Rechargeable battery kit	120 VAC for North America Only; charger, four NiMh batteries, AC & DC cords [Part # 020-0103]
Low Battery	Low battery indication with nominal 1 hour of life left
Protection against misconnection	Over-voltage protection to 60 V dc (rated for 30 seconds)
Display	High contrast graphic liquid crystal display. LED backlighting for use in low lit areas.

Source	
Output Impedance	< 0.3 Ohms
Source Current	> 20 mA (drives 80 mV into 10 Ohms)
Noise	≤ 4 microvolts p-p for frequencies of 10 Hz or below

Ranges & Accuracies

T/C Type	Degrees C Range	Accuracy	Degrees F Range	Accuracy	T/C Material	ISA/ANSI Color
J	-200.0 to -180.0	±0.5°	-346.0 to -292.0	±0.9°	+Iron -Connstantan Jacket	White Red Black
	-180.0 to -50.0	±0.4°	-292.0 to -58.0	±0.7°		
	-50.0 to 500.0	±0.3°	-58.0 to 932.0	±0.5°		
	500.0 to 1200,0	±0.4°	932.0 to 2192.0	±0..7°		
K	-230.0 to -100.0	±0.8°	-382.0 to -148.0	±1.4°	+ Chromel® -Alumel® Jacket	Yellow Red Yellow
	-100.0 to 1050.0	±0.4°	-148.0 to 1922.0	±0.7°		
	1050.0 to 1371.1	±0.5°	1922.0 to 2500.0	±0.9°		
T	-260.0 to -200.0	±1.2°	-436.0 to -328.0	±2.2°	+Copper -Constantan Jacket	Blue Red Blue
	-200.0 to -50.0	±0.7°	-328.0 to -58.0	±1.3°		
	-50.0 to 0.0	±0.4°	-58.0 to 32.0	±0.7°		
	0.0 to 400.0	±0.3°	32.0 to 752.0	±0.5°		
E	-240.0 to -200.0	±0.6°	-400.0 to -328.0	±1.1°	+Chromel -Constantan Jacket	Purple Red Purple
	-200.0 to -100.0	±0.4°	-328.0 to -148.0	±0.7°		
	-100.0 to 850.0	±0.3°	-148.0 to 1562.0	±0.5°		
	850.0 to 1000.0	±0.4°	1562.0 to 1832.0	±0.7°		
R	-13.3 to 250.0	±1.4°	-1.0 to 482.0	±2.5°	+Pt/13Rh -Platinum Jacket	Black Red Green
	250.0 to 750.0	±0.8°	482.0 to 1382.0	±1.4°		
	750.0 to 1600.0	±0.7°	1382.0 to 2192.0	±1.3°		
	1600.0 to 1767.8	±0.8°	2192.0 to 3214.0	±1.4°		

APPENDIX D: CERAMIC FIBER INSULATION

Physical Properties				
Specs	**Standard Grade**	**High-Purity Grade**	**High-Alumina Grade**	**Zirconia Grade**
Color	White	White	White	White
Maximum Use Limit	2300°F	2300°F	2552°F	2552°F
Continuous Use Limit	1832°F	2012°F	2192°F	2462°F
Density (PCF)	12.5	12.5	12.5	12.5
Tensile Strength (PSI)	≤5%	≤5%	≤5%	≤5%
Break Strength (PSI)	24.65	24.65	24.65	24.65
Thermal Conductivity	(Btu in./hr/ft²°F)			
@ 260°C (500°F)	0.24	0.24	0.24	0.24
@ 540°C (1004°F)	0.51	0.51	0.51	0.51
@ 600°C (1112°F)	0.55	0.55	0.55	0.55
@ 800°C (1472°F)	0.76	0.76	0.76	0.76
@1000°C (1832°F)	1.18	1.18	1.18	1.18

Activate Windc

Appendix (E): Sample of Raw Results from the DAQ

Ignition delays time reading for the stoichiometric mixture for Diesel-GTL blend (P4=6 bar) & 1100 K

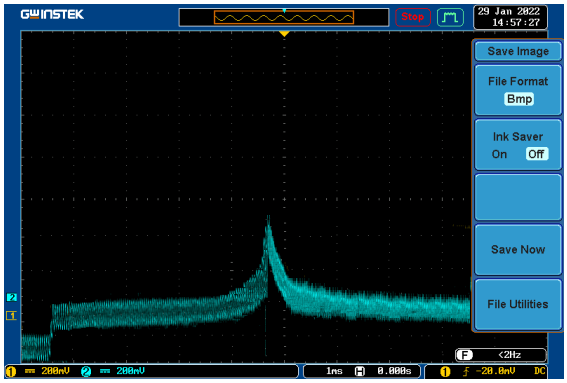

Ignition delays time reading for the lean mixture for Diesel-GTL blend (P4=10 bar) & 1075 K

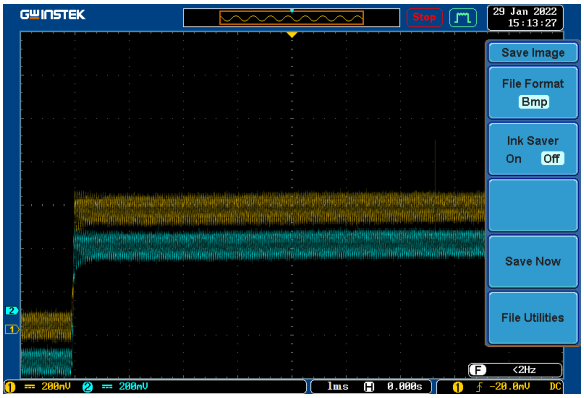

Ignition delays time reading for the rich mixture for Diesel-GTL blend (P4=14 bar) & 980 K

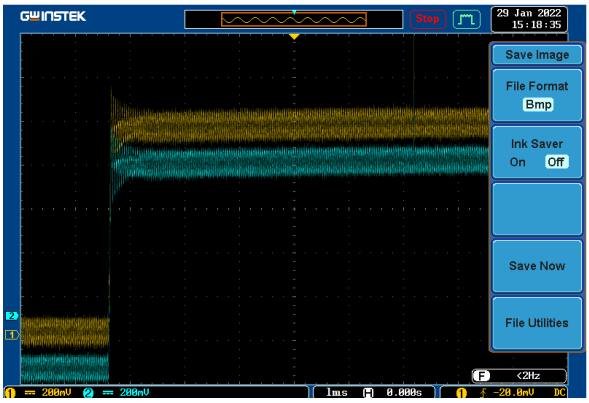

APPENDIX (F): THE ISENTROPIC MODEL EES CODE

```
"Initial Conditions"
{T1=170 [°C]}
P1=1 [bar]
T4=25 [°C]
x=0.1
P4=10 [bar]
{u1=300 [m/s]}

"Properties"
Cp_Ar=cp(Argon,T=T4,P=P4)
Cp_He=cp(Helium,T=T4,P=P4)
Cv_Ar=cv(Argon,T=T4,P=P4)
Cv_He=cv(Helium,T=T4,P=P4)
Cp_N2=cp(Nitrogen,T=T4,P=P4)
Cv_N2=cv(Nitrogen,T=T4,P=P4)
Cp_mix=x*Cp_Ar+(1-x)*Cp_He
Cv_mix=x*Cv_Ar+(1-x)*Cv_He

P4_HeAr=P4
P4_He=P4
P4_Ar=P4
P4_N2=P4

"Heat Capacity Ratio"
gamma_1=cp(Air_ha,T=T1,P=P1)/cv(Air_ha,T=T1,P=P1)
gamma_4HeAr=Cp_mix/Cv_mix
gamma_4He=Cp_He/Cv_He
gamma_4Ar=Cp_Ar/Cv_Ar
gamma_4N2=Cp_N2/Cv_N2

"Gas constant"
R_1=(cp(Air_ha,T=T1,P=P1)-cv(Air_ha,T=T1,P=P1))*convert(kJ,J)
R_4HeAr=(Cp_mix-Cv_mix)*convert(kJ,J)
R_4He=(Cp_He-Cv_He)*convert(kJ,J)
R_4Ar=(Cp_Ar-Cv_Ar)*convert(kJ,J)
R_4N2=(Cp_N2-Cv_N2)*convert(kJ,J)

"================================================================="
"Speed of Sound"
a1=sqrt(gamma_1*R_1*(converttemp(C,K,T1)))
a4_HeAr=sqrt(gamma_4HeAr*R_4HeAr*(converttemp(C,K,T4)))
a4_He=sqrt(gamma_4He*R_4He*(converttemp(C,K,T4)))
a4_Ar=sqrt(gamma_4Ar*R_4Ar*(converttemp(C,K,T4)))
a4_N2=sqrt(gamma_4N2*R_4N2*(converttemp(C,K,T4)))

"================================================================="
"Pressure in the driver gas"
P4_HeAr=P1*((1+((2*gamma_1)/(1+gamma_1))*(((Ms1_HeAr)^2)-1))*(1/(1-
(((gamma_4HeAr-1)/(gamma_1+1)))*(a1/a4_HeAr)*(Ms1_HeAr-
1/Ms1_HeAr)))^((2*gamma_4HeAr)/(gamma_4HeAr-1)))
P4_He=P1*((1+((2*gamma_1)/(1+gamma_1))*(((Ms1_He)^2)-1))*(1/(1-(((gamma_4He-
1)/(gamma_1+1)))*(a1/a4_He)*(Ms1_He-1/Ms1_He)))^((2*gamma_4He)/(gamma_4He-1)))
P4_Ar=P1*((1+((2*gamma_1)/(1+gamma_1))*(((Ms1_Ar)^2)-1))*(1/(1-(((gamma_4Ar-
1)/(gamma_1+1)))*(a1/a4_Ar)*(Ms1_Ar-1/Ms1_Ar)))^((2*gamma_4Ar)/(gamma_4Ar-1)))
```

P4_N2=P1*((1+((2*gamma_1)/(1+gamma_1))*(((Ms1_N2)^2)-1))*(1/(1-(((gamma_4N2-1)/(gamma_1+1)))*(a1/a4_N2)*(Ms1_N2-1/Ms1_N2)))^((2*gamma_4N2)/(gamma_4N2-1)))

"Incident shock Mach Number"
Ms1_HeAr=u1_HeAr/a1

Ms1_He=u1_He/a1

Ms1_Ar=u1_Ar/a1

Ms1_N2=u1_N2/a1

"Reflected Shock conditions"
P5_HeAr/P1=((2*gamma_1*(Ms1_HeAr^2)-(gamma_1-1))/(gamma_1+1))*((-2*(gamma_1-1)+(3*gamma_1-1)*Ms1_HeAr^2)/(2+(gamma_1-1)*Ms1_HeAr^2))
P5_He/P1=((2*gamma_1*(Ms1_He^2)-(gamma_1-1))/(gamma_1+1))*((-2*(gamma_1-1)+(3*gamma_1-1)*Ms1_He^2)/(2+(gamma_1-1)*Ms1_He^2))
P5_Ar/P1=((2*gamma_1*(Ms1_Ar^2)-(gamma_1-1))/(gamma_1+1))*((-2*(gamma_1-1)+(3*gamma_1-1)*Ms1_Ar^2)/(2+(gamma_1-1)*Ms1_Ar^2))
P5_N2/P1=((2*gamma_1*(Ms1_N2^2)-(gamma_1-1))/(gamma_1+1))*((-2*(gamma_1-1)+(3*gamma_1-1)*Ms1_N2^2)/(2+(gamma_1-1)*Ms1_N2^2))

T5_HeAr/(converttemp(C,K,T1))=((2*(gamma_1-1)*Ms1_HeAr^2+3-gamma_1)*((3*gamma_1-1)*Ms1_HeAr^2-2*(gamma_1-1)))/((gamma_1+1)^2*Ms1_HeAr^2)
T5_He/(converttemp(C,K,T1))=((2*(gamma_1-1)*Ms1_He^2+3-gamma_1)*((3*gamma_1-1)*Ms1_He^2-2*(gamma_1-1)))/((gamma_1+1)^2*Ms1_He^2)
T5_Ar/(converttemp(C,K,T1))=((2*(gamma_1-1)*Ms1_Ar^2+3-gamma_1)*((3*gamma_1-1)*Ms1_Ar^2-2*(gamma_1-1)))/((gamma_1+1)^2*Ms1_Ar^2)
T5_N2/(converttemp(C,K,T1))=((2*(gamma_1-1)*Ms1_N2^2+3-gamma_1)*((3*gamma_1-1)*Ms1_N2^2-2*(gamma_1-1)))/((gamma_1+1)^2*Ms1_N2^2)

APPENDIX (G): ALL RESULTS

For different pressures (bar), different reflected temperatures (k), and Air-fuel mixture conditions (stoichiometric, lean and rich)

Diesel

Φ=1.0					
T5	**1/T5**	**P4=6**	**P4=10**	**P4=14**	**P4=20**
980	1.02	12.036	3.962	1.098	0.217
1016	0.9843	7.234	2.855	0.984	0.113
1051	0.9515	3.843	1.402	0.651	0.084
1085	0.9217	1.502	0.7322	0.427	0.035
1119	0.8937	0.9102	0.7003	0.311	0.017

Φ=0.5					
T5	**1/T5**	**P4=6**	**P4=10**	**P4=14**	**P4=20**
980	1.02	21.008	9.341	1.378	0.789
1016	0.9843	11.178	6.003	0.951	0.371
1051	0.9515	6.421	2.941	0.712	0.0997
1085	0.9217	3.213	1.587	0.61	0.0621
1119	0.8937	1.378	1.231	0.4002	0.0227

Φ=0.7					
T5	**1/T5**	**P4=6**	**P4=10**	**P4=14**	**P4=20**
980	1.02	16.571	8.054	1.256	0.564
1016	0.9843	10.872	5.381	0.968	0.222
1051	0.9515	3.784	2.312	0.7005	0.094
1085	0.9217	1.864	1.005	0.0613	0.0555
1119	0.8937	0.554	0.845	0.355	0.0205

Φ=1.3					
T5	**1/T5**	**P4=6**	**P4=10**	**P4=14**	**P4=20**
980	1.02	N/A	10.911	5.261	1.001
1016	0.9843	N/A	7.001	2.009	0.634
1051	0.9515	N/A	3.005	0.975	0.511
1085	0.9217	N/A	1.201	0.621	0.102
1119	0.8937	N/A	0.741	0.374	0.072

GTL

Φ=0.5

T5	1/T5	P4=6	P4=10	P4=14	P4=20
980	1.02	13.812	4.085	2.741	1.672
1016	0.9843	7.056	2.207	2.566	1.522
1051	0.9515	5.341	1.956	1.985	1.341
1085	0.9217	3.611	1.008	0.988	0.891
1119	0.8937	2.397	0.6724	0.667	0.557

Φ=0.7					
T5	**1/T5**	**P4=6**	**P4=10**	**P4=14**	**P4=20**
980	1.02	4.135	3.985	2.691	1.572
1016	0.9843	2.361	2.211	2.516	1.422
1051	0.9515	2.006	1.856	1.777	1.241
1085	0.9217	1.141	0.991	0.938	0.791
1119	0.8937	0.8011	0.6511	0.617	0.457

Φ=1.0					
T5	**1/T5**	**P4=6**	**P4=10**	**P4=14**	**P4=20**
980	1.02	4.002	3.512	2.5001	1.5031
1016	0.9843	2.303	2.123	2.003	1.423
1051	0.9515	1.991	1.812	1.777	1.056
1085	0.9217	1.054	0.856	0.851	0.751
1119	0.8937	0.801	0.523	0.444	0.423

Φ=1.3					
T5	**1/T5**	**P4=6**	**P4=10**	**P4=14**	**P4=20**
980	N/A	20.512	20.312	2.841	1.822
1016	0.9843	8.021	7.821	2.666	1.672
1051	N/A	7.598	7.398	2.085	1.491
1085	0.9217	2.002	1.802	1.088	1.041
1119	0.8937	1.332	1.132	0.767	0.707

Blends of Diesel-GTL

Φ=0.5					
T5	**1/T5**	**P4=6**	**P4=10**	**P4=14**	**P4=20**
980	1.02	6.056	4.256	3.005	1.523
1016	0.9843	4.785	2.985	2.512	1.375
1051	0.9515	3.366	1.566	2.412	1.032
1085	0.9217	1.691	0.8988	1.121	0.784
1119	0.8937	1.2005	0.4005	0.3555	0.314

Φ=0.7

T5	1/T5	P4=6	P4=10	P4=14	P4=20
980	1.02	N/A	4.152	2.014	1.501
1016	0.9843	N/A	2.894	1.955	1.302
1051	0.9515	N/A	1.562	1.366	0.991
1085	0.9217	1.4001	0.8894	0.851	0.777
1119	0.8937	1.2350	0.4231	0.3412	0.301

Φ=1.0					
T5	**1/T5**	**P4=6**	**P4=10**	**P4=14**	**P4=20**
980	1.02	5.012	3.123	1.957	1.205
1016	0.9843	4.231	2.623	1.745	1.191
1051	0.9515	1.965	1.378	1.087	0.915
1085	0.9217	1.007	0.7322	0.6058	0.556
1119	0.8937	0.6289	0.5023	0.4038	0.087

Φ=1.3					
T5	**1/T5**	**P4=6**	**P4=10**	**P4=14**	**P4=20**
980	1.02	N/A	12	10.314	4.15
1016	0.9843	N/A	7.233	6.358	3.25
1051	0.9515	N/A	1.965	1.53	3.08
1085	0.9217	N/A	0.89	0.84	1.023
1119	0.8937	N/A	0.485	0.351	0.056

APPENDIX (H): UNCERTAINTY CALCULATIONS

"Initial Conditions"
T1=170 [°C]
P1=1 [bar]
T4=25 [°C]
x=0.1
dist=0.217 [m]
{t=0.01 }
{P4=10 [bar]}
"===
"
"Heat Capacity Ratio"
gamma_1=cp(Air_ha,T=T1,P=P1)/cv(Air_ha,T=T1,P=P1)
"===
"
"Gas constant"
R_1=(cp(Air_ha,T=T1,P=P1)-cv(Air_ha,T=T1,P=P1))*convert(kJ,J)
"===
="
"Speed of Sound"
a1=sqrt(gamma_1*R_1*(converttemp(C,K,T1)))

u1_HeAr=dist/t
Ms1_HeAr=u1_HeAr/a1

T5_HeAr/(converttemp(C,K,T1))=((2*(gamma_1-1)*Ms1_HeAr^2+3-
gamma_1)*((3*gamma_1-1)*Ms1_HeAr^2-2*(gamma_1-
1)))/((gamma_1+1)^2*Ms1_HeAr^2)

Uncertainty Results:

1 P4 [bar]	2 t [second]	3 a1	4 $u1_{HeAr}$	5 $Ms1_{HeAr}$	6 $T5_{HeAr}$
2±0.05	0.0004305±2.000E-08	421.3±2.3	504.1±5.807	1.197±0.01525	556±8.299
6±0.05	0.0003231±2.000E-08	421.3±2.3	671.6±7.738	1.594±0.02033	800.2±12.53
10±0.05	0.0002846±2.000E-08	421.3±2.3	762.5±8.784	1.81±0.02307	950.6±15.55
14±0.05	0.0002581±2.000E-08	421.3±2.3	840.8±9.686	1.996±0.02544	1093±18.53
18±0.05	0.0002473±2.000E-08	421.3±2.3	877.5±10.11	2.083±0.02656	1163±20.05
20±0.05	0.0002166±2.000E-08	421.3±2.3	1002±11.54	2.378±0.03031	1422±25.72